MICRO-OBJECT MANIPULATION USING OSCILLATING BUBBLES

by

Sang Kug Chung

B.S., Myongji University, South Korea, 2000

M.S., Pohang University of Science and Technology, South Korea, 2003

Submitted to the Graduate Faculty of the

Swanson School of Engineering in partial fulfillment

of the requirements for the degree of

Doctor of Philosophy

University of Pittsburgh

2009

UNIVERSITY OF PITTSBURGH

SWANSON SCHOOL OF ENGINEERING

This dissertation was presented

by

Sang Kug Chung

It was defended on

June 15, 2009

and approved by

Minking K. Chyu, Professor,

Department of Mechanical Engineering and Materials Science

Laura Schaefer, Associate Professor,

Department of Mechanical Engineering and Materials Science

Kang Kim, Assistant Professor,

Department of Medicine and Department of Bioengineering

Dissertation Director: Sung Kwon Cho, Assistant Professor,

Department of Mechanical Engineering and Materials Science

MICRO-OBJECT MANIPULATION USING OSCILLATING BUBBLES

Sang Kug Chung, PhD

University of Pittsburgh, 2009

This thesis deals with the development of novel manipulation techniques of micro/mini objects using oscillating bubbles. Two major physical principles studied and applied are cavitational microstreaming flows and electrowetting on dielectric (EWOD) actuation in gaseous bubbles. Micro/mini bubbles oscillated and handled in 2-D and 3-D spaces using these two principles are key components serving as carriers of objects to be manipulated.

The first type of manipulation system allows us to manipulate mini/micro objects on a 2-D space. A series of bubble operations (creation, elimination, and transportation) and object manipulations (capturing, carrying, and releasing) is extensively investigated in this configuration along with modeling and analysis. The capturing force is identified and completely confirmed as the acoustic radiation force through several experiments. Effects of the frequency and amplitude of acoustic excitation on capturing are quantified with high-speed imaging. The bubble elimination process is modeled by two sequential steps: catalytic reaction and dissolving process.

In addition, the similar operations of capturing, carrying, releasing of objects are accomplished only using AC-EWOD, not using the acoustic excitation. In this case, the AC voltage (optimal frequency of 100 Hz) not only oscillates the bubble but also transports the oscillating bubble on the surface. However, the carrying efficiency is lower than the simultaneous actuations of acoustic excitation and EWOD.

The second type of object manipulation system utilizes the capturing phenomenon by oscillating bubble. The main feature is that the oscillating bubble is deposited on a 3-D traversing rod tip, rather than a two-dimensional surface. So, it allows for object manipulation in a 3-D space. It is concluded from multiple experiments that the maximum carrying speed is highest near the bubble resonant frequency, meaning that the capturing force is proportional to the bubble oscillation amplitude.

Finally, the cavitational streaming flow is extended to underwater propulsion. The key concept is to utilize the net momentum flux around the oscillating bubble. As a reaction force, the net momentum flux pushes or pulls the solid substrate on which the oscillating bubble sits. Using mini/micro glass rods, the propulsion mechanism is experimentally proved. The propulsion force is measured to be hundreds of nano-Newtons in a pendulum configuration.

TABLE OF CONTENTS

LIST OF TABLES

LIST OF FIGURES

NOMENCLATURE

θ	modified contact angle
θ_e	equilibrium contact angle
V	electrical potential
t	thickness of the dielectric layer
γ	interfacial tension
θ_{adv}	advancing contact angle
θ_{rec}	receding contact angle
θ_R	modified contact angle on a right side of a bubble
θ_L	modified contact angle on a left side of a bubble
w	width of the bubble base
$F_{driving}$	bubble driving force
P	bubble pressure
Δn	number of mole of generated gas
h	gap between the top and bottom plates
D	diameter of the bubble
F	Faraday number
c^*	average gas concentration
a	radius of the bubble

ω	angular frequency of applied acoustic wave
r	distance from the bubble center
$\Delta\phi$	phase shift between volume and translational oscillations
d	density
C	compressibility
K	kinetic energy density
P	potential energy
k	wave number
f	frequency
f_o	natural frequency
δ	Stokes layer thickness
F_r	radiation pressure force
F_v	Stokes drag force
η	medium viscosity
R_s	particle radius
U_s	velocity of the particle relative to the medium
μ	water dynamic viscosity
Δ	peak-to-peak oscillation amplitude at the bubble apex
ε	normalized bubble undulation amplitude ($\varepsilon = \Delta/a$)
ψ	streaming function
$\underline{n}$	surface normal vector

ACKNOWLEDGMENT

First of all, I thank Lord in heaven for all my achievements. I would like to express my heartfelt thanks to my wife – Jawon Ko – who has stood by me all the time and I love. I thank my parent who has mentally and physically raised me to achieve this honor. I am also very grateful to my sisters – Jieun, Limsoo, and Yoonjin. I would like to confess that my sons - Yongbin and Kihyun born in Pittsburgh are my consolation during Ph. D. study.

I am also thankful to Dr. Cho who has guided my research work and my Ph. D dissertation committee. Lastly I would like to thank lab mates – Yuejun, Yizhong, Kyongjoo, Sean, Pavin, Elias, Josh, Emily, Danny and other friends who I have known in Pittsburgh.

1.0 INTRODUCTION

1.1 EXISTING MANIPULATION METHODS

Manipulating individual micro-objects in millimeter- and micro scales has increasingly become an important task in many biomedical applications [1-4] and in micro assembling [5, 6]. The most frequent operations include capturing (immobilizing), transporting, rotating, and isolating individual objects. A micropipette is one of the most commonly used tools for micro-object manipulation [1, 4]. It is a small apparatus typically consisting of a micro- or nano-sized hollow tube through which vacuum is applied to suck and hold micro-objects. In addition, fluid can be delivered through the tube into micro-objects, if necessary. This method is an invasive manipulation involving direct contact between the pipette's solid tip and micro-objects.

As an advanced tool, optical tweezers have made non-invasive manipulation of biological objects possible [7-11]. Focused laser beams can trap micro-objects by imparting angular momentum on them and thereby suspending them in place. By moving the microscope stage or the focal point, the micro-objects undergo a relative displacement with respect to the surrounding. Although this non-invasive technique has been used for many research projects, such issues as incompatibility with objects and media, insufficient force, and bulky and expensive setup have often restricted its widespread applicability.

In addition, MEMS (Micro-electro-mechanical systems) technology has made many other manipulation methods possible. Using micro channel networks with controllable pressure sources and electrical inputs [12-16], micro-objects suspended in flow streams can be manipulated; however, the degree of freedom in the manipulation is limited due to the predefined channel network. Field forces such as electrophoresis [17-19], dielectrophoresis [20-24], magnetophoresis [25-27], and electromagnetophoresis can also be used to manipulate micro-objects. Recently, Chiou et al [21] reported an opto-electronic manipulator using low-power images where a massive number of micro cells were dielectrophoretically trapped, transported, and sorted simultaneously. Micro robotic grippers or cages [28-30] are another option that enables holding and manipulation of micro-objects via direct physical contact.

1.2 BUBBLE APPLICATIONS

In the present manipulation principles, a key component is an oscillating bubble serving as a carrier of micron- and millimeter-sized objects [31-33]. Since bubbles are ubiquitous in everyday life and have been one of the steady research topics for a long time, occupying an important place in physics, chemistry, engineering, medicine, and so on, one may want to see an overview on their past and current research activities and applications first. Some representative examples include: boiling process in energy generation, bubble injection in oil transport and production, gas-liquid reactors, floatation and separation of oils, minerals or biological cells, ink jet printers, and so on. In particular, in the past decades since the microfluidic technology emerged, micro bubbles have been drawing much more attention,

not only bringing a great deal of interesting scientific/engineering issues but also providing high potentials in many microfluidic applications.

In the early stage of the microfluidics era, bubbles were largely regarded as necessarily avoided in microfluidic devices since they often cause clogging problems in narrow microfluidic passages. It is not trivial to completely eliminate bubbles in microfluidic passages, thus requiring careful design of microfluidic passages as well as troublesome pre-treatments or pre-runs for bubble removal.

If favorably utilized, however, the micron-sized bubbles can be effective regulators or actuation sources for micro fluid flows. Hua *et al* [34] demonstrated that micron sized bubbles positioned in microchannel necks could be used for active valves that switched flows on and off as they were electrochemically grown and dissolved into the liquid. The interfacial tension in the bubbles was strong enough to overwhelm the hydrodynamic pressure in the microchannel. The bubble ink jet head [35] is one of the most successful bubble actuators where thermally grown bubbles directly push tiny liquid droplets out of the nozzles in a controlled fashion [36]. In some applications for flow pumping and regulation, bubbles are used in indirect ways. Bubble-induced motions and forces are transmitted through secondary parts such as cantilever beams [37], membranes [38-41] or conduits [16].

In addition to fluid control applications, bubbles can be used to control light paths. Jackel [42] may have been the first one to use bubbles to redirect and multiple arrays of light signals. Furthermore, bubbles have been recently exploited to manipulate micro particles and biological cells. Tayler and Hnatovsky [43] and continued work [44] demonstrated that bubbles thermally grown on an optical fiber tip could trap and mix particles as well as biological objects.

1.3 PROPOSED MANIPULATION PRINCIPLES

Figure 1 illustrates a fundamental configuration of the proposed 2-D micro manipulation technique that can be easily integrated on microscope glass slides [31]. Two physical principles are simultaneously applied to a gaseous bubble resting on a hydrophobic plate: acoustic forcing and electrowetting on dielectric (EWOD). The acoustic forcing oscillates (expands and shrinks) the bubble in harmony with the acoustic frequency. It is found that the bubble oscillation generates an attraction force and thus captures neighboring objects in certain conditions. Here, this phenomenon is utilized to trap and collect target objects. Then, in order to carry the captured objects from one place to another, EWOD actuation is applied to the oscillating bubble at the same time. Energizing individual, arrayed electrodes changes local wettability of the surface and thus pushes the oscillating bubble in the desired direction on a 2-D surface.

A series of operational steps is detailed as follows. When an electrical voltage is applied to a bubble generation electrode on a top glass plate of a chip filled with deionized (D.I.) water, a bubble is created electrochemically (electrolysis) and grown on the electrode while the voltage is applied, Fig. 1(a, b) [31]. When the growing bubble touches the bottom plate on which a hydrophobic layer is deposited, the bubble moves rapidly to the bottom plate due to the difference of the surface properties between the top and bottom plates. The voltage is turned off to stop bubble growth. Note that bubbles prefer to sit on the hydrophobic surface. Then, the piezo-actuator is turned on to oscillate the bubble. The oscillating bubble generates both so-called cavitational microstreaming flows and a radiation pressure force (to be exact, Bjerknes force) around the bubble (Fig. 1(c) [32, 45-47]). The radiation force can capture neighboring objects onto the oscillating bubble surface. The captured objects are carried in the desired direction while the bubble is being transported by sequential EWOD actuations (Fig. 1(d)) [32,

48, 49]. Note that the capturing force generated by the oscillating bubble is large enough to hold the objects during the lateral bubble movement [32, 50]. When the carried objects reach the destination, the acoustic excitation is turned off. So the bubble leaves the objects completely and continues to move other places by EWOD actuations (Fig. 1(e)). When the above operation is completed and the bubble is no longer necessary (Fig. 1(f)), the bubble needs to be eliminated electrochemically on a platinum catalyst electrode coated with a thin Teflon layer.

This micro-object manipulation method can provide more reliable and controllable object manipulating operations. One of the unique features is that the micro bubbles can be created and eliminated electro-chemically in an on-chip and on-demand manner and transported in any direction by programming and sequentially activating arrays of EWOD electrodes on a 2-D plane. Over such techniques as micropipettes and microcages/grippers, the present technique provides the advantages of non-invasive manipulation with soft contact between the bubble and objects, not solid-to-solid contact, thus possibly minimizing the mechanical damage on the object. As compared to the optical tweezers, this technique is highly cost-effective due to simple hardware structure. The major part is electrodes on flat plates, which are easily fabricated by the current micro photolithography.

The two-plate channel structure in Fig. 1 is the fundamental configuration for the proposed manipulation method. This thesis first focuses on development of the proposed 2-D manipulation method including individual bubble operations and investigation of their underlying phenomena. In Chapter 2, a particular emphasis is made on the operation of bubble creation and elimination in the two-plate channel structure, as prerequisite steps to completion of the proposed 2-D manipulation method. Then, complete operations of the proposed manipulation are achieved with characterizations in Chapter 3.

In Chapter 4, a similar 2-D manipulation method is presented. A main difference is that bubbles are oscillated only using alternating current (AC) EWOD. The manipulation in Chapter 3 requires not only EWOD actuation for the bubble transportation but also acoustic excitation by a piezo-actuator for capturing objects. It turns out that the single actuation of AC EWOD object can conduct both of these functions to some extent. This method can give more freedom in design than the manipulation method shown in Chapter 3.

The operations in the previous chapters are limited to 2-D space. In Chapter 5, a 3-D micro-object manipulation method is presented using the similar capturing mechanism. A major modification is that an oscillating bubble is attached to the rod tip connected to a three-dimensional traverse system, not on the 2-D flat surface. The bubble is oscillated similarly using the piezo-actuator attached beneath the water chamber. The oscillating bubble generates a radiation force and then captures micro-objects. As the rod tip is traversed in a 3-D space using a 3-D traverse system, the captured objects can be carried to a desired location. When the excitation is off, the carried objects are released from the bubble. This method uses the similar capturing mechanism for the 2-D case but provides mobility in a 3-D space.

As an exploratory work, a novel underwater propulsion method using oscillating bubbles is presented in Chapter 6. This method can be used to manipulate objects even larger than the oscillating bubbles. It is found that the cavitational microstreaming flow generated by oscillating bubbles has a net momentum flux. In other words, the oscillating bubble can push the objects on which the bubble sits. Proof-of-concept experiments along with characterizations for the propulsion are presented. This propulsion method is simple, yet can provide enough force to propel a small object without mechanical moving parts. In addition, the method does not need any electrical wiring but a remote acoustic excitation source. So it implicates such biomedical applications as propelling and maneuvering of diagnostic, drug-delivery, and surgery robots swimming inside blood vessels.

Finally, this thesis ends in Chapter 7 with an overall summary and future research recommendations.

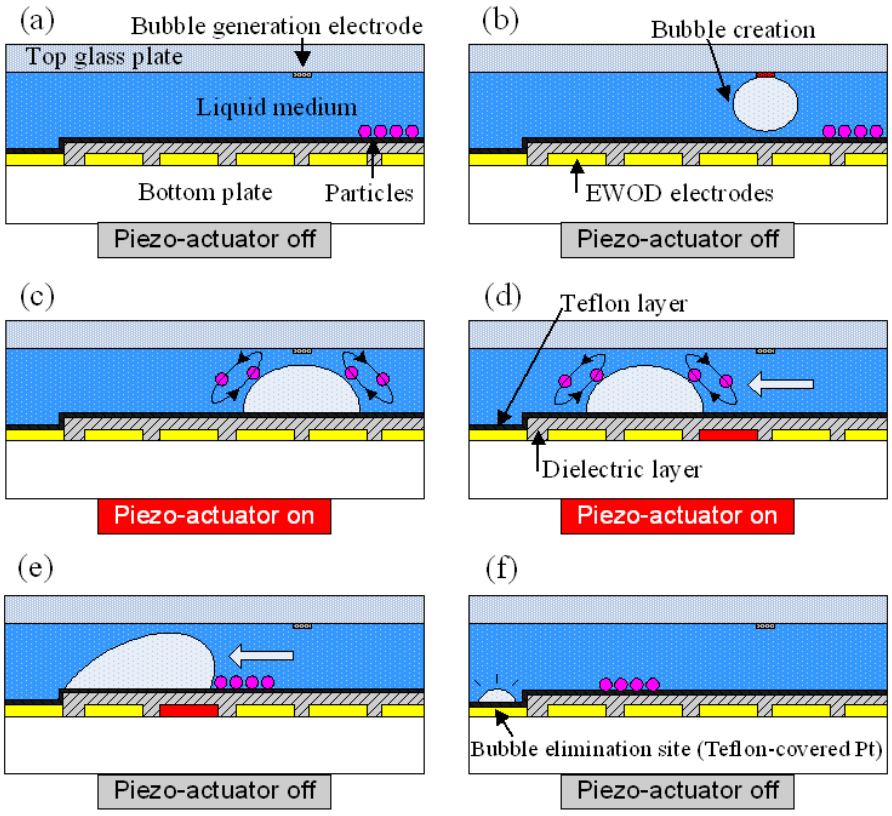

Figure 1 On chip micro particle manipulation by an oscillating bubble. (a)-(b) When an electric voltage is applied, a bubble is created on the bubble generation electrode of the top glass plate. (c) The piezo-actuator oscillates the gaseous bubble such that circulating flows are generated around the bubble, and then the neighboring objects are captured and orbiting in the circulating flows. (d) As EWOD electrodes are sequentially activated to the left, the bubble is moved left. Note that the piezo-actuator is still on while the bubble is moving. As a result, the captured particles are carried by the moving bubble. (e) When the piezo-actuator is off, the continued bubble transportation completely separates the captured particles from the bubble. (f) When the bubble is no longer necessary, the bubble can be eliminated electrochemically on a platinum catalyst.

2.0 ON-CHIP MICROBUBBLE MANIPULATION: CREATION, TRANSPORTATION, AND ELIMINATION

2.1 INTRODUCTION

To ensure that the platform envisioned in Fig.1 is fully functional, the platform should first be able to create microbubbles at desired times and positions within the chip. In addition, the created bubbles should be able to be transported to desired locations on a 2-D plane. Finally, the bubbles need to be eliminated on the chip if they have been used and are no longer needed. Otherwise, these bubbles would coalesce with other bubbles, blocking paths or generating unwanted flows under acoustic excitations. Zhao and Cho in our group previously introduced a simple method for bubble elimination in which the bubbles are moved to the air-liquid interface and then spontaneously eliminated. However, this method necessarily requires an air-water interface on the chip. This often makes chip fabrication and packaging more difficult.

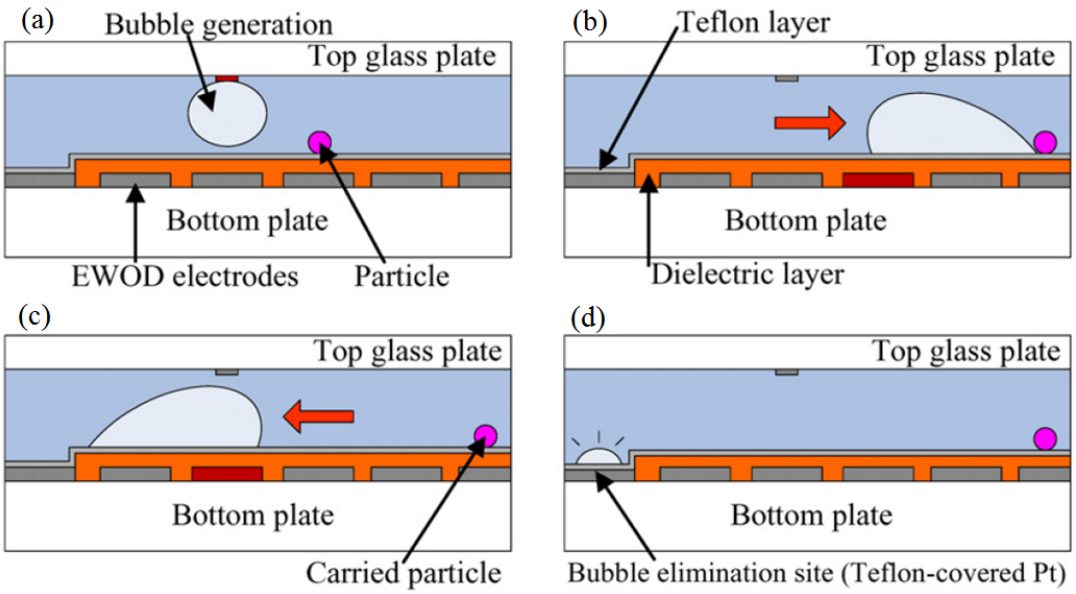

Figure 2 Schematic of bubble-based micro-object manipulator with three bubble operations: creation, transportation, direct manipulation, and elimination. (a-b) A bubble created from the top platinum electrodes by electrolysis can push a micro-object while being transported by EWOD. (c-d) If the bubble is not needed, it can be eliminated in the elimination site by a Pt-catalyzed electrochemical reaction. Note that the elimination platinum electrode is covered with a thin porous Teflon layer.

This chapter describes four different bubble operations – (i) creation of microbubbles, (ii) transportation of microbubbles, (iii) elimination of microbubbles, and (iv) direct manipulation of objects using bubbles – that can constitute a simplified scenario of bubble use and life in the envisioned platform. Here, the direct manipulation means that moving bubbles can push or pull the micro objects to reposition them, as shown in Fig. 2. These operations are successfully accomplished by integrating electrolysis and EWOD principles. Electrolysis is employed for bubble creation and elimination at designated sites. EWOD is used for bubble transportation to and from designated sites and also for object manipulation. This chapter places particular emphasis on the bubble elimination process by examining a wide range of elimination

conditions. Note that the present bubble elimination method does not require any air-water interfaces, only a simple planar structure of platinum electrode coated with a thin Teflon layer.

2.2 THEORETICAL BACKGROUND

2.2.1 Electrochemical reaction (electrolysis)

Electrolysis of water is a process that breaks water molecules into hydrogen and oxygen molecules using electricity [51, 52]. For this process, an electrically-closed electrochemical cell needs to consist of a power source and two electrodes (anode and cathode) that are necessarily immersed in water. The overall reaction process consists of two major steps. The first one is known as autoprotolysis that is described by $2H_2O \Leftrightarrow H_3O^+ + OH^-$. Thus, in pH neutral water, there are constant supplies of H^+ (or H_3O^+) and OH^- ions in any given conditions. The next step involves reactions on each electrode converting hydrogen and hydroxide ions in water into gases: $2OH^- \rightarrow O_2$ (gas) + $2H^+ + 4e^-$ (on anode) and $H^+ + 2e^- \rightarrow H_2$ (gas) (on cathode). For a given applied current or voltage, the created bubble size can be time-controlled. Meanwhile, in order to eliminate the created oxygen and hydrogen gases, the above reactions on the electrodes can be reversed. However, this reverse process must overcome a high energy barrier. One of the most common and efficient methods to lower the energy barrier is to use a platinum catalyst at the electrodes. In this case, the created bubbles can be quickly eliminated on the platinum electrodes.

Compared to thermal bubble generation, this electrolytic method provides many advantages: low power consumption, generation of room-temperature bubbles, and large force generation. Thus, the electrolytic method has been employed in many microfluidic bubble

actuators - such as microvalves [52, 53], micropumps [41], microdosing systems [54], cell sorting [55]- as well as in large scale applications [56].

In many of these micro actuators, elimination of the created bubbles was also required in order to continuously cycle actuations. In this case, a simple design is to have bubbles created and eliminated on the same platinum electrodes (anode and cathode) without any separation of bubbles from the electrodes. In most of the applications, hydrogen-oxygen mixture bubbles were created and eliminated across the same platinum electrodes by turning the applied electric input on and off. In the present microfluidic platform, however, the created bubbles should be first moved from the creation sites for the use of micro-object manipulation. In this case, the bubble size can be maintained nearly constant for a period of time without further growing or shrinking on the platinum electrode. In addition, when they are no longer needed these bubbles should be eliminated at a different location than where they were created. The use of a different electrode for elimination gives more flexibility in the design of creation and elimination electrodes. The bubble creation electrodes are sharp and tip-shaped whereas the elimination electrode is simply a rectangular planar electrode. Sharp vertices of the electrodes concentrate the electric field and provide geometrical singular points. Therefore, bubbles are nucleated and created more likely at the vertices. As shown in the results section, the creation electrodes are bare platinum electrodes while the elimination electrode is covered with a thin, porous Teflon layer. The porous Teflon layer is required on the elimination electrode not only to make bubbles easily transported by EWOD to the elimination site but also to shorten the total elimination time.

2.2.2 EWOD principle

Lippmann [57] first recognized over 100 years ago that an externally added electrostatic charge may significantly modify the capillary forces at an interface. However, this phenomenon had not drawn much attention until MEMS technology emerged. Recently, however, many reports have shown that the phenomenon also prevails in configurations where the electrode is covered with a thin dielectric layer [48, 49, 58, 59] (Fig. 3). The wettability of liquids on a dielectric surface can be electrically controlled with high reversibility in many cases, as illustrated in Fig. 3. Here a droplet is taken as an example rather than a bubble since most of the previous efforts have been made on millimeter-sized droplets. When an electric voltage V is applied between the aqueous sessile droplet and the electrode, the droplet spontaneously spreads out on the dielectric surface. Note that the contact angle θ is decreased (Fig. 3(b)), as a result. However, when the electric potential V is removed, the contact angle returns to its initial state. This phenomenon, known as electrowetting (to be exact, electrowetting on dielectric or EWOD), has outstanding features: (1) excellent reversibility; (2) extremely low power consumption (less than μW) since the dielectric layer acts like a capacitor, not an energy dissipation device; and (3) superb robustness since there is no direct electrochemical interaction between the electrode and the liquid.

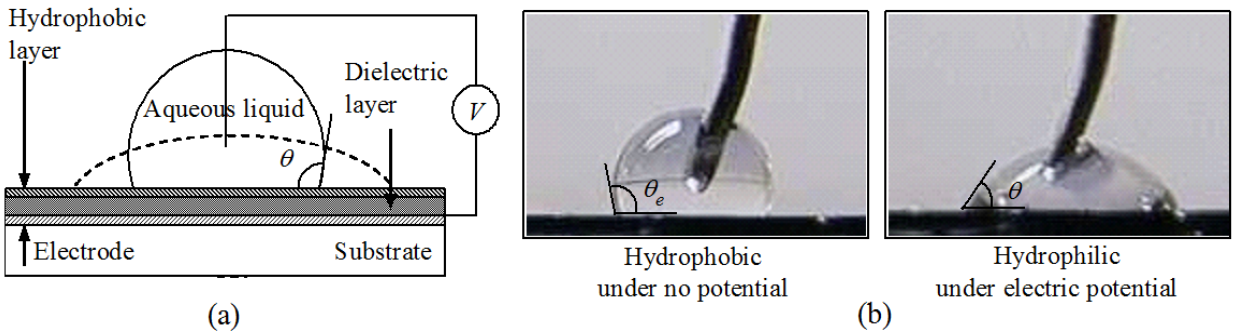

Figure 3 Principle of electrowetting on dielectric: (a) Schematic configuration; (b) Pictures of basic electrowetting demonstration on a sessile drop from Cho et al [60].

The relation between the contact angle change and externally applied electrical potential may be derived from the Lippmann equation employing the parallel-capacitor approximation for the dielectric layer. It can be alternatively derived by way of the minimum free-energy requirement for thermodynamic equilibrium conditions, as follows:

$$\cos\theta = \cos\theta_e + \frac{\varepsilon V^2}{2\gamma t} \tag{1}$$

where θ is the contact angle under the externally applied electrical potential V, θ_e is the equilibrium contact angle at V= 0 V, ε is the permittivity of the dielectric layer, γ is the interfacial tension between the droplet and surrounding fluid, and t is the thickness of the dielectric layer. This equation shows that the cosine of the contact angle can be parabolically modulated by the applied electric potential. In many configurations of millimeter-sized droplets, empirical results on contact angles have been successfully correlated to Eq. (1) within a moderate range of the contact angle. Other theoretical approaches such as Maxwell stress analysis [61] of electrostatic

force and electromechanical framework [62] also confirmed Eq. (1), although there is currently an argument on the origin of contact angle change.

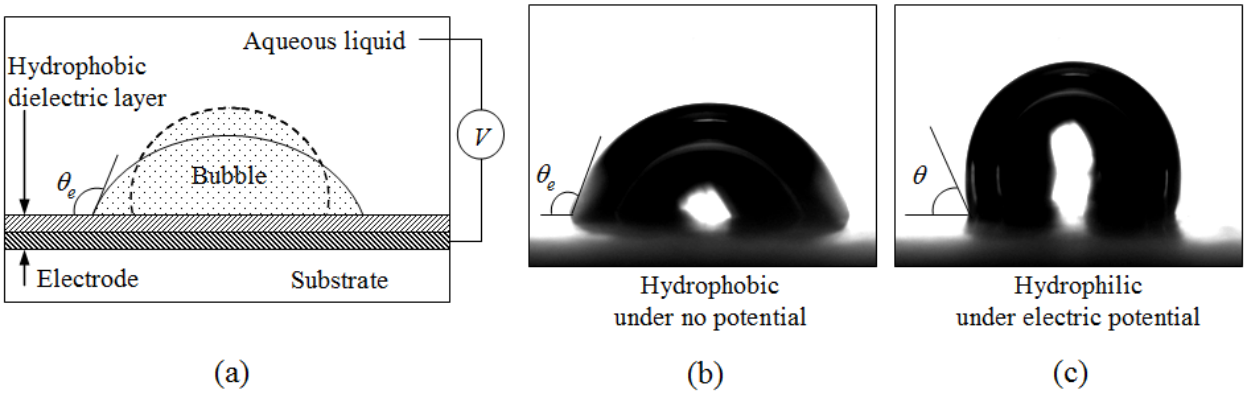

Figure 4 Preliminary results of electrowetting principle with an air bubble. The bubble retracts under electric potential and reversibly spreads back to the initial state under no electric potential: (a) configuration; (b) no electric potential applied; (c) electric potential applied.

Meanwhile, consider a gas or oil bubble in an aqueous environment in a similar configuration (Fig. 4). Note that the contact angle is also defined in the aqueous liquid side (Fig. 4a). Likewise, the contact angle of the bubble in an aqueous liquid can be modulated by the electrowetting principle. Contrary to the droplet configuration, the bubble would retract under an electric potential since the contact angle decreases, and return back with no electric potential.

2.2.3 Bubble transporting

In order to move bubbles on a solid surface, the bubbles need to overcome the adhesion force caused by contact angle hysteresis [51, 63-65]. Figure 5 shows macroscopic sketches of how a bubble placed over an array of electrodes behaves in response to electrowetting actuations and

contact angle hysteresis. As denoted by the broken line in Fig. 5a, the bubble initially sits on a dielectric surface in such a way that the right side of the bubble is placed over the second electrode from the right. Here, the contact angles on both sides of the bubble are equal to the equilibrium contact angle θ_e. The activation of the electrode on the right of the bubble would decrease the contact angle θ_R on the right side of the bubble according to Eq. (1), while the contact angle θ_L on the left side of the bubble would slightly increase due to the deformation of the bubble. Note that all the contact angles are referred to as the macroscopic apparent contact angle, not microscopic intrinsic contact angle, and the contact angles are always measured from the water side. The three-phase contact lines (TCL) on both the right and the left sides of the bubble do not move although the bubble is deformed in shape. As a result, there is no sliding movement in the bubble (Fig. 5a).

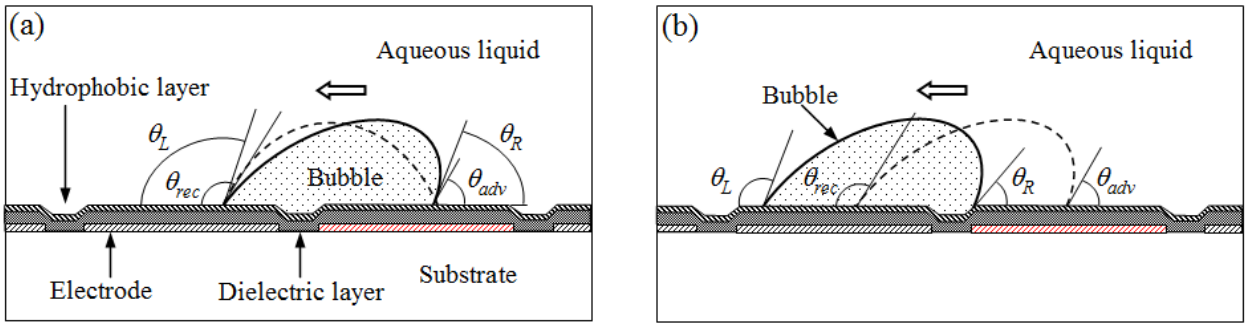

Figure 5 Sequential sketches of droplet and bubble transportation: (a) Immediately after the first electrode on the right of the bubble is activated, the bubble is deformed but does not move since the contact angles (θ_L and θ_R) on the left and right sides of the bubble are still within the contact angle hysteresis range (i.e., $\theta_L < \theta_{rec}$ and $\theta_R > \theta_{adv}$ for the bubble); (b) Once the contact angles pass over the critical angles (θ_{adv} and θ_{rec}) by electrowetting, the bubble starts to move.

This lack of movement is due to contact angle hysteresis (difference between θ_{adv} and θ_{rec}) [51, 63-65]: in order for the TCL to advance or recede, the contact angle needs to pass over critical values (θ_{adv} and θ_{rec}) which are different from the equilibrium contact angle θ_e. These critical angles are referred to as the advancing contact angle θ_{adv} and the receding contact angle θ_{rec}, respectively. Many physical parameters could play a role in the occurrence of this phenomenon, such as the surface roughness and the degree of heterogeneity of the surface, and so on. Only if the contact angle θ_R is lower than the advancing contact angle θ_{adv} and the contact angle θ_L is higher than the receding contact angle θ_{rec}, the bubble will start to move to the left. These conditions require a large span of the contact angle modulation by electrowetting actuations for the initiation of bubble motion.

By considering the static mechanical equilibrium [64, 66-68], the bubble driving force $F_{driving}$ produced by electrowetting actuation may be approximated as follows:

$$F_{driving} = 2\gamma w \sin\left(\frac{\theta_L + \theta_R}{2}\right)\left(\cos\theta_R - \cos\theta_L\right) \tag{2}$$

where γ is the interfacial tension between the liquid and the bubble and w is the width of the bubble base which linearly scales with the radius R of the bubble. Here, the contact angle θ_R of the bubble is modulated by electrowetting actuation, decreasing from the equilibrium contact angle θ_e with a large span (generally ~40^o). Therefore, the sine term in Eq. (2) can be roughly approximated to the sine of the equilibrium contact angle θ_e, while the difference of the cosines in Eq. (2) increases as the contact angle θ_R for the bubble is decreased by electrowetting modulation. Based on this, it can be concluded that the maximum driving force can be achieved

when the equilibrium contact angle is close to 90^o and the contact angle modulation is maximized by electrowetting actuation. This force can be in the μN range. For example, when $\theta_R = 60^o$ and $\theta_L = 120^o$, with an air bubble of 10 μm diameter in water, the driving force is roughly estimated to be of the order of 1 μN, more than four orders of magnitude stronger than the other actuation forces such as optical tweezers, dielectrophoresis, and so on.

The equilibrium contact angle θ_e is determined by the interfacial tensions among solid, liquid, and bubble phases. Therefore, it is critical to choose proper materials for the three phases such that the equilibrium contact angle is close to 90^o, and it is more important that the contact angle modulation is maximized by electrowetting actuation. In addition, there is a necessary condition to initiate the bubble motion; the contact angle hysteresis should be as small as possible. It is worthwhile to note that the driving force linearly scales with the bubble size R according to Eq. (2), thus dominating other forces that scale in the second or higher order with the characteristic length.

Sequential actuations of an array of electrodes can produce continuous movements along a programmed electrode path. Some bubble operations such as transporting, merging, and splitting of micro and millimeter sized air bubbles in DI water have been demonstrated in our group [50, 69].

2.3 FABRICATIONS AND EXPERIMENTAL SETUP

In order to examine the above bubble operations, testing devices that consist of two parallel plates (top and bottom) are fabricated using standard lithographic micro fabrication technology, as shown in Fig. 6. The bottom plate contains an array of EWOD electrodes and a bubble

elimination platinum electrode whereas the top plate has bubble generation electrodes (anode and cathode) and an EWOD ground electrode. The main fabrication process for the bottom plate consists of three steps: metallization and patterning of electrodes (Fig. 6a), deposition and patterning of a dielectric layer (Fig. 6b and c), and deposition of a hydrophobic layer (Fig. 6d).

For the EWOD driving and bubble elimination electrodes, a platinum layer of 1500 Å in thickness along with a chromium adhesion layer of 100 Å in thickness is sputter-deposited on a glass wafer and then patterned by wet etching (Fig. 6a). Each EWOD driving electrode is square in shape with a side length of 250 μm. In addition, larger EWOD electrodes (1.4×1.4 mm^2) are also designed only for object manipulation. The bubble elimination electrode positioned next to the edge of the EWOD electrode array is of rectangular shape (500×1160 μm^2). For the EWOD dielectric layer, a 3-μm thick photoresist (AZ4210, Clariant Co.) layer is spin-coated on the entire top surface of the bottom plate (Fig. 6b). To ensure the elimination electrode contact with bubbles, a rectangular window (500×1160 μm^2) is opened through the photoresist layer by a developing process (Fig. 6c). Finally, the bottom plate is coated with a hydrophobic Teflon layer (Fig. 6d).

In this case, note that the bubble elimination platinum electrode is in contact with bubbles through the porous Teflon layer. In order to examine the effects of the Teflon layer thickness on bubble elimination, three Teflon layers with different thicknesses (400, 1200, and 2000 Å) are tested along with a bare platinum electrode. The layer thickness is controlled by adjusting the Teflon concentration in the spin-coating solution (Teflon AF 1600® (DuPont) + solvent (FC-75, Acros Organics)).

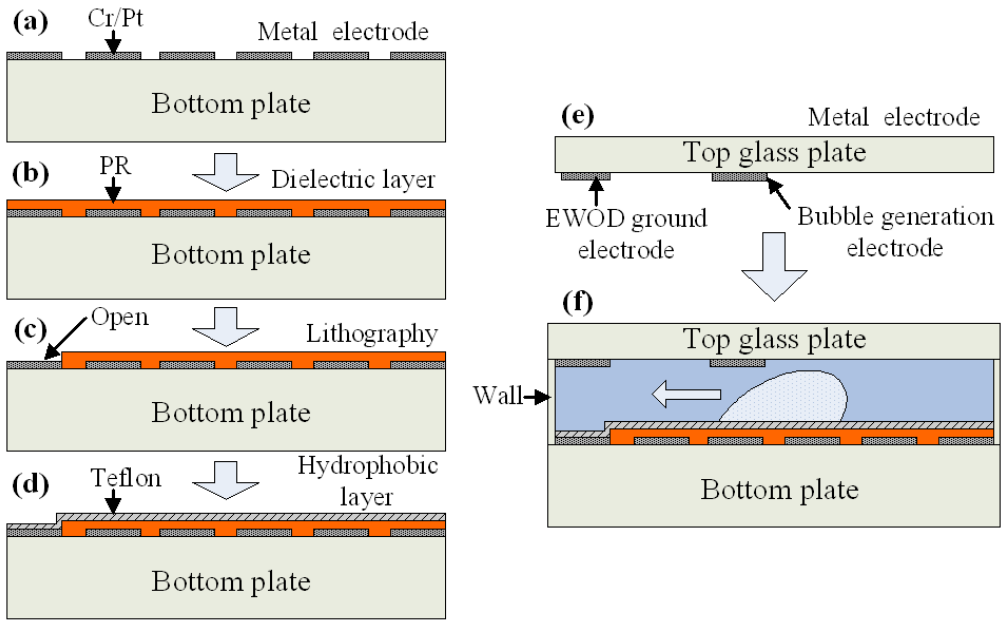

Figure 6 Microfabrication steps of testing device: (a) Metallization and patterning of electrodes (Cr/Pt) on the bottom plate; (b-c) Deposition and patterning of a photoresist layer on the bottom plate; (d) Deposition of a Teflon layer on the bottom plate; (e) Metallization and patterning of electrodes (Cr/Pt) on the top plate (f) Integration of the top and bottom plates with walls in between.

The top glass plate fabrication consists of metallization and patterning of the EWOD ground and anode/cathode electrodes. A platinum layer of 1500 Å in thickness along with a chromium adhesion layer of 100 Å in thickness is sputter-deposited on a glass wafer and then patterned by wet etching (Fig. 6e). The EWOD ground electrode is a 100-μm wide line electrode in direct contact with water whereas the sharp tip-shaped anode and cathode are pointed toward each other with a 5-mm (called electrode I) or 40-μm (called electrode II) separation distance. A sharp tip-shape is used for the anode and cathode for more accurate bubble-creation control.

The top and bottom plates are individually used for bubble creation and elimination, respectively; however, for the integrated bubble operation of creation, transportation and elimination, the two plates are integrated as shown in Fig. 6f. After putting a large water droplet

on the bottom plate, the top plate is gently pressed against the walls that are placed on the bottom plate. Multiple layers of double-sided tape (about 100 μm thick each) are used for the walls to confine the water in place and served as spacers. Unless particularly specified, the filtered water solution tested in this paper has a conductivity of 20 mS/cm and pH 6.7.

Figure 7 illustrates how to generate activation signals to drive droplets/bubbles in the microfabricated EWOD chip. The entire system consists of a personal computer, a digital output board, and a custom-made interface circuit. The schematic of the activation signal flows is shown in Fig. 7a. The digital signal from the computer through the digital board switches the relays that provide the high EWOD voltages to the electrodes in the testing device. A PC-based program coded using the C language or LabView® controls the digital I/O board (e.g., DAQPad-6507, National Instrument) generating on/off signals in each bit. Since the signals from the digital I/O are 0 or 5 V, it cannot be directly connected to the EWOD electrodes which requires typically 30 ~ 150 V AC or DC for droplet or bubble driving. For this reason, the digital output signal is used as the input to the photo-coupled relay (PhotoMos®, AQW614EH, Aromat Co.) which switches high voltage signals according to the combination of the digital signal bits. Here, one side of the relay is connected to the digital signal and the other side is connected to the EWOD electrode and a high-voltage power source, as shown in the middle figure in top in Fig. 7b. For the high voltage source, a DC or sine wave voltage is generated by a function generator (33220A, Agilent Co.) and amplified using a voltage amplifier (PZD700, TREK, Co.). The digital signal entered in the relay is photo-coupled with the high voltage side and switches the high voltage source connected to the EWOD electrodes.

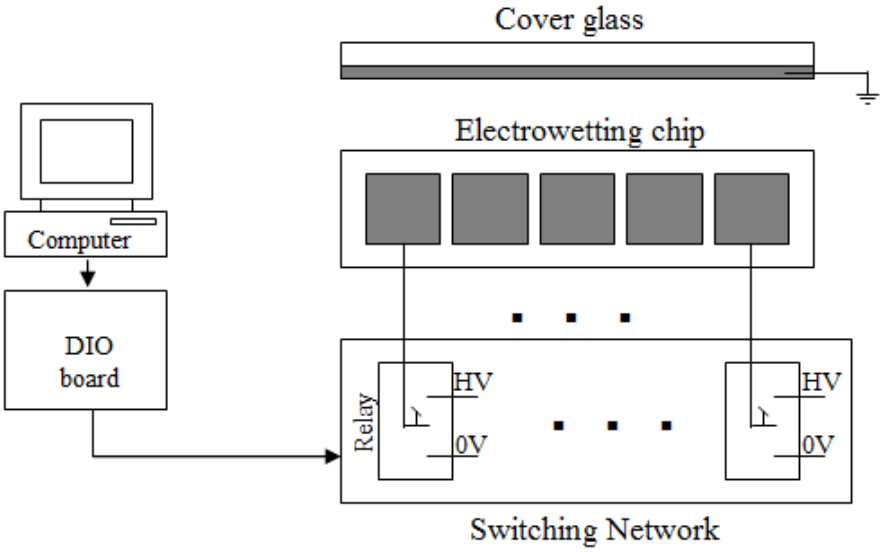

(a)

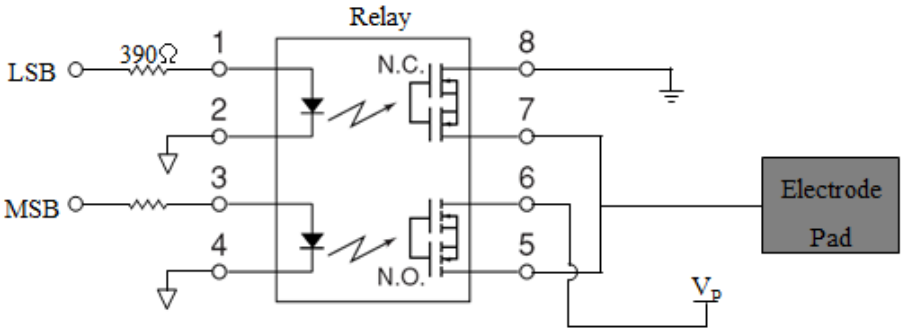

The relay working condition

MSB	LSB	STATUS
0	0	GND
1	1	HIGH
0	1	FLOAT
1	0	SHORT (Prohibited)

(b)

Figure 7 Schematic of droplet or bubble driving system setup. (a) Schematic of activation signal flows, (b) Photo-coupled relay (PhotoMos®, AQW614EH, Aromat Co.) for high voltage switching to the EWOD chip and relation between digital signal from DIO board and the voltages to the EWOD chip.

The table in Fig. 7b shows that each EWOD electrode can be set at three different states (ground, high voltage, and float) depending on the two-bit signal from the digital I/O board. For example, if both bits of the digital signal are on (i.e., 1, 1), the photo couplers in the relay transmit the digital signal, thus connecting the EWOD electrode to the high voltage source. To set the EWOD electrode at 0 V, both bits in the digital output signal need to be 0 V. As a result, the number of required bits is twice the number of EWOD electrodes in this circuit. Figure 8 shows pictures of experimental setup. Motions of droplets or bubbles are real-time imaged using a microscope and a DV-tape recorder. In Fig. 8a, the top view of the EWOD chip is shown on the computer monitor.

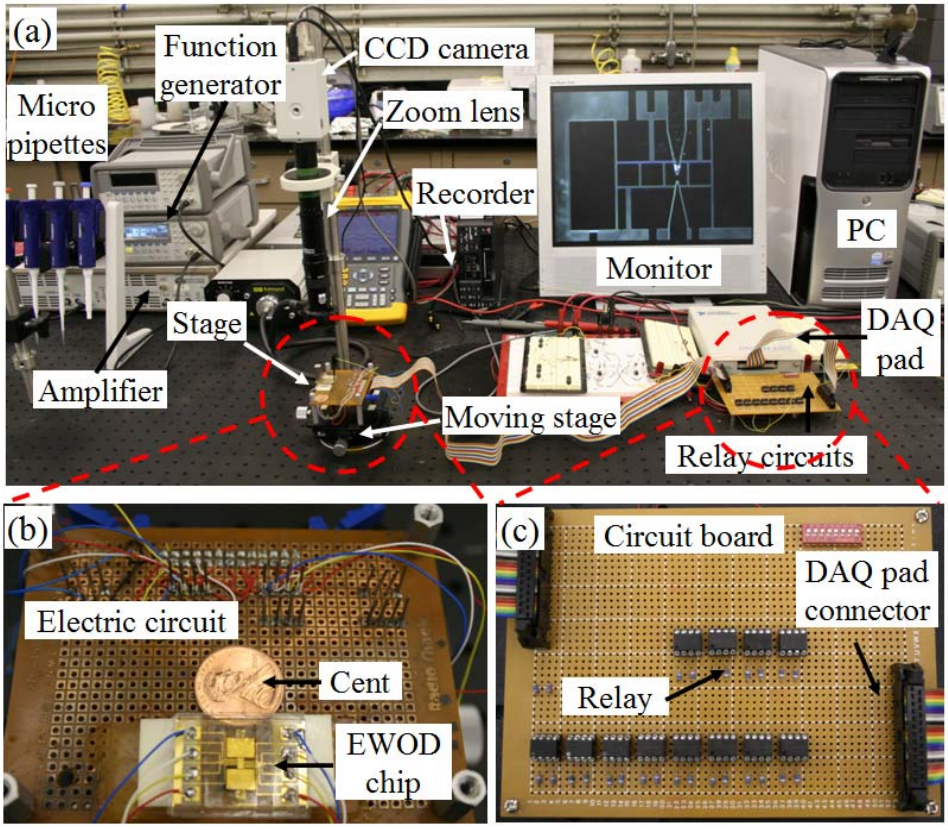

Figure 8 Experiment set-up: (a) Experiment configuration; (b) Installed EWOD chip; (c) Relay circuit board.

2.4 RESULTS AND DISCUSSION

2.4.1 Microbubble creation and transportation

Before integrating EWOD bubble transportation with bubble creation, the electrolytic bubble generation is examined first for two different electrode configurations. The first one (called electrode I) positions the anode and cathode 5 mm apart such that hydrogen and oxygen (or chlorine) bubbles are separately generated at the cathode and anode, respectively. Such a large distance is chosen in order to prevent any possible cross influences between oxygen and hydrogen bubbles via diffusion or convection through the liquid medium. The separately generated bubbles are later compared with the mixture bubbles to study the elimination speed. The second configuration (called electrode II) positions the anode and cathode in close proximity (40 μm distance) such that the bubbles are created as a mixture of hydrogen and oxygen gases.

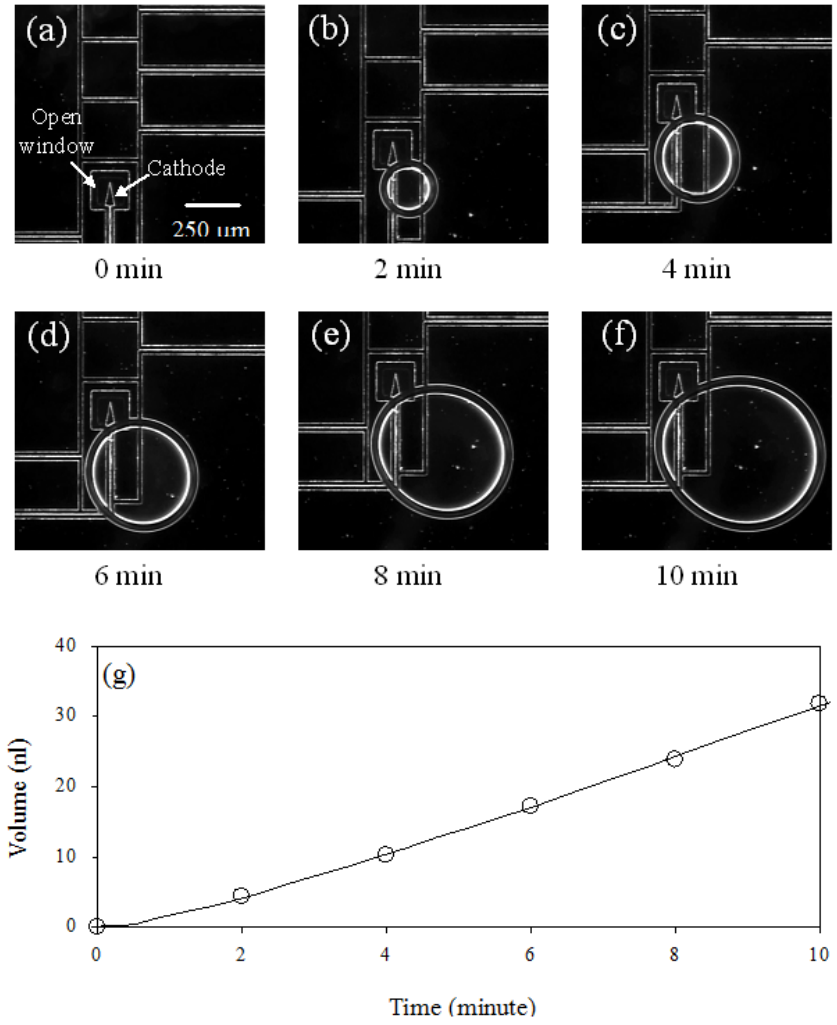

Figure 9 Creation of hydrogen bubble. (a-f) sequential images and (g) volume of micro hydrogen bubble generation by electrolysis. The cathode and anode electrodes are placed 5 mm apart (anode not shown). In a NaCl aqueous solution (conductivity 720 mS/cm), a hydrogen bubble nucleates on the cathode and grows up to 700 μm diameter at a constant voltage of 4 V. Note that the data are curve-fitted using Eq. (1).

For electrode I, the experiment is first conducted by immersing the entire top plate in a water chamber ($5 \times 5 \times 2$ cm^3). In this case, the top plate with the bubble-generation electrode faces up and is attached to the bottom of the chamber. To confine the created bubbles, another glass plate is placed over the top plate. The gap between the top plate and glass plate is set at

about 100 μm using spacers in between. The entire surface of the top plate is covered with a 3-μm thick photoresist layer except the triangular areas of the cathode and anode electrodes (Fig. 9a). Preliminary tests show that the large distance (5 mm) between the anode and cathode requires the application of high voltages. To reduce the applied voltage, a small amount of NaCl electrolyte is added into a D.I. water chamber. As a result, the solution has the conductivity of 720 mS/cm and the pH value of 6.7. In this reaction, hydrogen bubbles are created on the cathode whereas chlorine bubbles are formed on the anode. Figure 9 shows sequentially captured images of hydrogen bubble creation with corresponding volumes. When a voltage (4 V) is applied between the cathode and anode, a hydrogen bubble nucleates at the cathode and grows up to 700 μm in diameter under constant voltage. A chlorine bubble (not shown here) is also generated on the anode. As shown in Fig. 9g, the volume of the created hydrogen bubble V is well-defined by time t, the relation for the case of constant applied current I (or constant voltage) may be described as:

$$t = aV + b\sqrt{V} \tag{3}$$

where the coefficient a and b are determined from the experimental data since the current is too low to be resolved by our available instruments. Equation (3) may be derived by combining Faraday's law ($\Delta n = \frac{3}{4F}\int_0^t Idt$), the ideal gas law ($PV = \Delta nRT$), the Young-Laplace equation ($P = \gamma(2\cos\theta/h + 2/D)$), and the geometrical relationship of the bubble volume ($V = \pi D^2 h/4$). Here, F is the Faraday number (= 9.6486×10^4 C mol^{-1}), P is the bubble pressure, Δn is the number of

moles of generated gas, h is the gap between the top and bottom plates, γ is the surface tension (0.072 N/m), θ is the contact angle on the plates, and D is the diameter of the bubble.

For the configuration of electrode II, sequentially captured images of bubble-generation are shown in Fig. 10a-f. The top plate with the electrodes faces down and placed over the glass substrate with a gap of ~ 100 μm. Created bubbles are confined in the gap between the top plate and substrate. As shown in Fig. 10b, hydrogen and oxygen gases are generated on the cathode and anode, respectively, as soon as a voltage (6.2 V) is applied between the cathode and anode. Since the distance between the cathode and anode (40 μm) is very small, a mixture bubble of oxygen and hydrogen immediately forms at the gap and continues to grow, exceeding 700 μm in diameter under the fixed voltage condition. The rate of bubble generation can be controlled by altering the applied voltage or current. However, it is observed that voltages higher than 6.2 V make controlling of the bubble size difficult. A large number of small bubbles (< 10 μm in diameter) were generated from the tips and floated away in the water. Figure 10g shows the volume of generated bubbles vs. time. Similar to the configuration of electrode I, the bubble size can be easily controlled by time, and the volume-time relationship can also be nicely curve-fitted by Eq. (3) over the range of several minutes tested. In general, a smaller distance between the cathode and anode reduces the required voltage and improves the reliability of the bubble generation. In addition, a smaller area of the electrodes minimizes multiple bubble generations and enhances controllability. Therefore, if there is no need for separate gas bubble creation, electrode II is preferable over electrode I.

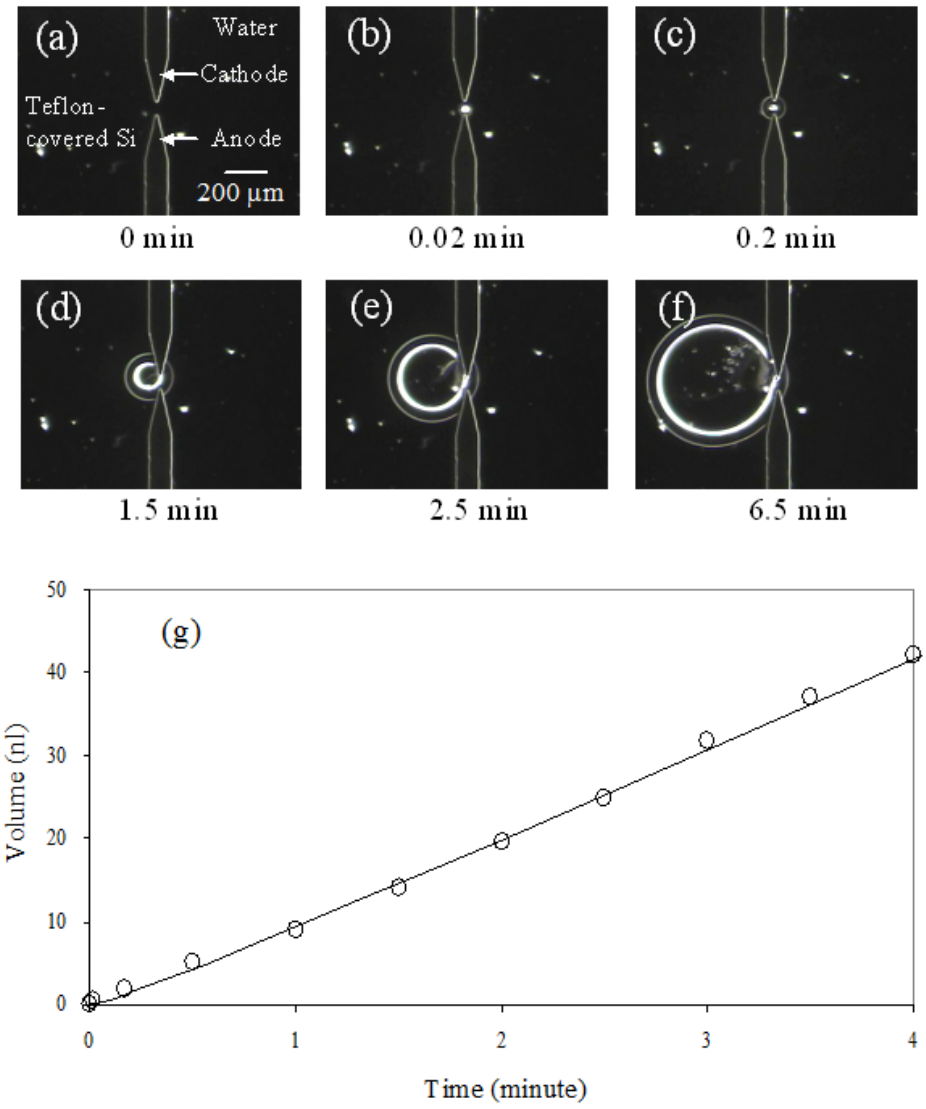

Figure 10 Creation of hydrogen-oxygen mixture bubble. (a-f) The cathode and anode are placed on the top plate in close proximity with a separation distance of 40 μm. When a voltage (6.2 V) is applied between the cathode and anode, a hydrogen-oxygen mixture bubble is created at the tips of the electrodes and grows. (g) The bubble size is controlled by time under the constant voltage applied, ranging from 0 to 700 μm in top view diameter (0 to 45 nl in volume). Note that the data are curve-fitted using Eq. (1).

After characterizing the bubble creation behaviors for given conditions, the bubble creation is integrated with bubble transportation. Figure 11 shows captured images of successive

bubble creation and transportation in the configuration of electrode II. A similar integration in electrode I has been done [32], although the results are not shown here. As described in the fabrication section, the electrolysis electrodes are placed on the top plate while the EWOD electrode array is placed on the bottom electrode. Note that the top plate is made transparent for visualization except the area of the cathode and anode.

First, when a voltage (6.2 V) is applied between the cathode and anode, the first bubble is generated at the gap between the cathode and anode and then continues to grow large enough to touch the bottom plate. As soon as the bubble touches the bottom plate, it is automatically transferred from the top plate to the bottom plate (Fig. 11b). Here note that the top plate is hydrophilic (glass surface) while the bottom plate is hydrophobic (Teflon-covered). Generally, the bubble has a tendency to attach to more hydrophobic areas. Once the bubble is transferred onto the bottom plate, the bubble growth stops due to separation from the anode and cathode.

The EWOD electrode directly underneath the tips of the cathode and anode is energized first, as a result, pushing the bubble to the left. Shifting activations of the EWOD electrodes causes the bubble to be continuously transported to the left end of the EWOD electrode array (Fig. 11c). The average bubble speed is measured at ~ 4 mm/s. Similarly, the second bubble is generated and transported, but takes a different path (goes down first and then left in Fig. 11d & e). Then, when the second bubble reaches the first bubble, it merges with the first bubble (Fig. 11f). By repeating this process, we can generate multiple bubbles with a fine control. The three generated bubbles are of nearly equal size. Figure 11h shows a large bubble formed by merging the three bubbles. These results demonstrate that the integration of electrolysis and EWOD enable reliable generations and transportations of microbubbles for the micro-object manipulation platform.

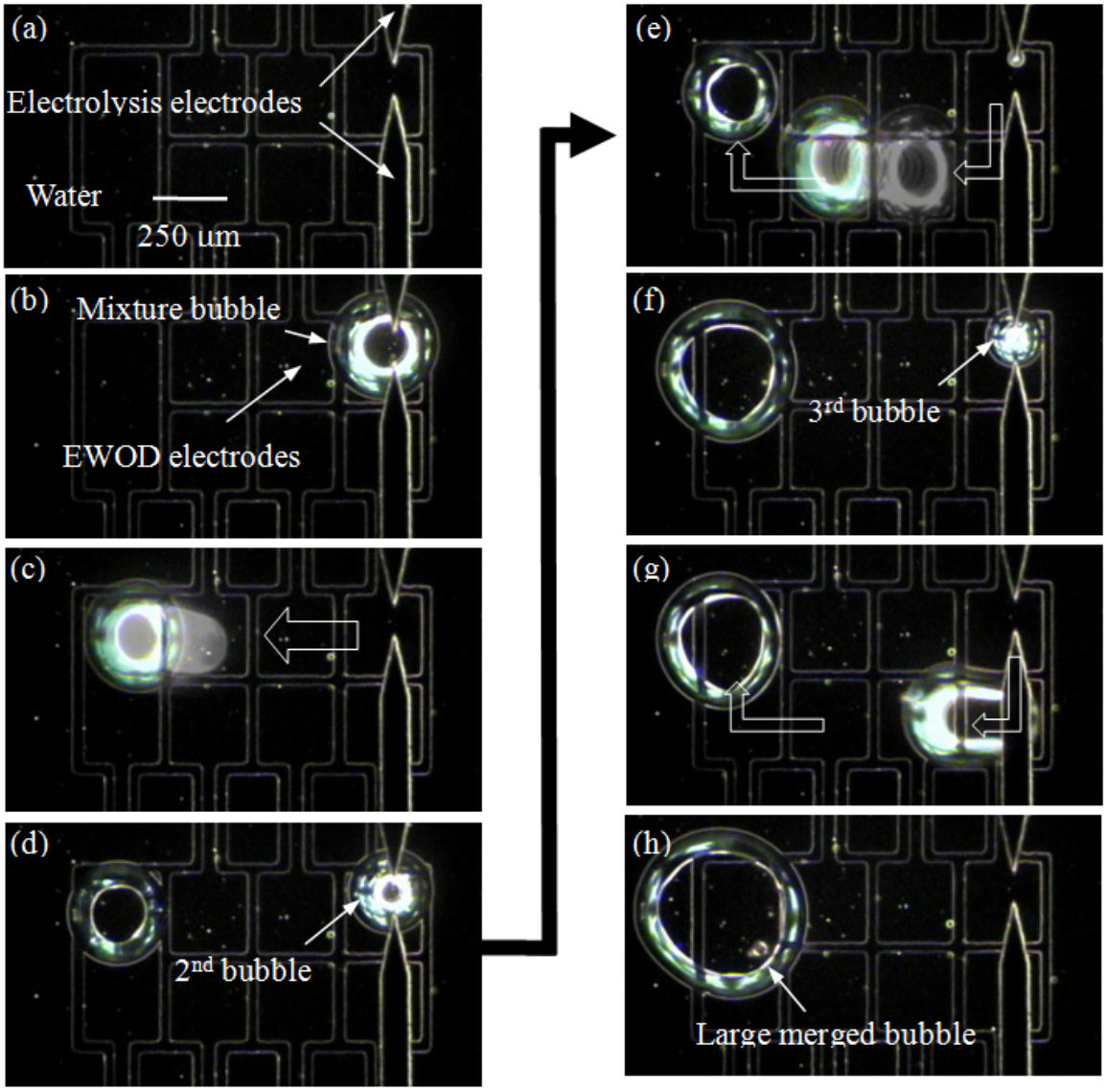

Figure 11 Sequential images of successive generation and transportation of hydrogen-oxygen mixture bubbles. (a-b) The first bubble is generated and grown on the top cover plate by electrolysis. Once the bubble touches the hydrophobic bottom plate, it is automatically transferred to the bottom plate on which the EWOD electrode array lies. (c-e) The bubble is transported to the left end by EWOD, and the second bubble is created again, transported, and merged with the first bubble. Note that the second bubble takes a different path from the first one (moves down first and then left). (f-h) Likewise, the third bubble is generated, transferred, and merged. The large bubble is formed by merging the three created bubbles that are of nearly equal size.

2.4.2 Elimination of microbubbles

Bubble elimination is one of the key operations in the present manipulation platform and in many microfluidic devices. Papavasiliou [52] used a combustion reaction process between oxygen and hydrogen gases in the microbubbles. Due to extremely high heat transfer rate in the microscale, however, the flame that was initially ignited by an electric spark could not be sustained but disappeared immediately. An easier and more reliable method for bubble elimination is to reverse the electrolytic bubble generation process. However, the reverse reaction between hydrogen and oxygen to form water does not take place automatically due to the energy barrier. The energy barrier can be lowered by a catalyst [51]. Among the many choices, platinum is one of the most commonly used catalysts. In the reverse electrolysis, the platinum catalyst can dissociate hydrogen gas into hydrogen atoms that react far more rapidly with oxygen gas molecules. Since the reverse reaction takes place between solid catalysts and gas reactants [51, 52] on the platinum electrode surface, as opposed to in the liquid medium, it is called heterogeneous catalysis.

For this catalytic reaction, a platinum electrode is placed separately in a designated elimination site on the substrate. The overall process for bubble elimination consists of two consecutive operations: i) bubble transportation to the elimination site and ii) bubble shrinking by the catalytic reaction. To ensure that bubbles are completely and rapidly removed, they should be placed on the platinum electrode with a maximized contact area; however, it is found that bubbles cannot be transported to bare platinum electrodes by EWOD actuation since they have a strong tendency to stay on the hydrophobic area. The bare platinum electrode is much more hydrophilic than the Teflon layer that covers the EWOD electrodes. EWOD is not strong enough to move bubbles from the hydrophobic Teflon surface to the hydrophilic bare platinum electrode.

One possible method to circumvent this problem is to cover the bare platinum electrode with a thin Teflon layer. It is known that the spin-coated thin Teflon layer is amorphous and, more importantly, highly porous [70] such that the catalytic reaction can be made via gas molecule exchange through the thin Teflon layer.

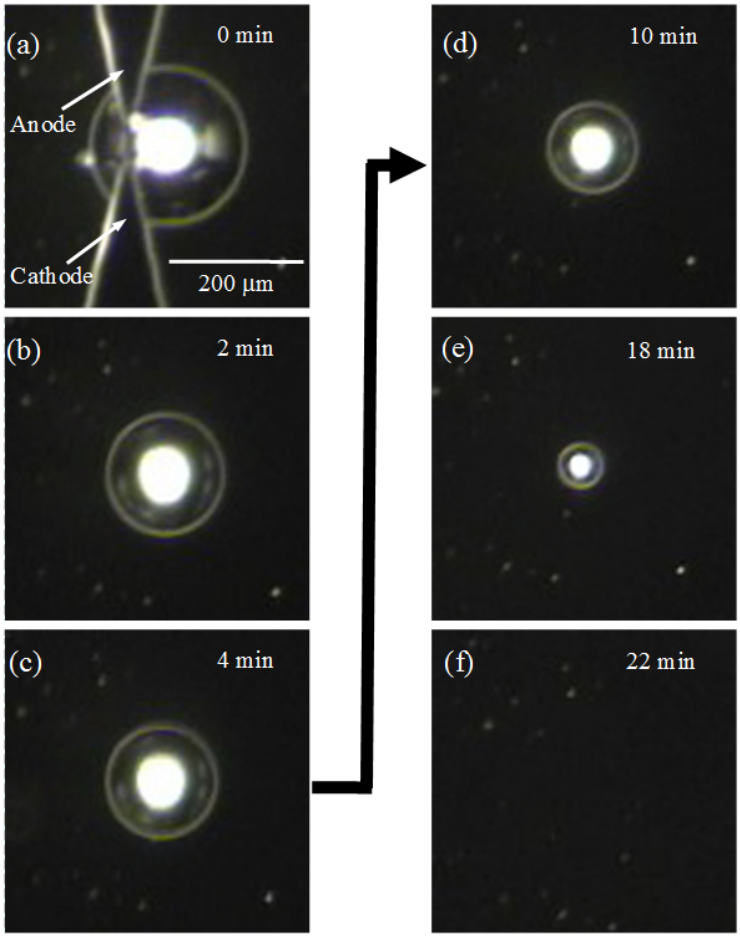

Figure 12 Sequential images of microbubble elimination. (a) A hydrogen-oxygen mixture bubble is created on the top plate and is transferred to the bottom plate on which a Teflon-covered (2000 Å thick) platinum electrode is placed for the catalytic bubble elimination process. (b) The bubble rapidly starts to shrink by the catalytic chemical reaction. (c-f) As time goes on, the shrinking speed decreases. The total time for complete elimination of a 200 μm diameter bubble is about 22 minutes.

To confirm this concept, the bubble shrinking process on a Teflon-covered platinum electrode is first investigated before combining the transportation and shrinking operations. For this purpose, microbubbles are generated and immediately deposited on the elimination electrode without EWOD bubble transportation. Figure 12 shows sequential images of a microbubble that is shrinking on a Teflon-covered (2000 Å thick) platinum electrode. The experiment is carried out in the two-plate configuration immersed in the same water chamber as previously used for bubble creation (Fig. 10). The elimination site on the bottom plate is placed at the same lateral and longitudinal position as the creation site on the top plate. The configuration of Electrode II on the top plate is used for bubble generation. When a voltage (6 V) is applied to the anode and cathode on the top plate, a hydrogen-oxygen mixture bubble is generated and grown. As soon as the bubble touches the bottom plate, it is automatically transferred from the top to the bottom plate due to the higher hydrophobicity of the bottom plate (Fig. 12a). The voltage is then turned off and the top plate is removed for better visualization of the bubble. Figure 12b shows that the transferred bubble suddenly starts to shrink. This is attributed to the catalytic reaction associated with gas transfer through the Teflon layer. As the bubble becomes smaller and smaller, this shrinking rate seems to gradually decrease. It takes the 200-μm diameter bubble about 22 minutes to be completely eliminated (Fig. 12c-f).

To find the effect of the Teflon layer thickness on the bubble shrinking speed, similar experiments are performed with three different thicknesses (400, 1200, and 2000 Å) for the Teflon layer, along with a bare platinum electrode. Figure 13 shows the volume of the shrinking bubbles vs. time for the different Teflon layer thicknesses. Here the same initial bubble volume (V_o = 0.6 nl) is used for all the cases. The data in Fig. 13 are represented using the dimensionless parameter of bubble volume (V) divided by the initial volume (V_o). For reference, the bubble

placed on a Teflon-covered silicon surface is also examined. In this case, there is no catalytic reaction at all, only a pure dissolving process into water. As expected, the total time for complete elimination is very long, about 250 minutes, an order of magnitude larger than any of the other cases (inset in Fig. 13a). Conversely, when the Teflon-covered platinum electrodes are used, the elimination time is substantially decreased; in all of these cases, the bubbles are completely eliminated in less than 20 minutes.

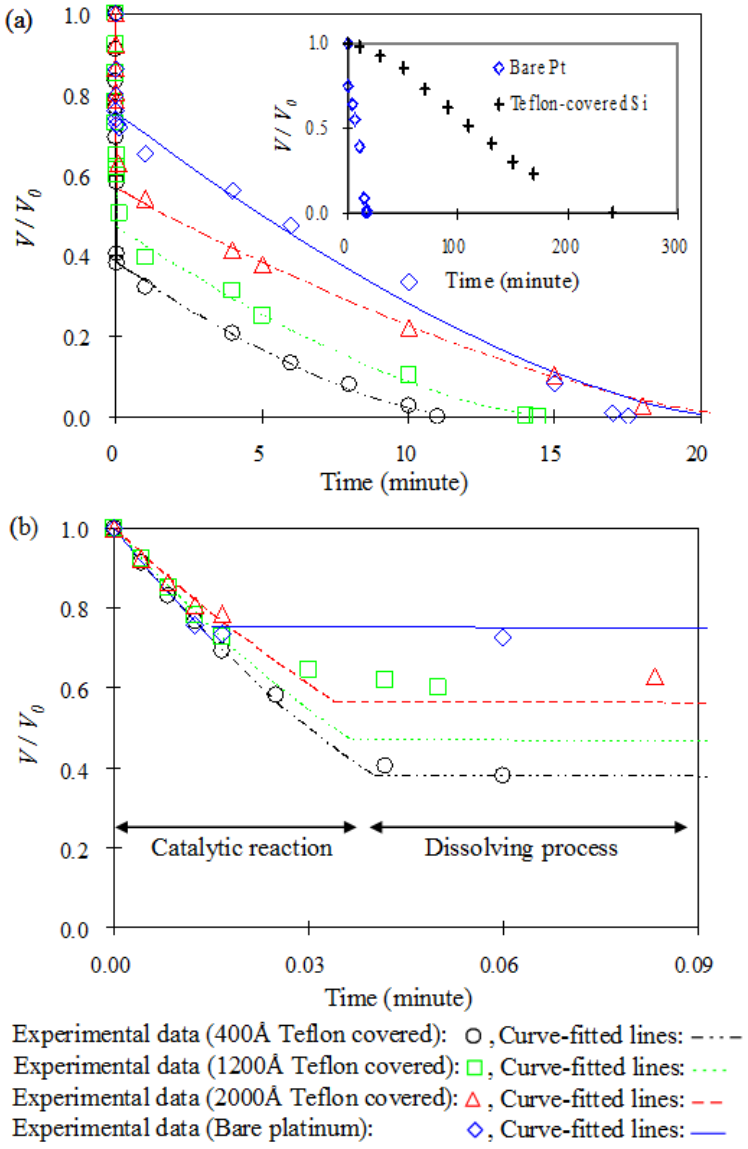

Figure 13 Effects of the Teflon layer thickness covering the platinum electrode on bubble shrinking. The volume (V) is normalized by the initial volume (V_o = 0.6 nl) which is the same for all the cases tested. For reference, a bubble on a Teflon-covered silicon surface is also examined. The platinum electrode accelerates bubble shrinking by an order of magnitude faster than the Teflon-covered silicon surface, as shown in the inset. The thinner the Teflon layer is, the faster the bubble shrinking is. Note that the bare platinum electrode is not more effective than the Teflon-covered platinum electrodes.

As the Teflon layer becomes thinner, the elimination time is reduced (Fig. 13a). The shortest time is about 11 minutes for the 400 Å Teflon layer. This confirms that the thinner Teflon layer allows higher rate of mass exchange through the layer. The overall bubble shrinking process consists of two distinct sequential steps: catalytic reaction and dissolving process, which is more clearly shown in Fig. 13b. In the beginning, the catalytic reaction makes rapid bubble shrinking. For the Teflon-covered electrode cases, more than 40% of the initial volume is eliminated by the catalytic reaction. Then, the shrinking speed significantly slows down as shown in Fig. 13a and b. The catalytic reaction is prominent only for a few seconds. This may be attributed to the fact that the contact area between the platinum and gas and the gas concentration in the bubbles decreases as the bubbles shrink. This mechanism can be modeled by approximating that the number of reacted gas molecules on the platinum surface is proportional to the average gas concentration c^* (moles/m^3) in the bubble and the contact area A. The reduced number of gas molecules in the bubble is equal to the reacted number of gas molecules on the platinum surface, yielding the following differential relation: $d(c^*V)/dt \sim -c^*A$. Equating this relation with the ideal gas law ($P \sim c^*$) and the Young-Laplace equation ($P \sim 1/V^{1/3}$) yields $d(V^{2/3})/dt \sim -V^{1/3}$. By integrating this equation, the approximate functional form can be written with the coefficient k as:

$$\left(\frac{V}{V_o}\right)^{1/3} = 1 - kt \tag{4}$$

As shown in Fig. 13b, the bubble volume V by the catalytic reaction is curve-fitted using Eq. (4).

After the catalytic reaction, the process is taken over by the slow dissolving process in which gas is directly dissolved through the gas-liquid interface. Based on the Epstein and Plesset equation, the approximated relation between the volume and time was given with coefficients a' and b' as,

$$\left(\frac{V}{V_o}\right)^{2/3} = a' + b't \tag{5}$$

The curve-fitted lines in Fig. 13a, which correspond to the nearly horizontal lines in Fig. 13b, are obtained using Eq. (5), describing the dissolving behavior well.

Very interestingly, the elimination time for the bare platinum electrode is similar to or longer than the other Teflon-covered platinum electrodes. This is due to the fact that the bubble has less contact area with the bare platinum electrode than the Teflon-covered electrodes. The contact angle (defined in the water side) of the bubble on the bare platinum electrode is measured at about 45^o while it is about 120^o on the Teflon-covered electrode. This means that the bubble is configured much flatter on the Teflon-covered electrode than on the bare platinum electrode. Recall that the initial volume of the bubble on the bare electrode is the same as in the other cases. From the above results, the Teflon-covered electrode provides two advantages over the bare platinum electrode: i) faster bubble elimination and ii) enablement of transportation of bubbles onto the elimination electrode.

To find the effects of the bubble size on the bubble shrinking speed, experiments are carried out with three different bubble sizes (200, 250 and 320 μm in top-view diameter). The experimental setup and conditions are the same as the ones in Fig. 13. Figure 14 shows the

change of the bubble volume with respect to time for the three different size bubbles. The two mechanisms (catalytic reaction and dissolving process) also appear. The sudden reduction at the beginning is attributed to the catalytic reaction. The smaller the bubbles are, the faster they shrink. In particular, for the 200 and 250 μm bubbles, the catalytic reaction seems to play a major role in the shrinking process. For the 320 μm case, however, it seems that the catalytic reaction is saturated quickly and is then followed by the much slower dissolving process. As a result, the entire process is largely dictated by the dissolving process. The total time is up to 350 minutes, much longer than the other two cases.

In the above cases, the testing bubbles contain a mixture of hydrogen and oxygen gases. Here, one may be questioning whether the catalytic reaction is effective on a single component gas bubble such as hydrogen or oxygen bubble. In this regard, oxygen and hydrogen bubbles are separately generated in water without adding NaCl. Electrode configuration I is used that has a distance of 5 mm between the anode and cathode. Under the application of 14 V between the anode and cathode, hydrogen and oxygen bubbles of 200-μm diameter are generated, the same size as the mixture bubble. As shown previously, the generated bubbles are immediately transferred onto a Teflon-covered (400 Å thick) platinum electrode. Figure 15 shows the shrinking speed of hydrogen, oxygen and their mixture bubbles. As expected, the mixture bubble shrinks faster than the other two bubbles.

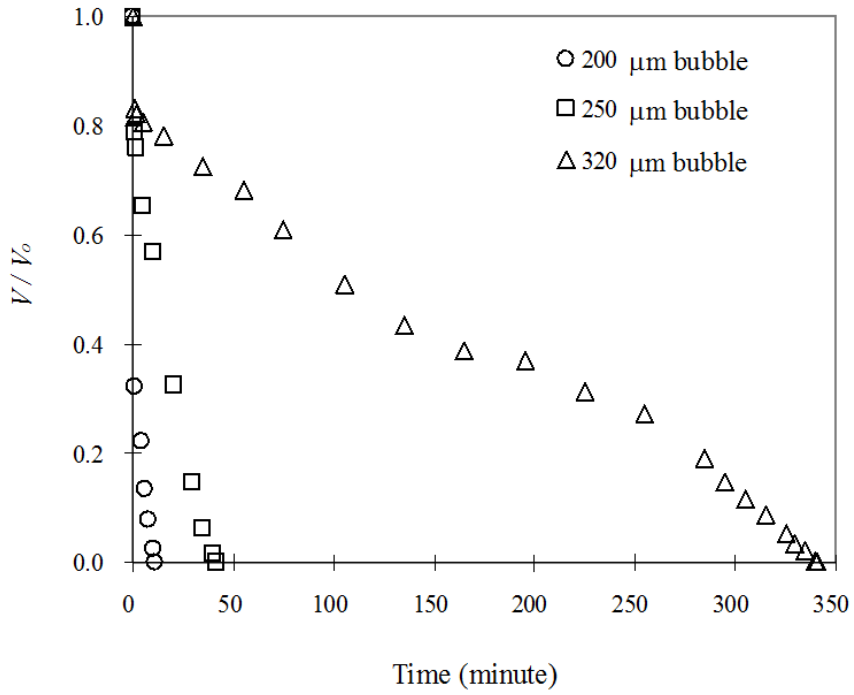

Figure 14 Effect of bubble size on the elimination time. The bubbles are tested on the Teflon-covered (400 Å) platinum electrode. The catalytic reaction plays a major role in bubble shrinking, showing a sudden change in volume at the beginning. In particular, for the 200 and 250 μm bubbles, the catalytic reaction is effective until they are completely eliminated. For the 320 μm bubble, the catalytic reaction seems to saturate quickly and is followed by a slow dissolving process.

It is noteworthy that the platinum catalytic reaction expedites the shrinking process of the hydrogen and oxygen as well. One may easily presume that mixing of the two gases is a necessary step prior to catalytic reaction because in most of the previous works the catalytic reaction for bubble shrinking has been applied to hydrogen/oxygen mixtures, not to single component gases. As shown in Fig. 15, however, elimination of oxygen and hydrogen bubbles can be expedited by the catalytic reaction. The hydrogen and oxygen bubbles are completely eliminated within 20 minutes. Note that their elimination time on a Teflon-covered silicon surface is more than 200 minutes. Oxygen reduction by catalytic reactions has been rarely

reported in microfluidic devices, although it has been implemented in some macroscale fuel cell devices [71].

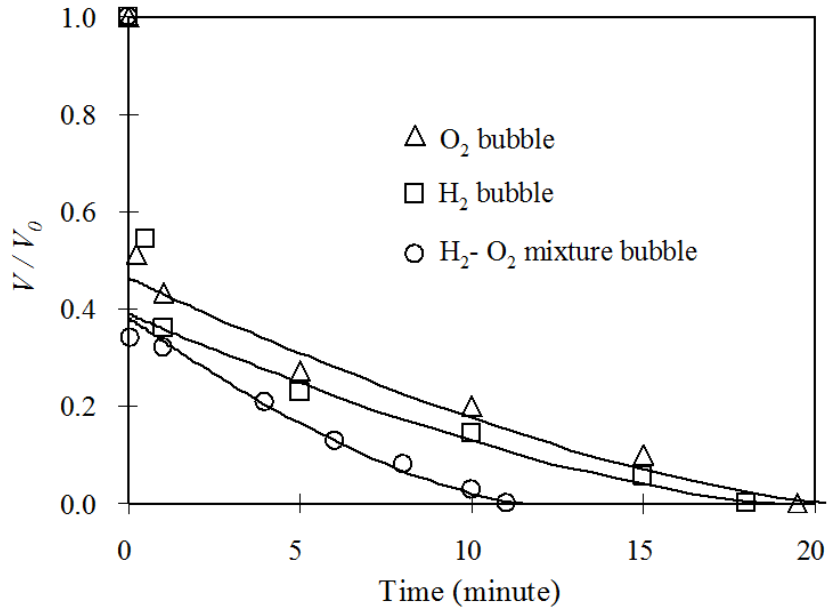

Figure 15 Effect of bubble gas type on the elimination speed. Before testing, oxygen, hydrogen and oxygen-hydrogen mixture bubbles are separately created and grown to the same diameter of 200 μm by electrolysis. Then, all three bubbles are tested on the Teflon-covered (400 Å thick) platinum electrode. The mixture bubble shrinks faster than the hydrogen and oxygen bubbles. However, it is noteworthy that the Teflon-covered Platinum electrode substantially accelerates elimination of the hydrogen and oxygen bubbles as well. On a Teflon-covered silicon electrode, elimination time for all the three bubbles is over 200 minutes.

Figure 16 demonstrates a series of integrated operations of generation, transportation and elimination. A hydrogen-oxygen mixture bubble (~ 250 μm in diameter) is created from the anode and cathode (electrode II), transferred to the bottom plate (Fig. 16b), and transported to the elimination site by shifting activations of EWOD electrodes (250 × 250 μm square) to the left (Fig. 16c & d). The Teflon layer (400 Å) on the elimination platinum electrode allows the bubble

to be easily transported and placed above the platinum electrode via EWOD. Finally, the bubble is completely eliminated in about 50 minutes by the catalytic reaction. Note that the upper bubble creation electrode peels off partially during the bubble creation process due to the low quality of the platinum layer (Fig. 16b).

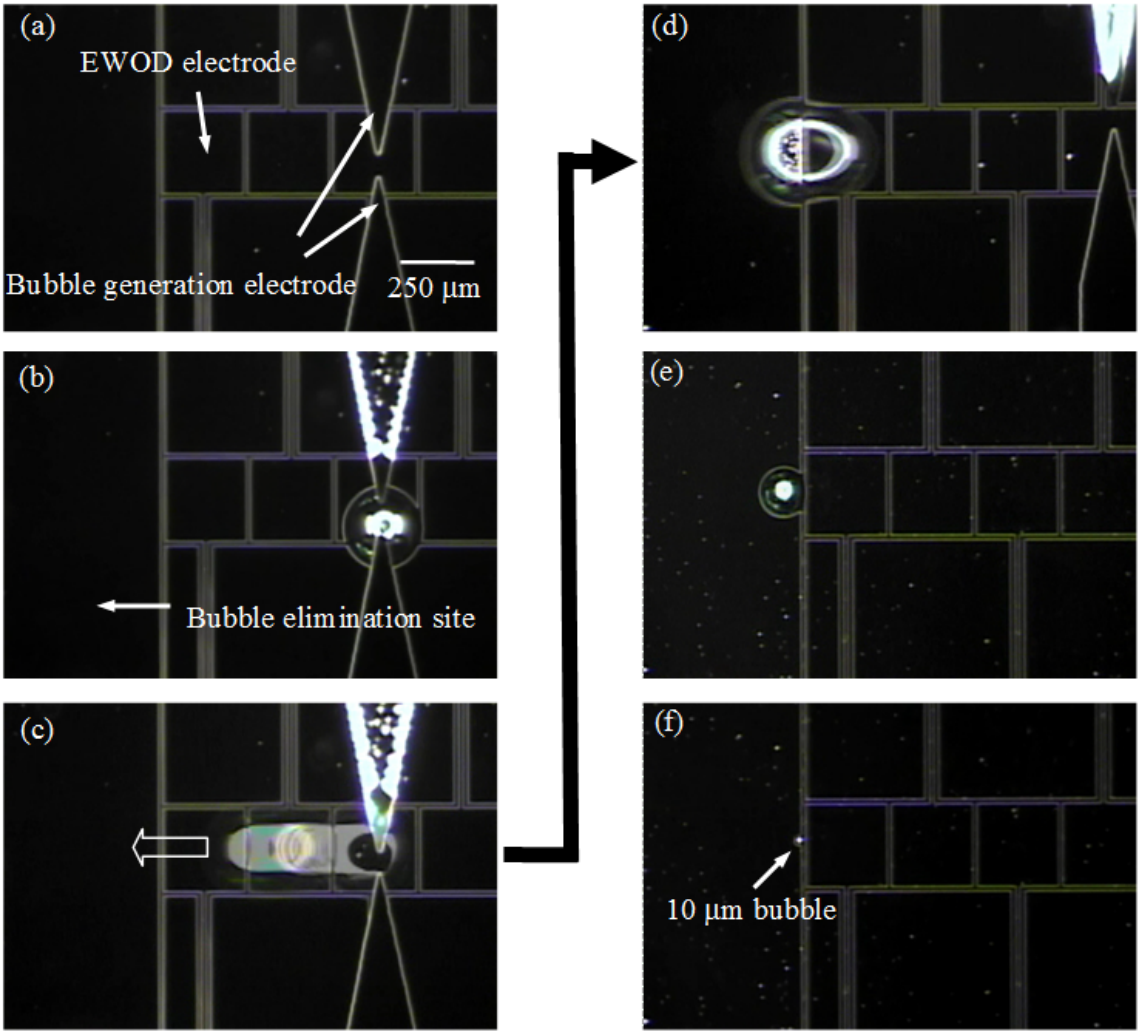

Figure 16 Sequential images of integrated microbubble operations: generation, transportation, and elimination. (a-b) Note that the elimination site is formed by covering the platinum electrode with a 400 Å Teflon layer. A hydrogen-oxygen mixture bubble (250 μm diameter) is generated by electrolysis from the top plate and transferred to the bottom plate. (c) The bubble is transported to the left by EWOD (d) and reaches the bubble elimination site. (e) The

bubble begins to shrink by the catalytic chemical reaction. (f) The bubble is shrunken down to 10 μm in diameter and is then completely removed in a few seconds.

2.4.3 Micro-object manipulation

Proof of the concept that EWOD-actuated bubbles can be used to push or pull micron- and millimeter-sized objects is demonstrated in Fig. 17. First, a millimeter-sized object is manipulated using bigger EWOD electrodes (1.4 × 1.4 mm^2). A fish egg (about 1 mm in diameter), with a hydrophilic surface, is pushed out of the well by an EWOD-actuated bubble (Fig. 17b) and then released from the bubble (Fig. 17c). Although not shown here, it is also confirmed that a hydrophobic object (sesame husk) can be similarly pushed and pulled by an EWOD-actuated bubble. Likewise, as shown in Fig. 17d-g, 80-μm glass particles are repositioned by a micron-sized bubble.

The microbubble of 250-μm in diameter is initially created from the cathode and anode (Fig. 17e) and is then transported to the right via EWOD (Fig. 17f), simultaneously pushing the surrounding particles. Finally, the bubble returns to the initial position. As a result, the particles are re-positioned. These results show the high feasibility of the direct bubble carrier concept.

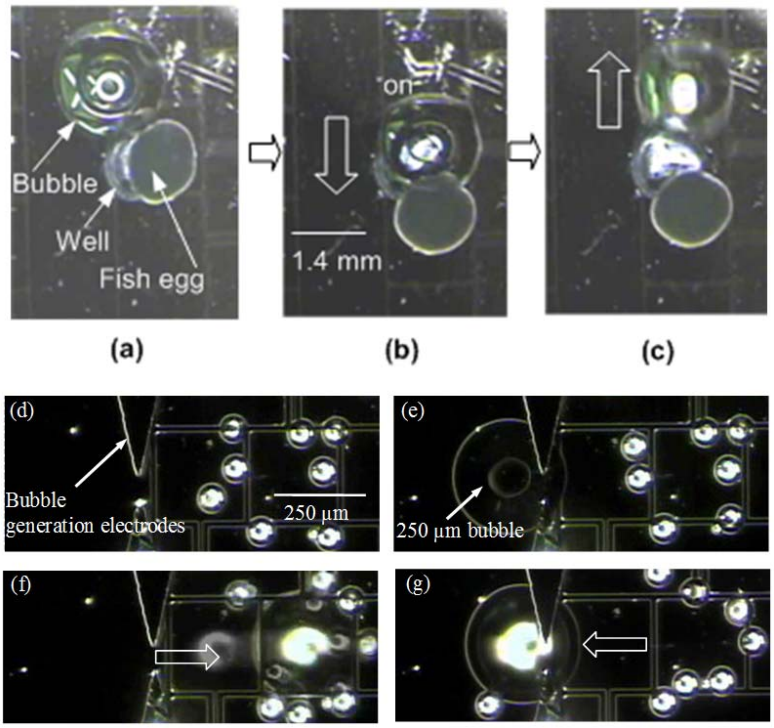

Figure 17 Bubbles can be used as carriers to manipulate millimeter- and micron-sized objects. (a-c) manipulation of millimeter-sized object: (b) an EWOD-actuated bubble pushes the fish egg out of the well and (c) releases it. (d-g) manipulation of micron-sized particles: (d) A 250 μm hydrogen-oxygen mixture bubble is generated by electrolysis from the top plate and is transferred to the bottom plate; (f) The bubble is transported to the right via EWOD, simultaneously pushing 80 μm glass particles; (g) The bubble returns back to the initial position, releasing the particles. As a result, the particles are re-positioned.

2.5 SUMMARY

This chapter describes on-chip creation and elimination of microbubbles using an electrochemical process and integration with EWOD (electrowetting on dielectrics) actuations. These operations constitute critical fluidic elements in the proposed microbubble-based micro-object manipulation platform. It is shown that microbubbles ranging from several microns to

several hundred microns in diameter can be electrolytically created. Hydrogen-oxygen mixture bubbles are “on-chip” created when the anode is placed next to the cathode (40 μm apart), whereas, when the anode and the cathode are separated by a distance of 5 mm, hydrogen and oxygen (or chlorine) bubbles are separately generated. By integrating bubble generation and EWOD actuation, created bubbles can be successfully detached and transported from the creation site.

By reversing the electrolytic bubble generation process, bubbles in water can be on-chip eliminated. The overall elimination process follows two sequential steps: catalytic reaction and dissolving process. In the catalytic reaction process, Pt electrodes are used as a catalyst either with or without a porous Teflon coating, substantially increasing the rate of elimination of microbubbles in both cases at an order of magnitude faster than on a Teflon-covered Si surface. However, the following dissolving process is relatively slow. As the Teflon layer becomes thinner, the bubbles shrink faster. Very interestingly, the Teflon-covered electrodes tested provide shorter elimination time than the bare Pt electrode. This is due to the fact that the bubble contact area on the Teflon-covered electrodes (hydrophobic surface) is larger than on the bare Pt electrode (hydrophilic surface). In addition, this Teflon layer is necessarily required to make the elimination electrode surface hydrophobic, thus making possible EWOD transportation of bubbles onto the elimination electrode.

As the initial bubble size decreases, the catalytic elimination becomes more prominent. The catalytic reaction is effective in eliminating hydrogen and oxygen bubbles as well as their mixture bubbles. Integrated bubble operations - generation, transportation and elimination - are realized on a single chip by electrolysis and EWOD, demonstrating a simplified scenario of bubble use in the micro-object manipulator. Finally, as a proof of concept for the bubble-based

direct object manipulator, it is demonstrated that an EWOD-actuated bubble can push micron- and millimeter-sized objects and release them at a different place.

3.0 2-D OBJECT MANIPULATION: CAPTURING, CARRYING, AND RELEASING

In Chapter 2, the fundamental microbubble operations - creation, transportation, and elimination - have been successively achieved along with their characterizations, underlying physics and modelling. In addition, as a primitive level of manipulation, direct push and pull of objects using EWOD actuated bubbles are demonstrated. In this chapter, acoustic excitation is integrated with the fundamental microfluidic structure and operations developed in Chapter 2.

3.1 THEORETICAL BACKGROUND

3.1.1 Cavitational microstreaming flow

When a gaseous bubble is exposed to acoustic wave, it oscillates (expands and shrinks) in harmony with the applied wave frequency since the bubble is compressible. Acoustic excitation generates various oscillation modes in bubbles such as axisymmetric, translational, and surface-wave oscillations, which are highly dependent on the excitation frequency and amplitude. Such oscillations can induce non-zero velocities in the time-averaged flow field in the surrounding fluid, so-called “cavitational microstreaming”, as shown in Fig. 18. A variety of vortical flow patterns around the oscillating bubble can be induced by changing the frequency and amplitude of the excitation. In general, the flow pattern has a toroidal vortex over the bubble with straight

flow near the bubble apex. Tho *et al* [47] visualized flow patterns and measured the velocity field around oscillating bubbles using polystyrene seed particles of 2 μm in diameter. Marmottant *et al* [46] derived a streaming function of a cavitational streaming flow for an axisymmetric bubble oscillation mode as follows:

$$\psi = -3\varepsilon^2 a^3 \omega \sin(\Delta\phi)\frac{a}{r}\cos^2\theta\sin^2\theta + O(\varepsilon^2 r^{-2}). \quad (1)$$

Here, ε is the amplitude of bubble oscillation normalized by the radius of the bubble a, ω is the angular frequency of the applied acoustic wave, r is the distance from the bubble center, θ is the angle coordinate with respect to the axis of translation, and $\Delta\phi$ is the phase shift between volume and translational oscillations. Note that the bubble on the solid surface experiences both up-and-down translational oscillation and radial volume oscillation. Marmottant *et al* [46, 72] confirmed a qualitative agreement between Eq. (1) and experimentally visualized flow pattern shown in Fig. 18. They showed that the induced vortical flow is highly sheared enough to deform and break neighboring vesicles (30 μm diameter). In addition, they showed that the vortical flow is controllable to some extent. Neighboring micro-particles were steered by putting a solid structure near the bubble [73].

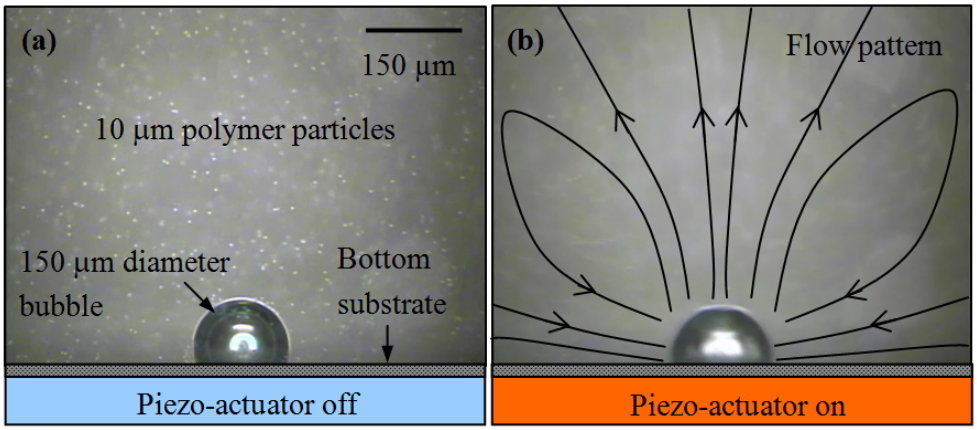

Figure 18 Cavitational microstreaming flow around an oscillating bubble. The bubble is excited by the piezo-actuator at 25 kHz. (a) Initial state : for flow visualization 10 μm polymer particles are seeded and suspended. (b) Excitation : large circulation flow patterns are formed around the bubble.

3.1.2 Radiation force

In addition to the microstreaming flow, the bubble oscillation generates a spherical pressure field as a secondary effect, so called acoustic radiation force (Bjerknes force). This pressure field is different from the primary sound pressure field that is generated by the external piezo-actuator. For a simplified axisymmetric bubble oscillation mode, Coakley and Nyborg [74, 75] derived the radiation force F_r acting on a spherical particle placed near the oscillating bubble, as follows:

$$F_r = \frac{4}{3}\pi R_s^{\,3}\left(B\frac{\partial K}{\partial r} - A\frac{\partial P}{\partial r}\right), \tag{2}$$

where A and B are given by

$$A = 1 - C_s / C_m \tag{3}$$

and

$$B = 3(d_s - d_m)/(2d_s + d_m)\,. \tag{4}$$

Here, d is the density, C is the compressibility, K is the kinetic energy density in the spherical wave, P is the potential energy in the spherical pressure wave, and subscripts m and s denote the fluid medium and the particle, respectively. For the spherical oscillation source of radius R_p and the radial velocity amplitude u_o of the bubble surface, K and P are given at radius r as:

$$K = 0.25 d_m {u_o}^2 {R_p}^4 \left[r^{-4} + k^2 r^{-2} \right] \tag{5}$$

and

$$P = 0.25 d_m {u_o}^2 {R_p}^4 k^2 r^{-2} \quad , \tag{6}$$

where k is the wavenumber (2π divided by the wavelength). Substitution of equations (5, 6) into equation (2) yields

$$F_r = \frac{4}{3} \pi {R_s}^3 d_m {u_o}^2 {R_p}^4 \left[(A - B)\left(\tfrac{1}{2} k^2 r^{-3}\right) - B r^{-5} \right] \tag{7}$$

In current experimental conditions, the order of *kr* is 0.01 or less. So the first term in the bracket is much smaller than the second term. If the first term in the bracket is ignored, then the radiation force reduces to

$$F_r = \frac{4}{3}\pi R_s^{\ 3} d_m u_o^{\ 2} B R_p^{\ 4} r^{-5} \tag{8}$$

The radiation pressure force is in proportion to the particle volume and the negative fifth power of the radius *r*. More importantly, the direction of the radiation force is dependent on the sign of *B*. This means that a particle would be attracted to the oscillating bubble when the density of particle is higher than the density of the medium, and vice versa. In this study, this attraction force will be harnessed to capture neighboring objects.

3.1.3 Capturing phenomena

3.1.3.1 Capturing phenomena by oscillating solid objects

Similar capturing methods using oscillation of solid bodies or fluids have been previously reported by other research groups. Lutz *et al* [76] showed that when a solid cylinder (radius *R*) is placed in a 2-D translational oscillating flow at the low frequency (< 1 kHz), four vortical eddies develop around the cylinder, one in each quadrant. Particles are trapped and collected into each center of the vortical eddies. Although the origin of the capturing force was not noted, the main features of trapping were well described through scaling analysis for the oscillating and steady

streaming flows. The trapping is pronounced when the object size is comparable to the Stokes layer thickness $\delta = (\nu/\omega)^{1/2}$, a characteristic measure of how far viscous damping of the oscillating velocity gradient persists from the oscillating body. Here, ν is the kinematic viscosity of the medium, and ω (= $2\pi f$) is the angular frequency of the applied oscillation. For a small oscillation ($\varepsilon << 1$), they showed that the dimensionless frequency $M = (R/\delta)^2$ alone controls the size of vortical eddies, and at a given frequency, ε controls the magnitude of the steady flow inside the eddies. By adjusting the eddy size similar to the size of trapping objects, they were able to capture spheres in the range of 10 to 36 μm (i.e., the sphere size is comparable to the Stokes layer, its ratio ranging from 0.4 to 1.5).

In the mean time, Hu and Santoso [77] developed an ultrasonic tweezers in which a multilayer piezoelectric vibrator (oscillating solid body) was clamped between two metal plates and immersed in water. The flexural vibration of the metal plates was used to generate a standing wave sound field in the gap between the plates. Particles congregated at nodes (zero sound pressure) in the sound pressure field between the plates depending on the compressibility and density of the particles and medium. The excitation frequency was 152.8 kHz, between one and two orders of magnitude higher than the present applied frequencies. Recently, Hu *et al* [78, 79] extended the work using a single needle strongly vibrated by a stacked piezo-actuator. They suggested that attracting and capturing of particles by the single needle were also attributed to the pressure node (zero pressure) near the vibrating needle (acoustic radiation force or Bjerknes force). Note in the above studies that the solid needles vibrating in large amplitudes, not oscillating bubbles, are used to attract the objects. In addition, the force direction depending on the density difference between the fluid and particle was not reported.

3.1.3.2 Capturing phenomena by oscillating bubbles

When a bubble oscillates in the presence of an acoustic field, the induced cavitational microstreaming flow agitates the surrounding fluid. Thus, neighboring particles orbit in the vortical streaming flow rather than being attracted and captured on the bubble surface. That is, it gives an adverse effect in capturing objects. Meantime, as predicted by Coakley and Nyborg [74], the acoustic radiation force (or Bjerknes force) for axisymmetric oscillations is responsible for attracting particles. The oscillating bubble emits spherical acoustic waves and generates nodes and antinodes in the sound pressure field around the bubble. In this case, neighboring particles can be attracted and collected in the node areas. Miller [80] reported that the particle attraction behavior appears when gas traps in microspores are ultrasonically excited.

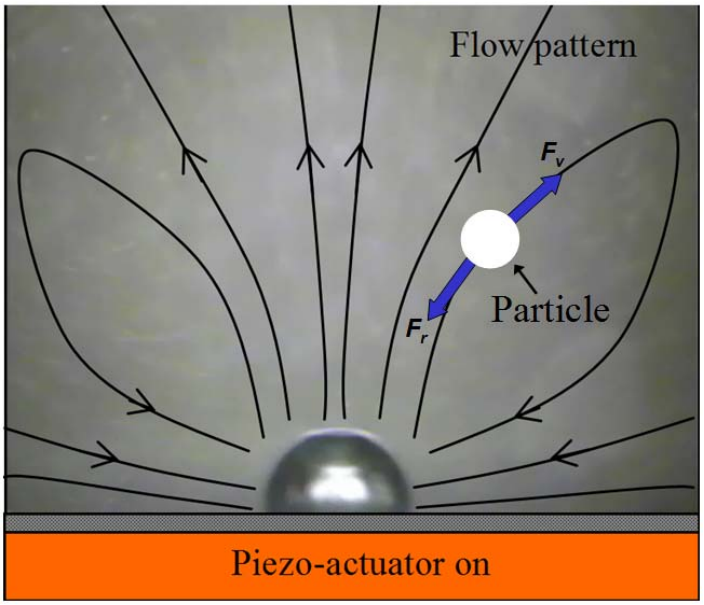

Figure 19 Schematic image of a particle in a cavitational microstreaming flow generated by an oscillating bubble. The particle experiences the acoustic radiation force (F_r) and the Stokes drag force (F_v) simultaneously.

As a result, the capturing mechanism is the competition between the acoustic radiation force and microstreaming flow in Fig. 19. In particular, the object is placed on outgoing

streamlines. In this condition, forces acting on the particle are the radiation force F_r and the Stokes drag F_v, as illustrated in Fig. 19. The Stokes drag on the particle is given as:

$$F_v = 6\pi\eta R_s U_s \,, \tag{9}$$

where η is the medium viscosity, R_s is the particle radius, and U_s is the velocity of the particle relative to the medium. For the acoustic streaming flow generated by a hemispherical oscillating bubble resting on a solid boundary, the maximum limiting particle velocity in streaming flow U_s is specified as follows [81]

$$U_s = +\omega^{-1} u_o^{\,2} R_p^{\,4} r^{-5} \tag{10}$$

where $\omega = kc$. The positive sign indicates that this flow is directed radially outward from the hemisphere bubble surface. The substitution of equation (10) into equation (9) yields:

$$F_v = 6\pi\eta\omega^{-1} u_o^{\,2} R_s R_p^{\,4} r^{-5} \quad . \tag{11}$$

The ratio of the radiation force [equation (8)] to the maximum drag force [equation (11)] on the particle particle is given as:

$$[RF]/[AS] = \tfrac{4}{9}\pi f d_m B R_s^{\,2} \eta^{-1} \,. \tag{12}$$

Here, [*RF*] and [*AS*] represent the relative magnitudes of the radiation force and the drag force, respectively. Equation (12) reveals that when the particle becomes larger and the particle density is larger than the medium density the radiation force dominates the drag force. As a result, the capturing will be effective for large and dense particles. The above relation is derived with many assumptions and simplified first-order modeling (i.e., axisymmetric oscillations). Therefore it may not be suitable to quantitatively compare it with real experimental results. However, the relation provides quantitative guidelines to optimize the capturing conditions. In the following result sections, the qualitative trend for this relation will be experimentally verified.

3.2 TESTING DEVICE FABRICATIONS

In order to investigate and characterize the capturing phenomenon, acoustic excitation without EWOD is first applied to air bubbles on a Teflon-covered glass plate ($2 \times 2 \times 0.05$ cm^3). Since oscillating bubbles are easily detached from the hydrophilic glass plate due to the buoyancy force, the top surface of the plate is spin-coated with a hydrophobic amorphous Teflon layer. Spin coating of 2 % Teflon solution (Teflon AF 1600® + Fluorocarbon solvent) results in a 2000 Å thick Teflon layer. Two configurations are examined for bubble excitation. The first is that a large droplet is placed on the glass plate. After injecting a small bubble in the droplet using a pipette, a top glass cover is gently placed against spacers on the bottom glass plate. Although not used here, the on-chip bubble generation method via electrolysis can be easily integrated with the present system. For the spacers, double-sided tape of approximately 100 μm thickness is used. In addition to maintaining the gap between the bottom glass plate and top glass cover, these spacers serve as sidewalls to confine the water. The gap between the top and bottom plates is fixed at

approximately 500 μm by stacking 5 layers of the tape. A ring type piezo-actuator (outer and inner diameters, and thickness are 25 mm, 9.5 mm, and 3.2 mm, respectively, Omega Piezo Co.) is directly glued onto the back of the glass plate.

The second configuration is with the bottom glass plate immersed in a water chamber (5 × 5 × 2.5 cm^3 with 1.5 cm water level) and placed on the bottom of the chamber. The same piezo-actuator is glued to the bottom of the chamber, rather than to the glass plate. Air bubbles are injected directly on the hydrophobic top surface of the glass plate using a pipette. After preliminary tests, we find that capturing behaviors are qualitatively very similar in the two configurations. One main difference is that the bubble oscillation amplitude becomes somewhat lower when the glass plate is immersed in the chamber. The applied signal for acoustic excitation is generated by a function generator, amplified by a power amplifier, and transmitted to the piezo-actuator. To view bubble motions, the testing chip is placed under a microscope (EO Edmund optics co.) which is connected to either a regular CCD camera (CV-S3200, JAI Co.) or a high-speed camera (Phantom v7.3, Vision Research Co.).

For integration of acoustic excitation with EWOD, a linear array of individually addressable electrodes needs to be incorporated into the aforementioned Teflon-covered plate. As illustrated in Fig. 16, the testing setup is a two-plate channel structure: top and bottom plates with the bubble in between. The main fabrication process for electrodes on the bottom plate consists of three steps: metallization and patterning of electrodes, deposition and patterning of the dielectric layer, and deposition of the hydrophobic layer. For the EWOD driving electrodes, a chromium layer of 100 Å in thickness as an adhesion layer and a gold layer of 2000 Å in thickness are sequentially deposited on a glass wafer by sputtering and are then patterned by wet etching. Each driving electrode is a square with an area of 250 × 250 μm^2 or 1.0 × 1.0 mm^2. A 3-

μm thick photoresist (AZ4210, Clariant Corporation) layer is then spin-coated on as the dielectric layer. Finally, the bottom plate is spin-coated with a hydrophobic Teflon layer.

The top glass plate, coated with a transparent, conductive ITO (Indium Tin Oxide) layer, serves as ground for the EWOD actuation. The transparent ITO layer covering the entire area of the top glass plate allows bubble motions to be seen. The last step of the fabrication process is to integrate the two plates. After putting a large water droplet on the bottom plate, a bubble is injected on the bottom plate using a pipette. The top glass plate is gently pressed against the spacers on the bottom plate. The gap between the top and bottom plates is also fixed at approximately 500 μm. For more details on the EWOD chip fabrication, refer to Fig. 6.

3.3 RESULTS AND DISCUSSION

3.3.1 Radiation force vs. Streaming Flow in Capturing

To confirm the competition between the acoustic radiation (Bjerknes) force and streaming flow in the particle capturing, various experiments are carried out. Firstly, the effect of particle size in capturing phenomena is experimentally checked. According to Equation (12), larger particles should have stronger radiation force than smaller particles. It is expected that large particles are attracted to the oscillating bubble while small particles follow the vortical flow pattern or are scattered away.

The excitation frequency is set near the natural frequency of the bubble. The natural frequency f_o for air bubbles can be roughly estimated using Minnaert's equation [82]: $af_o \cong 6$ kHz•mm [83], although this relation is developed for a suspended spherical bubble in medium,

not bubbles hanging from a surface. For a higher accuracy, the natural frequency of bubbles on a solid surface can be experimentally determined at the frequency for which the oscillation amplitude of the bubble reaches a maximum value. For this process, regular- and/or high-speed images are used.

A mixture of two different sized glass particles is tested with two different sized bubbles in a water chamber (the second configuration described in section 3.3). As shown in Fig. 20 a-2 and b-2, 80 μm glass particles are collected to the bubble rim whereas 8 μm particles are scattered away from the oscillating bubbles and drifting into the surrounding vortical streamlines after applying acoustic excitation on the bubbles for seconds. Note that particles of the two different sizes are initially mixed and deposited on the surface.

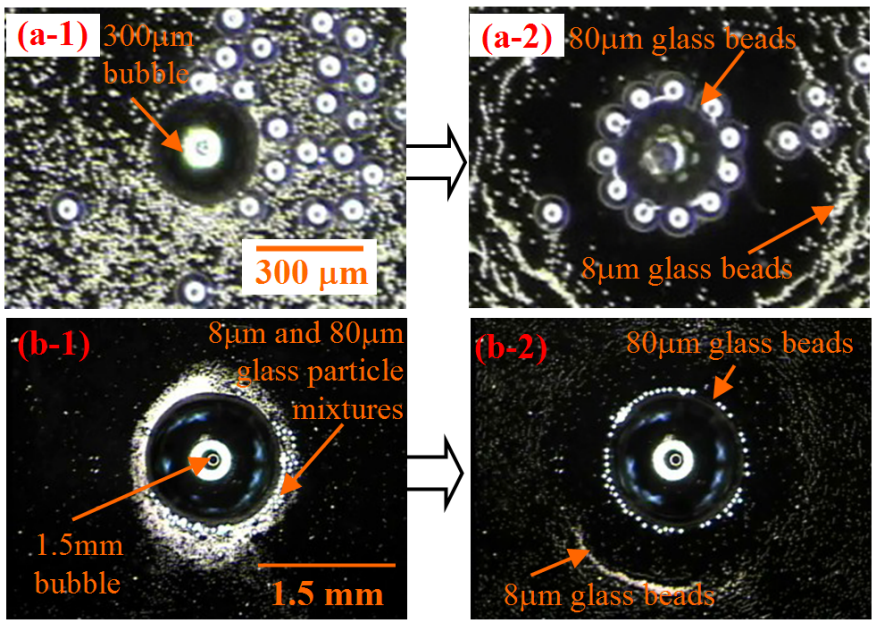

Figure 20 Sequential pictures showing that acoustically excited oscillating bubbles can separate particles of two different sizes. (a) with a 300 μm bubble and mixtures of 8 μm and 80 μm glass particles: (a-1) initial state; (a-2) After acoustic excitation (20 kHz), most of the 80 μm particles are collected near the bubble whereas the 8 μm particles are repelled away; (b) with a 1.5 mm bubble and mixtures of 8 μm and 80 μm glass particles: (b-1) initial

state; (b-2) After acoustic excitation (4.5 kHz), the 80 μm particles are collected around the bubble whereas the 8 μm particles are repelled away.

It is important to find the effect of the particle size on the capturing performance. Using the same experiment setup as the one in Fig. 20, four different sized glass particles (2 μm, 8 μm, 20 μm, 40 μm) are tested to find the critical particle size for capturing as shown in Fig. 21.

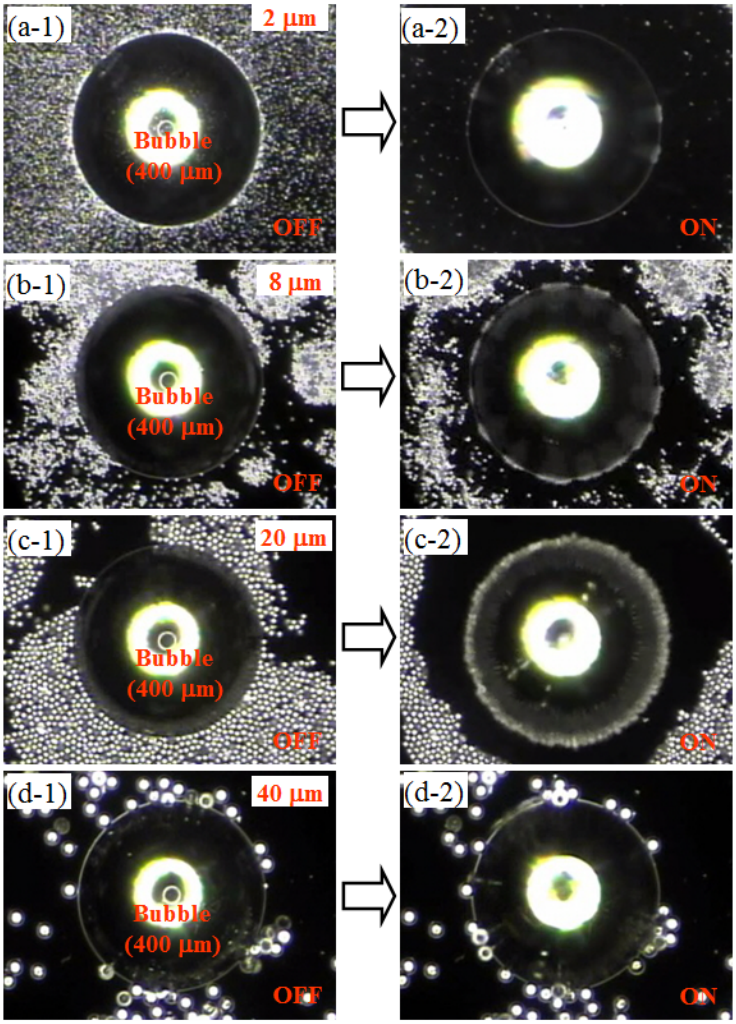

Figure 21 Sequential pictures showing particle capturing or repelling, depending on the particle size. (a) a 400 μm bubble and 2 μm glass particles: (a-1) Initial state; (a-2) After acoustic excitation (15 kHz), most particles are repelled away from the bubble; (b) a 400 μm bubble and 8 μm glass particles: (b-1) initial state; (b-2) After acoustic

excitation (15 kHz), a small amount of particles is collected around the bubble whereas most particles are repelled away. (c) a 400 μm bubble and 20 μm glass particles: (c-1) Initial state; (c-2) After acoustic excitation (15 kHz), some of the particles are collected around the bubble whereas the rest of the particles are repelled away; (d) a 400 μm bubble and 40 μm glass particles: (d-1) Initial state; (d-2) After acoustic excitation (15 kHz), most particles are collected around the bubble.

The results show that the oscillating bubble (400 μm diameter) consistently captures particles larger than 40 μm in diameter, but repels particles smaller than 2 μm in diameter. The capturing behavior of the glass particles between 2 μm diameter and 40 μm in diameter is not clear. They are captured or repelled by the oscillating bubble. Overall, larger particles in the range are more likely to be captured.

In addition, the density difference between the particle and medium is evaluated using low density particles. Miller [80] examined the density difference effect using polystyrene particles (diameter 1 μm and density 1.05 kg/L) in a water-based medium. The medium density was elevated to see repelling of the particles but he could not observe clear repulsion. Perhaps, the density difference was not high enough for the repulsion force to appear. As a consequence, he could not prove the simplified theory (equation (8)) from his experiment completely. Since then, it has not been very clear that the Bjerknes force is really responsible for the capturing phenomenon. To check the existence of the repulsion force, a similar experiment that Miller did is conducted in the water chamber. A Teflon-coated transparent glass substrate is immersed in water and suspended horizontally. For the low-density particle, hollowed glass particles (K1, 3M^{TM}, density 0.125 kg/L) are used. Note that the density difference between the particle and the liquid medium is much smaller than Miller's case. A bubble (500 μm diameter) and the hollow glass particles are injected on the bottom side of the plate by using a micropipette. Due to the

low density, the particles and bubble stay on the bottom surface of the plate. The particle size is diverse in the range of 10 to 100 μm in diameter. When the piezo-actuator attached beneath the water chamber excites the bubble, all the hollow glass particles are repelled from the bubble, Fig. 22b, c. This finally proves that equation (8) correctly describes the capturing phenomenon, at least in a qualitative manner. That is, the radiation force is responsible for attracting neighboring objects.

In the meantime, polystyrene particles (density 1.05 kg/L) are also examined in heavy water (D_2O with density 1.106 kg/L). The result shows that the particles are not repelled but attracted on the bubble as similar to Miller's results. It maybe the density difference is not large enough to see the particle repelling.

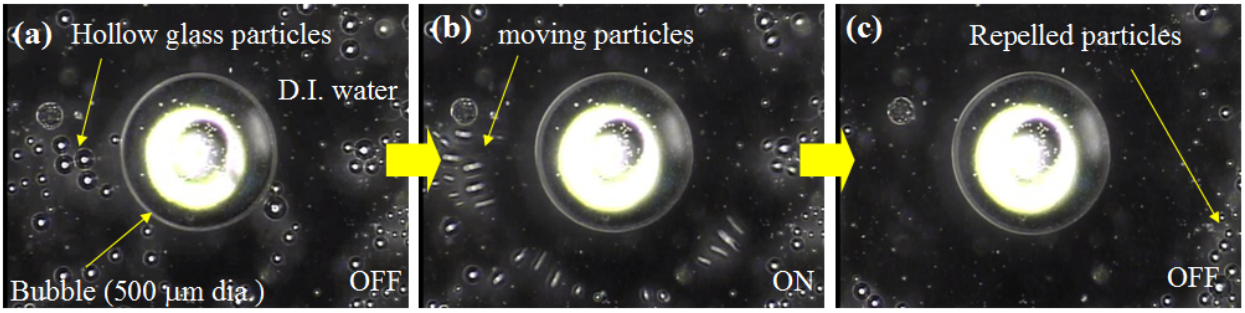

Figure 22 Sequential images of a repelling test using hollow glass particles: (a) Initial state. (b-c) When a bubble (500 μm diameter) is acoustically excited at 10 kHz, all particles, having different sizes, are repelled from the oscillating bubble.

3.3.2 Capturing of various objects

Shown in Fig. 23 is the capturing of various objects such as spherical glass particles, a fish egg, and a water flea. Bubble sizes ranging from 400 μm to 1.5 mm are examined in the water chamber configuration. First, glass beads of 80 μm in diameter are tested with a micron sized bubble of diameter a = 400 μm (Fig. 23a). Initially, more than 60 glass beads are placed around the bubble rim.

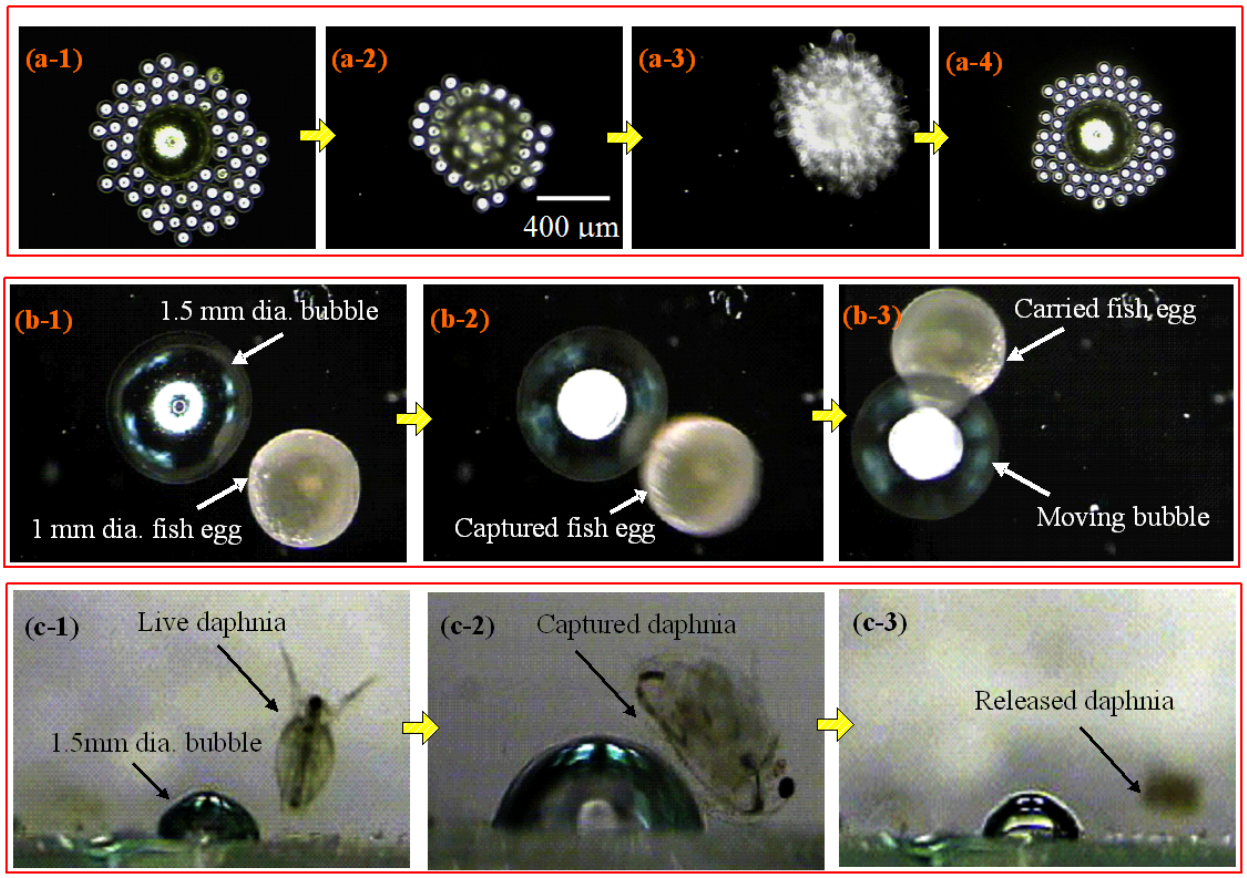

Figure 23 Capturing of various objects using oscillating bubbles: (a-1) Initial state, (a-2) More than 60 glass particles (80 μm dia) are captured in orbit by the oscillating bubble when the piezo-actuator is turned on (200 V), (a-3) The oscillating bubble, at its natural frequency of 15 kHz, erratically and randomly moves on the surface carrying the captured particles, (a-4) Turning off acoustic excitation releases the captured particles; (b-1) Initial state, (b-2) A

fish egg (~1 mm in diameter) is attracted to the oscillating bubble which is acoustically excited at 4.5 kHz, (b-3) The captured fish egg is carried by the oscillating bubble in erratic motion on the surface; (c-1 and -2) A live water flea (Daphnia) is captured by an oscillating bubble acoustically excited at 4.5 kHz, (c-3) The water flea can escape only when the bubble oscillation is turned off. Note that the applied voltage to the piezo-actuator in (b) and (c) is 400 V.

As the frequency approaches the natural frequency of the bubble, oscillation amplitude grows and almost all particles are collected, as shown in Fig. 23a-2. Some collected particles are orbiting around the bubble. Interestingly, when the applied frequency is set at the natural frequency (15 kHz), the oscillating bubble moves erratically and violently on the surface, yet it holds the particles (Fig. 23a-3). The bubble oscillation is strong enough to overcome contact angle hysteresis in the bubble and therefore generates lateral motions. Note that no EWOD actuation is applied in this case. When the excitation is off, the lateral bubble motion is stopped, and all the captured particles are released from the bubble (Fig. 23a-4). Even after large displacement motions in the bubble, the number of particles around the bubble remains almost the same as before excitation. These results enable us to employ bubbles as particle carriers.

Oscillating bubbles can capture larger objects with sizes comparable to the bubble size. Figure 23b shows that an oscillating bubble of a = 1.5 mm can capture a fish egg (about 1.0 mm in diameter). When the excitation frequency is set at the natural frequency of the bubble (about 4.5 kHz), the oscillating bubble captures (Fig. 23b-2) and carries the fish egg while the bubble is randomly moving around on the surface (Fig. 23b-3). When the acoustic excitation is turned off, the bubble releases the fish egg. In addition, an oscillating bubble can capture and hold a live animal. Figure 23c shows sequential images of capturing and holding a water flea (*Daphnia*) using an oscillating bubble of a = 1.5 mm. The water flea is almost the same size as the bubble.

When the water flea comes close to the bubble, the piezo-actuator is turned on. The water flea is captured by the bubble, and cannot escape from the bubble (Fig. 23c-1 and -2). The water flea makes several strokes to swim away from the bubble but is attracted back to the bubble. Only when the actuator is turned off is the water flea able to swim away from the bubble (Fig. 23c-3). Note that the water flea is still alive even after the capturing process. The drag force F_d on the free-swimming water flea is estimated at ~ 50 nN based on Stokes drag ($F_d = 6\pi\mu Dv$), where μ, D, and v are the water dynamic viscosity (10^{-3} Pa•s), water flee diameter (~ 0.5 mm), and water flee swimming speed (~ 1 cm/s [84]), respectively. It can be reasonably assumed that the capturing force is comparable in magnitude to the drag force.

To measure how far the capturing force reaches, glass particles are initially placed in a row beginning from the bubble rim and extending in the radial direction, as shown in Figs. 24a-2 and 24b-2. Two different bubbles of a = 300 μm and a = 1.5 mm are examined on the Teflon-covered plate immersed in the water chamber. Acoustic excitation is set at the natural frequencies for each bubble (19 kHz and 4.3 kHz, respectively) and the maximum applied voltage is 300 V and 700 V, respectively. Since at the natural frequencies the bubbles randomly move due to violent oscillations, the bubbles must be held to the surface. To accomplish this, the Teflon layer is patterned with two circles of 300 μm and 1.5 mm in diameter. It is found that the bubbles remain on the Teflon circle patterns throughout experiments even when they are strongly excited at the natural frequencies. Experiments for the two different size bubbles (a = 300 μm and 1.5 mm) are carried out separately. When the bubble of a = 300 μm is excited at its natural frequency of 19 kHz, the bubble is oscillating with surface undulations on the bubble surface showing a polygonal shape, not a perfect spherical cap, as shown in the high-speed image in Fig. 24a-1. Using the high-speed camera, the peak-to-peak oscillation amplitude Δ at the bubble apex

is measured at about 15 μm ($\varepsilon = \Delta/a$ = 5%). As shown in Fig. 24a-3, all the particles within ~ 2a from the bubble center are captured upon excitation. In this range, the microstreaming vortical flow is strong enough to overwhelm the adhesion (friction) force between the particles and the solid surface.

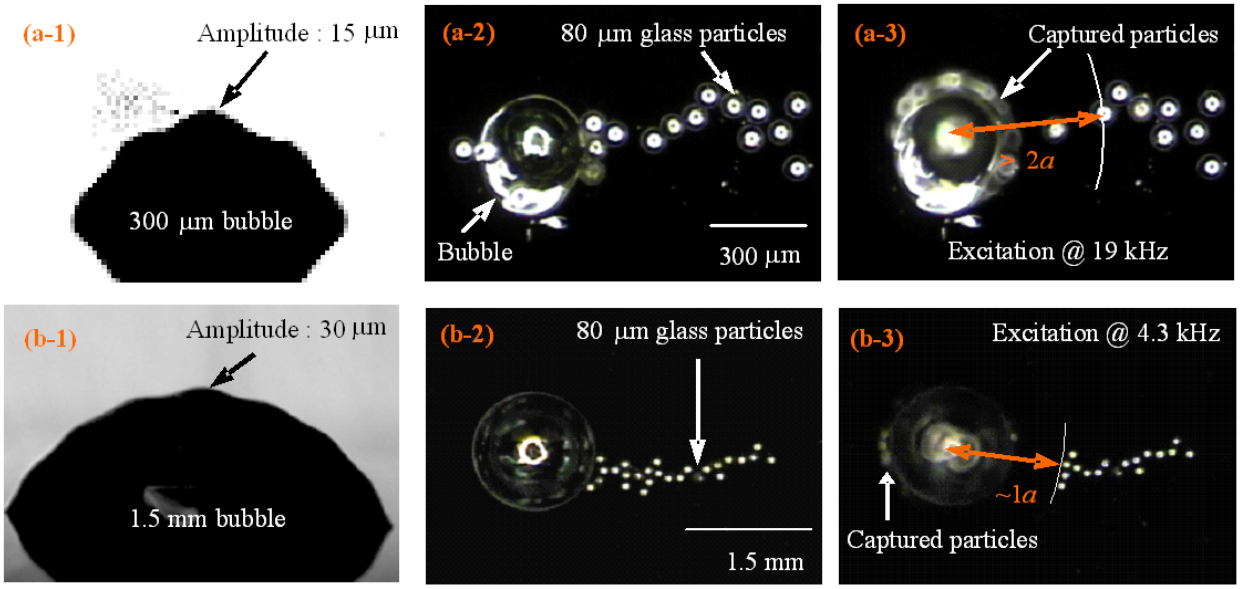

Figure 24 Oscillating amplitude of bubbles and corresponding capturing range: (a) Bubble of a (diameter) = 300 μm: (a-1) The bubble surface undulates with an amplitude of ~15 μm under acoustic excitation at 19 kHz; (a-2) Before excitation, 80 μm-dia. glass beads are placed in a row in the radial direction; (a-3) Under excitation, the particle capturing range is > 2a; (b) Bubble of a (diameter) = 1.5 mm: (b-1) The bubble surface undulates with an amplitude of ~30 μm under acoustic excitation at 4.3 kHz; (b-2) Before excitation, 80 μm-dia. glass beads are placed in a row in the radial position; (b-3) Under excitation, the particle capturing range is about 1a.

Similar experiments are made with the bubble of a = 1.5 mm. The peak-to-peak amplitude of undulation is measured to be Δ = 30 μm ($\varepsilon = \Delta/a$ = 2%) at 4.3 kHz (Fig. 24b-1). This normalized undulation amplitude is lower than that for the bubble of a = 300 μm. Acoustic wave generation in the actuator and its transmission through the testing rig are dependent on the

frequency. As shown in Fig. 24b-3, the particle capturing range is a distance of ~ a from the bubble base center. The relative distance to the bubble diameter is shorter than for the bubble of a = 300 μm. This is due mainly to lower ε in the bubble of a = 1.5 mm than in the bubble of a = 300 μm, rather than to the bubble size.

3.3.3 Dependence of excitation frequency and amplitude

Dependence of capturing performance on the amplitude and frequency of acoustic excitation is investigated. First, a bubble of a = 1.2 mm is examined. When the excitation frequency is far from the natural frequency, bubble oscillation is not significant. Five different excitation frequencies near the natural frequency are examined. The excitation frequency f is normalized by the natural frequency f_o = 4.5 kHz. The applied voltage (V) to the actuator is set at three different values (200, 300, and 400 V). In all the cases tested, the bubble mainly has surface-wave undulations since the excitation frequency is close to the natural frequency. Similar surface-wave modes were reported by Tho *et al* [47] when the frequency was set close to the natural frequency. They showed that when the excitation frequency is much lower than the natural frequency, the oscillation mode is translational. As the frequency increases but is still far below the natural frequency, the mode changes to axisymmetric. The oscillation amplitude Δ on the bubble apex, which is dominantly represented by the surface-wave mode (not the axisymmetric mode), is measured for nine conditions (three different frequencies: f/f_o = 0.9, 1, and 1.1; three different voltages V: 200, 300, and 400 V) using high-speed images (Fig. 25a). Of course, the oscillation amplitude at f/f_o = 1.0 and V = 400 V is the highest among the nine cases. In the testing range, the maximum peak-to-peak amplitude is 22 μm ($\varepsilon = \Delta/a$ = 1.8 %). At the other two

frequencies with V = 400 V, the oscillation amplitudes are lowered to 15 μm ($\varepsilon = \Delta/a$ = 1.3 %). Note that the numbers on the bubble images in Figs. 25a and 26a represent ε for the corresponding frequency and voltage condition.

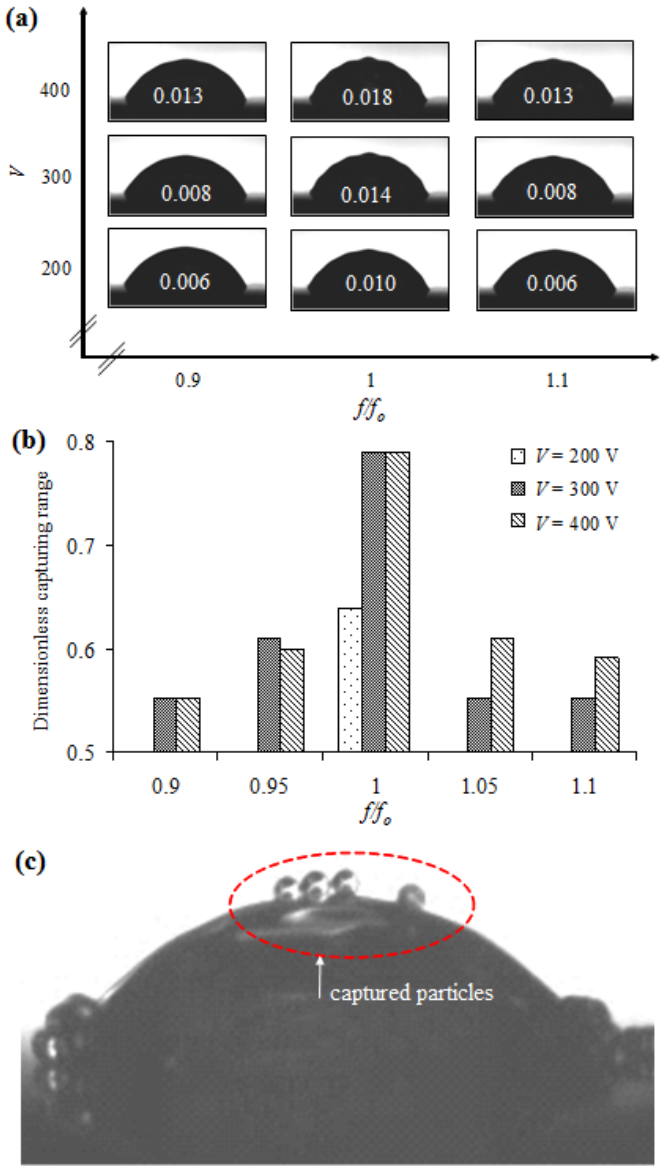

Figure 25 1.2 mm dia. bubble: (a) The oscillation amplitude at the bubble apex is measured from high-speed images with respect to the applied voltage (V) and frequency (f). The number on each image represents the ratio of the peak-to-peak oscillation amplitude in the bubble apex to the bubble diameter (ε). (b) Capturing range with respect to

applied voltages and frequencies. The measured capturing distances are normalized by the bubble diameter (a). Note that the applied frequency is set at the natural frequency (f_o) of 4.5 kHz. (c) Side views of the oscillating bubble with the captured particles. The captured particles stay on the bubble surface.

Generally, for each frequency, the capturing range is proportional to the applied voltage V, as shown in Fig. 25b. Initially, twenty glass particles of 80 μm in diameter are distributed within the distance of ~ a from the bubble center. In order to exclude the effect of the surface tension force between the particles' and the bubble's interface in the capturing and holding process, hydrophilic glass particles are selected as the testing objects. When the bubble is excited at f/f_o = 1.0 and V = 400 V, the capturing range is highest, showing a fairly symmetric behavior with respect to the natural frequency. In addition, the capturing range increases as the applied voltage V increases. Overall, the capturing range is proportional to the bubble oscillation amplitude ε. Figure 25c shows a high-speed image of captured particles orbiting and staying on the bubble surface (f/f_o = 1.0 and V = 400 V).

Similar experiments are carried out with a bubble of a = 300 μm. Figure 26a shows the bubble shape during surface-wave oscillation and the oscillation amplitude for the nine cases (three different frequencies: f/f_o = 0.8, 1.0 and 1.2; three different voltages: 100, 150, and 200 V). The maximum oscillation amplitude Δ is 15 μm ($\varepsilon = \Delta/a$ = 5 %). Overall, ε is higher than for the 1.2 mm bubble. The general trend is very similar to the case for the 1.2 mm bubble: the oscillation amplitude is nearly symmetric with respect to the natural frequency and increases as the applied voltage increases.

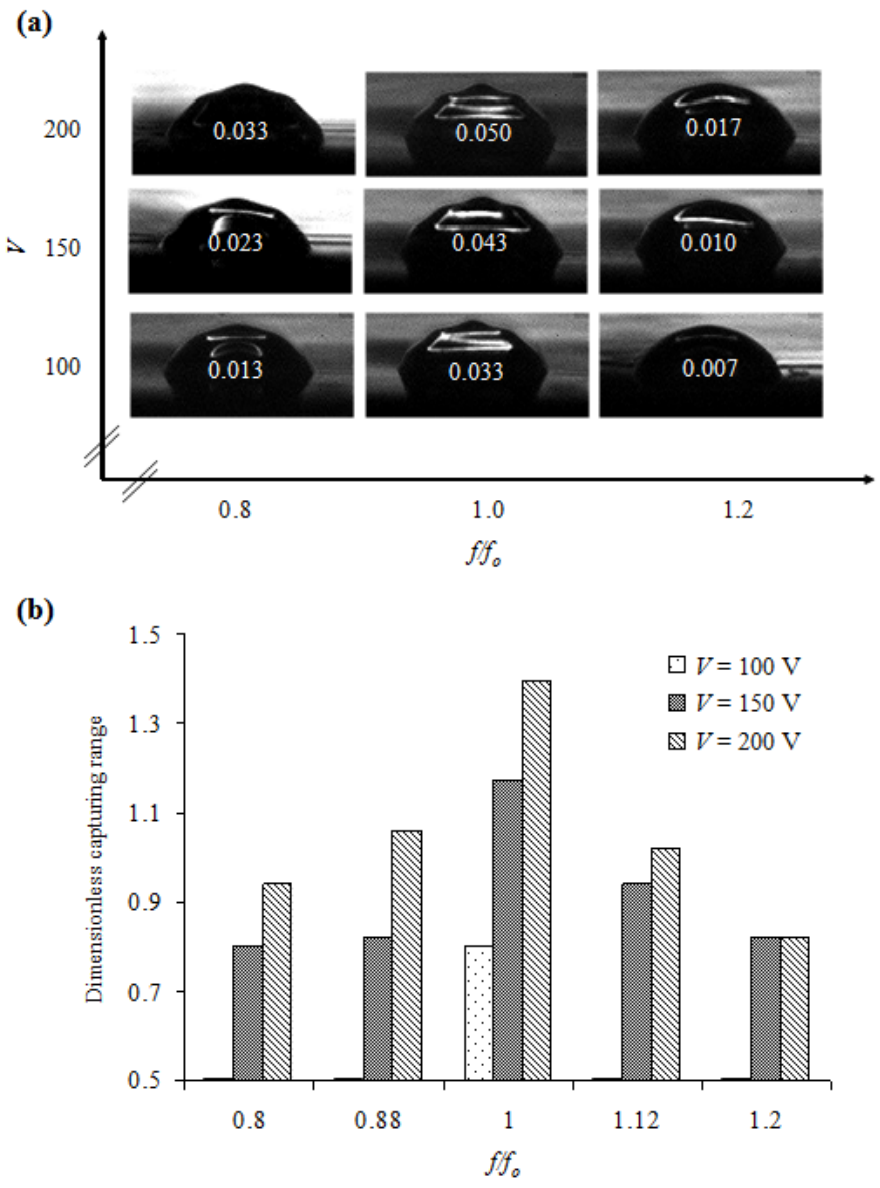

Figure 26 300 μm dia. Bubble: (a) Amplitude of the bubble surface oscillation with respect to the applied voltage (V) and frequency (f). The number on each image represents the ratio of the peak-to-peak oscillation amplitude in the bubble apex to the bubble diameter (ε). (b) Capturing range with respect to applied voltages and frequencies. The measured capturing distances are normalized by the bubble diameter (a). Note that the applied frequency is set at the natural frequency (f_o) of 19 kHz.

As shown in Fig. 26b, the capturing range also shows a similar trend to a = 1.2 mm; it is generally proportional to ε. The capturing performance is effective for a wider range of

excitation frequencies than for the case of a = 1.2 mm. In particular, at f/f_o = 1 and V = 200 V, the captured particle number is more than the initial particle number (13) within the 2a distance from the bubble center. This is because the bubble erratically moves due to strong oscillation and sweeps even the particles that are located out of the capturing range. Note that in the results shown in Figs. 25 and 26 the bubbles are placed on the uniformly Teflon-covered surface. This is different from the cases in Fig. 24 where the bubbles are held by the Teflon circle patterns. The acoustic excitation is turned off when the bubble starts to move laterally. As a consequence, this capturing distance is shorter than the result in Fig. 24 with higher uncertainty. Unless the acoustic excitation is turned off, the number of captured particles would increase continuously. As shown in Fig. 23a, when the excitation is applied for longer than 2 sec, the maximum number of captured particles is more than 60 particles, which is more than the bubble surface area can accommodate. In this case, many of the particles cannot stay on the bubble surface. Instead, they orbit in larger paths, going away from and returning to the bubble surface (Fig. 23a-3). In the other cases for weak bubble oscillations, the bubble stays on the initial position without any lateral motion. The captured particles and range are significantly less and shorter than the case of f/f_o = 1 and V = 200 V.

3.3.4 Integration of capturing, carrying, and releasing

Although high amplitude excitations make the oscillating bubble move laterally and thus carry neighboring objects, the bubble motion is random and not controllable. Using EWOD actuation, the bubbles can be transported on a 2-D solid plane in a controllable fashion. In order to demonstrate a series of integrated operations such as capturing, carrying, and releasing of particles in a controllable way, an EWOD-driving mechanism is incorporated with the acoustic

excitation. Two bubbles of different size (1.5 mm and 300 μm in diameter) are examined, as shown in Fig. 27. Figure 27a shows sequential images for the 1.5 mm bubble. As soon as the piezo-actuator is turned on, the bubble oscillates and captures adjacent particles (80 μm glass beads). The bubble is then transported step-by-step to the right (Fig. 27a-2) by sequentially activating the EWOD electrodes. The voltage of 80 V at 1 kHz is applied for EWOD actuation. Since over 99 % of the applied voltage drops in the dielectric layer, not in the water, we could not see any noticeable effect of the voltage on the attraction of particles. While the bubble is in transportation, the captured particles orbit around the bubble surface. After the bubble crosses two electrodes, the piezo-actuator is turned off. The trapped particles are released from the bubble surface and stay on the bubble rim (Fig. 27a-3). As the bubble is further transported to the right with acoustic excitation off, the particles completely separate from the bubble. In all, nine particles are carried from the initial location. The maximum instantaneous speed of the bubble is measured at approximately 1.5 cm/s from the recorded images. Note that four particles are lost at this bubble speed and remain in the middle of the bubble path. In this case, the carrying efficiency is $9/(4+9) \approx 70$ %. This carrying efficiency can be improved by changing the electrode actuation scheme.

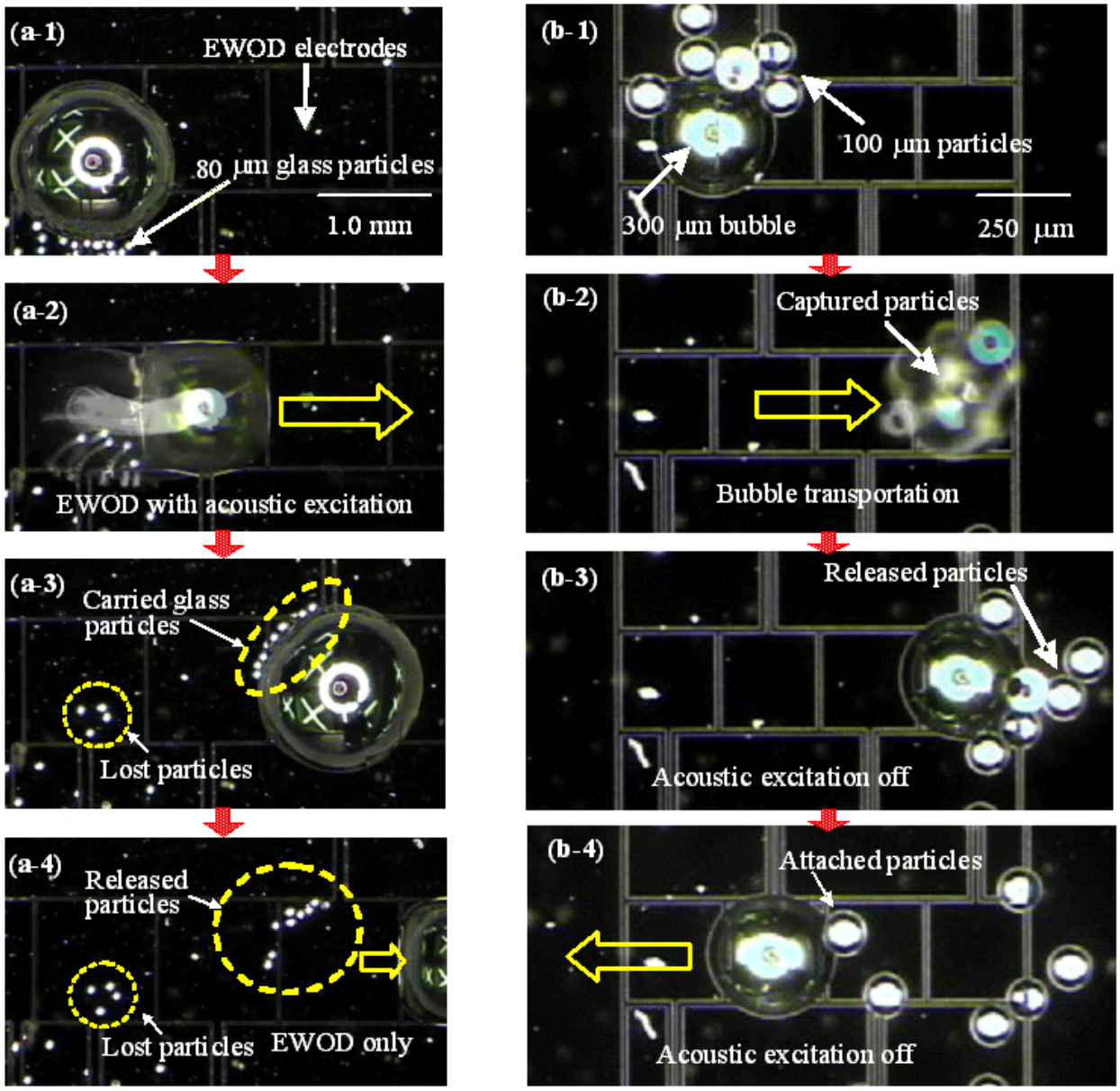

Figure 27 Sequential pictures showing that an oscillating bubble captures, carries, and releases neighboring glass particles: (a) Bubble size 1.5 mm with glass beads: (a-1) Initial state, (a-2) With acoustic excitation (at 4.2 kHz, 300 V) on and EWOD (80 V @ 1 kHz) on, the oscillating bubble captures and carries glass beads (80 μm), (a-3) The carried particles are released with acoustic excitation off, (a-4) The carried particles are completely detached from the bubble when acoustic excitation is turned off, and the bubble continues to move to the right by EWOD only (Note that the captured and carried particles are circled by yellow broken lines); (b) Bubble size 300 μm with polystyrene particles (contact angle ~66°): (b-1) Initial state; (b-2) A 300 μm diameter oscillating bubble captures and carries 100 μm polystyrene particles to the right under acoustic excitation (at 20 kHz, 150 V) and with EWOD

(80 V @ 1 kHz) on, (b-3) Acoustic excitation off, (b-4) Most of the particles, except one, are completely detached from the bubble when the bubble is moved by EWOD to the left with acoustic excitation off. The attachment is due to the particle's hydrophobicity.

In Fig. 27a, except the electrode on which the bubble sits, all the electrodes are activated at the same time. These activations shift step-by-step to the right. As a result, the bubble base is confined to the single non-energized electrode, and the shape of the bubble base becomes a square, similar to the electrode shape, while in motion. As a result, the bubble is significantly deformed. In this case, it is found that the chance for losing the captured particles becomes higher. On the contrary, if two electrodes (one is on which the bubble sits and another is the next right electrode to the bubble) are non-energized with everything else energized, the carrying efficiency becomes higher since the bubble has a more (double) non-energized area on which it can sit while in motion. The results in Table 1 are obtained using the latter scheme, showing higher carrying efficiencies in all five runs (right most column in Table 1).

Similar operations using a smaller bubble (300 μm in diameter) are also examined with glass particles of 80 μm in diameter and polystyrene particles of 100 μm in diameter. Since the present testing system can generate higher ε in smaller bubbles, the carrying efficiency is higher for smaller bubbles than for larger bubbles. Figure 27b shows sequential images of capturing, carrying, and releasing of the 100 μm polystyrene particles using the 300 μm bubble. The bubble captures all six particles initially located near the bubble and carries all of them to the right end of the chip without losing any particles (Fig. 27b-2). After releasing the particles, the bubble moves left (Fig. 27b-3 and -4). At the final state, however, one particle still remains in contact with the bubble surface without complete separation (Fig. 27b-4). This is due to the hydrophobicity of the polystyrene particles. The contact angle of the polystyrene particles is

around 66°. This is much higher than the glass particles and many typical biological objects. This attachment was not observed with the glass particles. Sometimes, attachment may hamper release of hydrophobic objects. One of the methods to mitigate this problem may be to add an extremely small amount of surfactant to reduce the adhesion force between the bubble and hydrophobic objects [85]. To examine the reliability of the above operation, five additional runs are repeated in separate experiments using the glass as well as polystyrene particles, as tabulated in Table 1. For the 300 μm bubble, the average carrying efficiency is 100 % for both glass and polystyrene particles. For the 1.5 mm bubble, it is 95 % for the glass particles.

Table 1 Carrying efficiency. The particle numbers are shown after and before carrying operations (the 300 μm bubble is excited at 20 kHz, 150 V and the 1.5 mm bubble is excited at 4.2 kHz, 300 V).

Case #	300 μm dia. bubble with 80 μm glass beads			300 μm dia. bubble with 100 μm polystyrene beads			1.5 mm dia. bubble with 80 μm glass beads		
	# of captured particles	# of carried particles	(%)	# of captured particles	# of carried particles	(%)	# of captured particles	# of carried particles	(%)
1	2	2	100	5	5	100	3	3	100
2	3	3	100	6	6	100	4	3	75
3	3	3	100	6	6	100	5	5	100
4	5	5	100	8	8	100	5	5	100
5	6	6	100	9	9	100	13	13	100
Total	19	19	100	34	34	100	30	29	95

3.4 SUMMARY

When an air bubble resting on a solid surface in water is acoustically excited near the natural frequency, the bubble oscillates with undulations on the bubble surface, called surface wave oscillation. It is found that this oscillation generates a strong attraction force, and as a result the

bubble captures neighboring solid objects. A variety of objects including glass beads (80 μm), polystyrene beads (100 μm), a fish egg (~ 1 mm), and a live water flea (~ 1 mm) are successfully captured; however, small particles (≤ ~ 10 μm) are not captured but instead follow cavitational microstreaming vortical flows. In addition, it is first shown that when the medium density is lower than the object density repulsion occurs between the bubble and object. This result qualitatively proved Miler's simplified model. Capturing performance for two bubbles of different sizes (300 μm and 1.2 mm) is characterized using 80-μm hydrophilic glass particles. In this characterization, the excitation frequency and amplitude are varied, and high-speed images of the bubbles are taken to measure the oscillation amplitude of the bubbles. At the natural frequencies the capturing range is highest. The capturing range increases as the oscillation amplitude increases. The trapping force is strong enough to hold the captured objects while the bubbles are in lateral motion. By integrating acoustic excitation with electrowetting-on-dielectric (EWOD) bubble transportation, it is demonstrated that oscillating mobile bubbles can capture, carry, and release neighboring objects as desired, showing high carrying efficiencies for glass and polystyrene beads. This on-chip manipulation method may provide an efficient, non-invasive tool for handling millimeter- as well as micron-sized objects such as biological cells and other entities.

4.0 ON-CHIP OBJECT MANIPULATION ONLY USING AC-EWOD

4.1 INTRODUCTION

In Chapter 3, micro-object manipulations - capturing, carrying, and releasing - have been studied on a 2-D plane using two simultaneous actuations: (1) acoustic excitation by a piezo-actuator for capturing objects and (2) electrowetting actuation for bubble transportation. This chapter describes similar micro-object manipulations on a 2-D plain but the major difference is to use a single actuation: AC-EWOD. AC-voltage-driven EWOD is solely used for both bubble oscillation and transportation (Fig. 28), with no need for acoustic excitation. Detailed operational steps are shown in Fig. 28. The AC voltage (low frequency) oscillates the bubble in order to capture and hold neighboring objects while the bubble is moving as well as at rest. (Figs. 28b and c). The capturing highly depends on the AC-signal frequency, implicating that the frequency can be used to control capturing and releasing of objects. By switching the AC electrowetting signal in the electrode array the oscillating bubble can be transported (Fig. 28c), simultaneously carrying the captured objects. The captured particles can be completely released in an on-demand manner by changing the frequency of electrowetting signal (Fig. 28d).

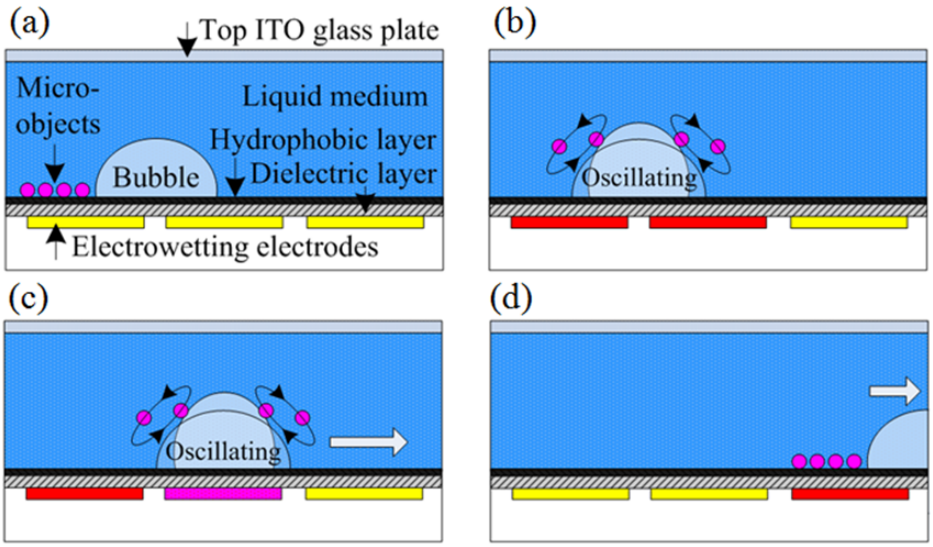

Figure 28 Capturing, carrying, and releasing of objects by an AC-electrowetting-actuated oscillating bubble. (a)-(b) Low-frequency electrowetting (100 Hz) on two red electrodes oscillates the gaseous bubble such that an attraction force generated around the bubble captures neighboring objects. (c) As the pink electrode is momentarily turned off, the oscillating bubble is moved right. Note that low-frequency electrowetting (100 Hz) is used for both bubble transportation and oscillation (particle capturing). As a result, the captured particles are carried by the bubble. (d) When EWOD actuation frequency is changed from 100 Hz to 1 kHz, the continued bubble transportation completely separates the captured particles from the bubble.

4.2 FABRICATIONS

To transport bubbles in a controlled manner, the patterned and arrayed electrowetting electrodes are micro-fabricated using the similar fabrication method (described in Chapters 2 and 3) (Fig. 29). The main difference is that there is no piezo-actuator. The fabricated testing chip is of two-plate channel with bubbles and filler liquid in between. The main fabrication process on the bottom plate consists of three steps: metallization and patterning of electrodes, deposition of the dielectric layer, and deposition of the hydrophobic layer, as illustrated in Fig. 29. For the driving

electrodes, a chromium layer of 100 Å in thickness as an adhesion layer and a gold layer of 2000 Å in thickness are sequentially deposited on a glass wafer by a sputter and then patterned by wet etching. Each driving electrode is of square type with an area of 1.0×1.0 mm^2. Then, a 3 μm thickness photoresist layer as the dielectric layer is deposited using a spinner. Finally, the bottom plate is finished with a hydrophobic Teflon layer. Spin-coating of 2 % Teflon solution (Teflon AF 1600® + Fluorocarbon solvent) results in a 2000 Å thick Teflon layer. Meanwhile, the top glass cover coated with an ITO (Indium Tin Oxide) layer is also spin-coated with the hydrophobic Teflon layer. The transparent ITO layer covering the entire area of the top cover glass makes bubble motions visible.

The last step of the fabrication process is to integrate the two plates (Fig. 29(e)). After putting a large water drop on the bottom plate, the top cover plate is gently pressed against the spacers that are already placed on the bottom plate. The double-sided tape of about 150 μm thickness is used for the spacers. The gap between the top and bottom plates is fixed at around 750 μm by putting 5 layers of the tape in stack.

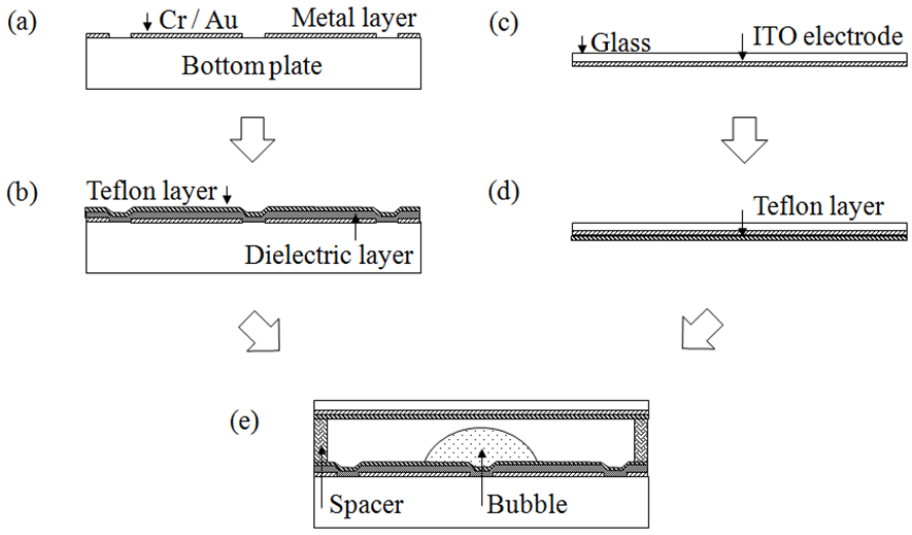

Figure 29 Microfabrication process of testing device: (a) patterning of electroweting electrodes on bottom plate; (b) deposition of dielectric layer (photoresist) and hydrophobic Teflon layer on bottom plate; (c) deposition of ITO on top glass plate; (d) deposition of hydrophobic Teflon layer on top glass plate; (e) Integration of top and bottom plates with a spacer.

4.3 RESULTS AND DISCUSSION

4.3.1 Measurement of oscillating bubble amplitude with respect to frequency

Since oscillation amplitude is directly correlated to capturing strength [32, 86], dependency of bubble oscillation amplitude on the AC-electrowetting frequency is studied first (Fig. 30) with a capped bubble. This experiment is conducted in a water chamber ($5 \times 5 \times 2.5$ cm^3 with 1.5 cm water level). An electrowetting electrode is immersed in the water chamber and placed on the bottom of the chamber. Air bubbles are injected directly on the hydrophobic top surface of the electrowetting electrode using a pipette. The applied signal for electrowetting actuation is generated by a function generator, amplified by a power amplifier, and transmitted to the EWOD

electrode. To view bubble motions, the testing chip is placed under a microscope (EO Edmund optics Co.) that is connected to either a regular CCD camera (CV-S3200, JAI Co.) or a high-speed camera (Phantom v7.3, Vision Research Co.).

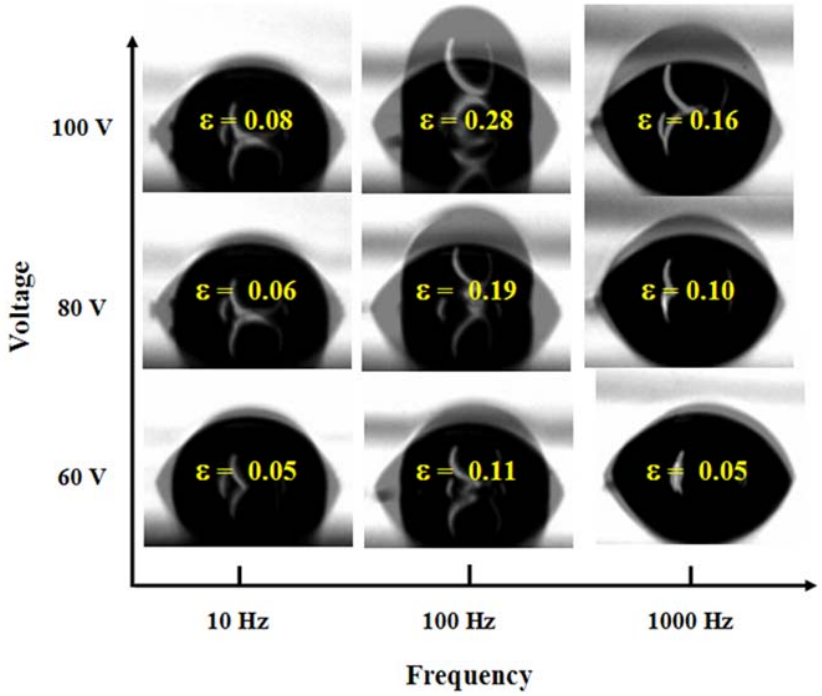

Figure 30 The oscillation amplitude at the bubble (300 μm dia.) apex is measured from high-speed images with respect to the applied electrowetting voltage and frequency. The number on each image represents the ratio of the peak-to-peak oscillation amplitude to the bubble diameter (ε). Note that an electrowetting electrode covers the entire surface the bubble sits on.

The electrowetting electrode covers the entire surface the bubble sits on, thus generating axisymmetric bubble oscillations. The high-speed images of 300 μm bubble show that bubble oscillation reaches maximum at the frequency 100 Hz (Fig. 30). To measure the oscillation amplitude, the captured images are overlapped together. A similar trend appears for 1 mm bubble

(Fig. 31). Note that the maximum oscillation of 1-mm bubble is much larger than that of 300 μm bubble.

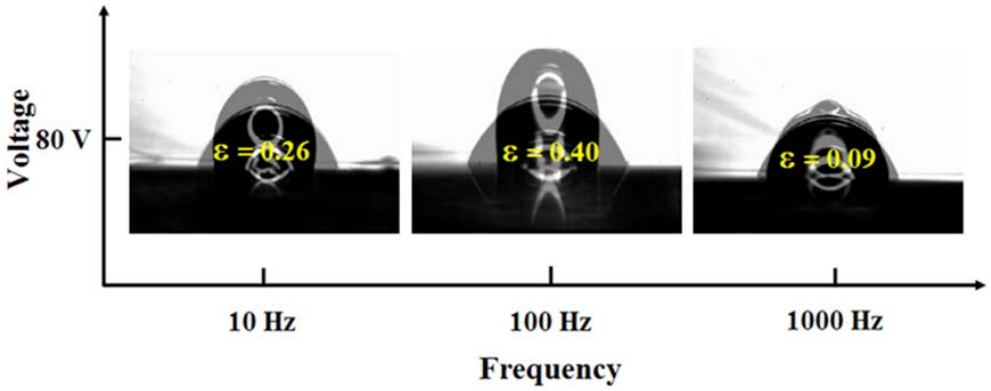

Figure 31 The oscillation amplitude at the bubble (1 mm dia.) apex is measured from high-speed images with respect to the frequency.

4.3.2 Capturing of objects

Figure 32 shows results of particle capturing using AC-EWOD oscillations. The experiment is conducted in the same water chamber as in Fig. 30. Air bubbles are injected directly on the top surface of the electrowetting electrode using a pipette, and glass beads (80 μm) and a fish egg are placed around the bubbles using the same pipette (Fig. 32). An AC-electrowetting electrode also covers the entire area of solid surface.

When the bubble (~400 μm dia) is oscillated by AC electrowetting of 100 Hz, neighboring glass beads (80 μm) are captured on the bubble (Fig. 32a-1-2); however, when the frequency is shifted to 1 kHz, the capturing is not significant (Fig. 32a-3) due to small oscillation amplitude. Similar results appear in the 1 mm bubble (Fig. 32b1-2). Figure 32c shows that the

oscillating bubble randomly moves on the surface due to large oscillation amplitude, captures, and carries a fish egg without losing it while in lateral motion. This result means that the capturing force is strong enough to carry objects. However, as compared to the acoustic excitation, the capturing force seems to be weaker. This may be due to the fact that the frequency in this case is much lower than the acoustic excitation as predicted in Eq. (12).

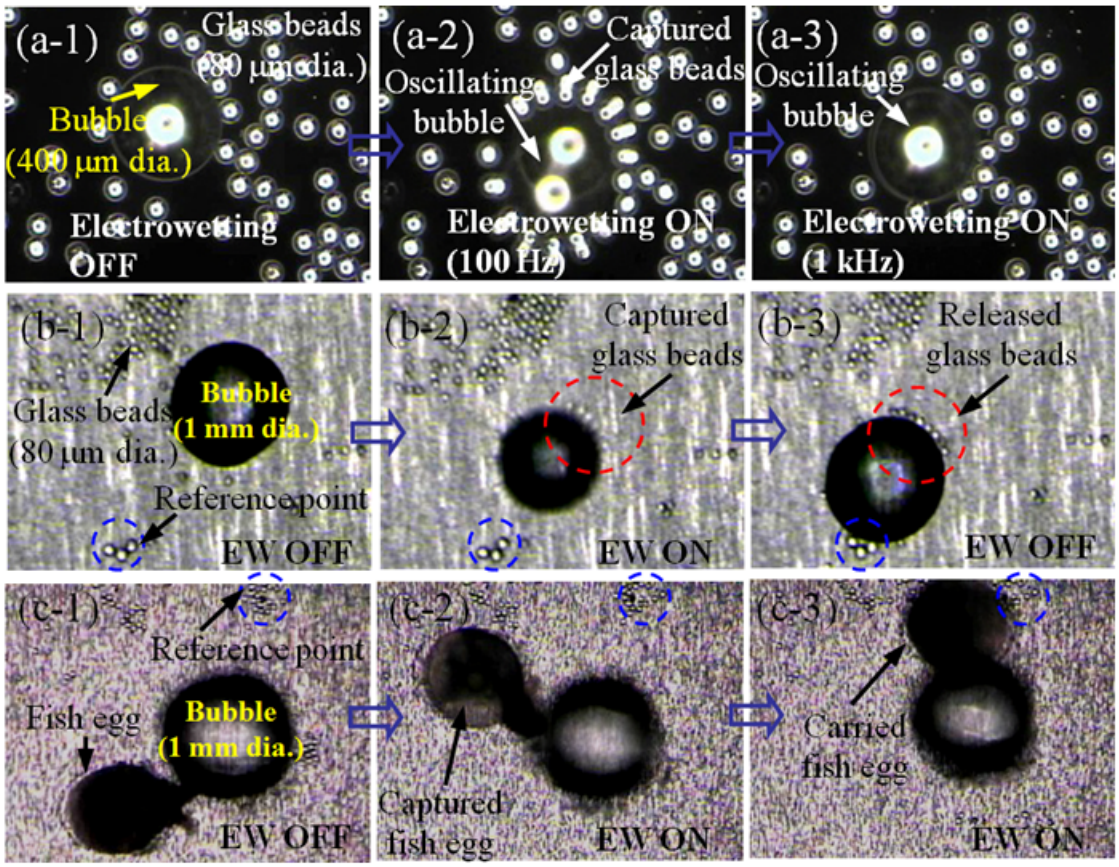

Figure 32 Capturing and carrying of glass beads and a fish egg using oscillating bubbles: (a-1) Initial state (bubble size ~400 μm), (a-2) Strong capturing of glass beads (100 Hz AC electrowetting), (a-3) Weak capturing (1 kHz AC electrowetting); (b) Similar to case (a) except bubble size (~1 mm dia); (c-1) Initial state, (c-2) A fish egg (~ 1 mm) is captured on the oscillating bubble (100 Hz AC-electroweting), (c-3) When the bubble moves randomly due to large oscillation, the fish egg is carried by the bubble.

4.3.3 Integrated micro-object manipulations: capturing, carrying, and releasing

In order to laterally transport captured objects in a controlled manner, an array of patterned electrodes is used. First, a large water droplet is placed on the testing chip covering almost the entire area of the arrayed electrowetting electrodes. After injecting a small bubble and glass beads (80 μm) near the bubble in the droplet using a pipette, a top glass cover is gently placed against spacers on the bottom electrowetting electrodes (Fig. 29(e)). Water fills in the space between the top and bottom plates.

Sequential images (Fig. 33) show that a 1 mm bubble captures 80 μm glass beads on the bubble rim when all the electrodes are connected to AC-electrowetting signal (80V, 100 Hz) (Fig. 33b). Momentarily turning off the second right electrode (others are on) makes the bubble move one step right and simultaneously carries many captured beads (Fig. 33c). Shifting this switching procedure to the next right electrode repeats this operation one more time (Fig. 33d-e). While the bubble is moving, some particles are lost from the bubble (Fig. 33e). However, this may be able to be minimized by fine control of actuation signal timing. In order to completely release the captured beads, the bubble is transported right again using 1 kHz signal (not 100 Hz). None of particles remain on the moving bubble (Fig. 33f) since bubble oscillation at 1 kHz is weak. However, bubble transportation is not susceptible to the EWOD driving frequency as far as the frequency remains typically below 1 kHz.

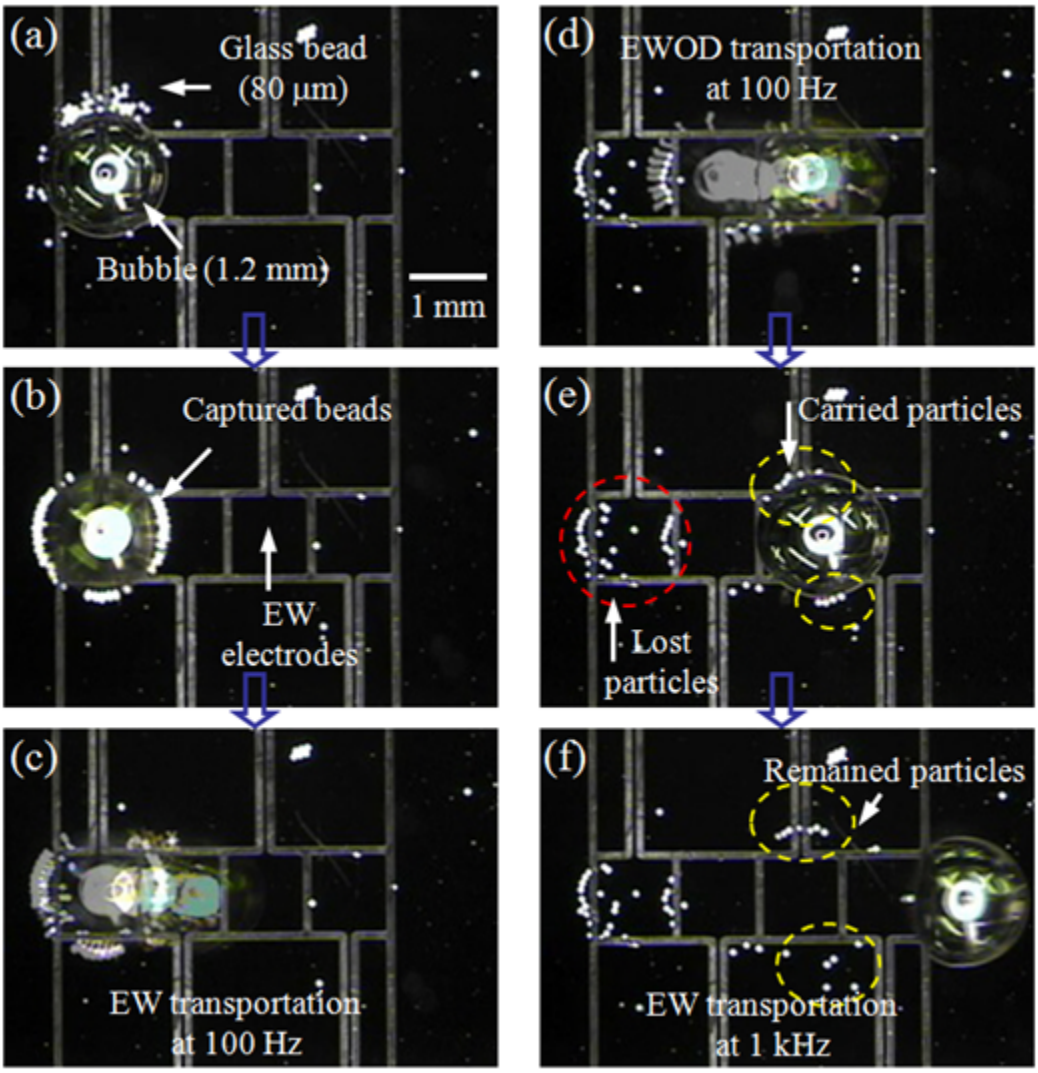

Figure 33 Sequential pictures showing that an oscillating bubble captures, carries, and releases neighboring glass beads: (a) Initial state, (b) The glass beads are captured on the bubble under EW actuation (100 Hz), (c-e) Momentary switching-off of the next right electrode on which the bubble will sit makes the bubble move right with holding the beads; however, some of them are detached from the bubble and remain behind, (f) When the bubble moves to right with 1 kHz EW actuation, it leaves all carried particles behind due to low oscillation amplitude.

4.4 SUMMARY

This chapter describes object manipulations along with experimental proof where gaseous bubbles oscillated/driven by AC-electrowetting capture and carry neighboring micro/mini objects. Unlike the case in Chapter 3, this method uses a single actuation without acoustic excitation. AC-electrowetting is used for bubble oscillation as well as bubble transportation. The oscillation amplitude of the bubbles is quantified using high-speed images while varying the acoustic excitation frequency and amplitude. The results show that the oscillation amplitude is maximum around 100 Hz. Using AC-EWOD -driven oscillating bubbles, capturing behavior is examined. Consistent with the oscillation amplitude, the capturing strength is highest at 1 kHz bubble oscillation. However, due to low frequency the capturing performance is not as good as the dual actuations in Chapter 3. Finally, it is demonstrated using arrayed EWOD electrodes that oscillating mobile bubbles can capture, carry, and release neighboring objects on a chip.

5.0 3-D OBJECT MANIPULATION: CAPTURING, CARRYING, AND RELEASING

5.1 INTRODUCTION

In Chapters 3 and 4, micro-object manipulations - capturing, carrying, and releasing - have been studied. However, these methods are effective only on a 2-D plane, not 3-D space since the bubbles stick to a 2-D surface. This chapter presents 3-D manipulations of objects using the similar capturing principle (i.e., an acoustically excited oscillating bubble). The working principle is illustrated in Fig. 34. A millimeter- or micron-sized bubble is deposited on a hydrophobic rod tip, which is immersed in a water chamber and connected to a 3-D traversing system (Fig. 34a). As a result, the bubble tip can be traversed in any positions in the water chamber. When a bubble on the tip is excited by a piezo-actuator attached beneath the bottom of a water chamber, the bubble oscillates and generates a radiation pressure force, capturing micro-objects near the oscillating bubble (Fig. 34b). The capturing force by the oscillating bubble is strong enough to carry the captured objects in a 3-D space in a water chamber (Fig. 34c). By turning off the acoustic excitation, the captured objects can be easily released at a desired position and time (Fig. 34d). A series of these operations (capturing, carrying, releasing of objects) can constitute fundamental units in the 3-D manipulation task.

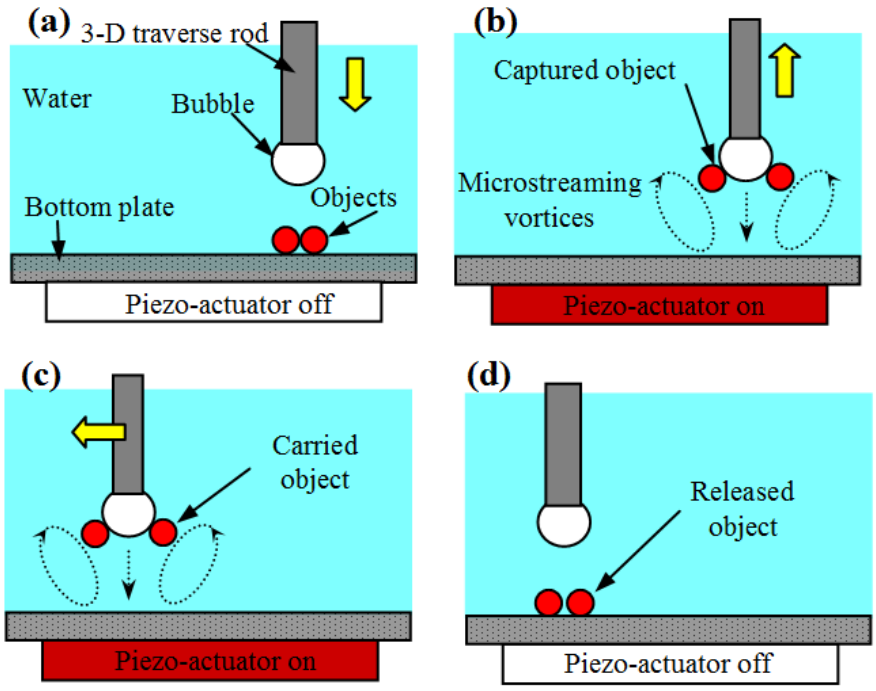

Figure 34 3-D manipulation: capturing, carrying, and releasing of millimeter- or micron-sized objects by an oscillating bubble attached on a 3-D traversing rod. (a) The bubble tip approaches the objects. Note that the piezo-actuator beneath the bottom substrate is still off. (b) When the bubble reaches close enough to the objects, the piezo actuator is turned on and oscillates the bubble. The oscillating bubble generates an attraction force and thus captures the objects. The dotted lines indicate vortical flows induced by the oscillating bubble (cavitational microstreaming) (c) The captured objects are carried as the rod is traversed in a 3-D space. Also note that the piezo-actuator remains on while the bubble is traversing. (d) When the bubble reaches a destination, the piezo-actuator is turned off, resulting in releasing the carried objects.

5.2 RESULTS AND DISCUSSION

5.2.1 3-D object manipulations

For the 3-D manipulation, similar water chamber and acoustic excitations are used as described in Chapter 3. Figure 35 shows that an oscillating bubble captures, carries, and releases various objects. A fish egg (about 1.5-mm in dia., Fig. 35a) is initially placed on a silicon plate (2 × 2 cm^2) immersed in a water chamber (5 × 5 × 2.5 cm^3 with 1.5 cm water level). The primary sound pressure field in the water chamber generated by the piezo-actuator is assumed to be homogeneous without pressure nodes and antinodes under the applied acoustic frequencies due to large wave length. When a bubble (diameter D = 1.3 mm) deposited on a Teflon tip reaches the fish egg, the disk type piezo-actuator (25 mm dia., Omega Piezo Co.) glued to the bottom of the water chamber is turned on at the frequency of f = 4.5 kHz (near the bubble resonance frequency). Due to the large quantity of bulk water in the chamber, the temperature increase is less than 0.5 °C for 5 minutes excitation. The resonance frequency f_o is measured at the frequency where the oscillation amplitude of a certain size bubble becomes maximum. Using Minnaert's equation [82] or $f_oD \cong 6$ kHz•mm in standard condition [83], f_o can be roughly predicted although the equation is developed for a suspended spherical bubble in medium, not hanging bubbles on a surface. A sound pressure wave is then transmitted to the bubble on the tip and oscillates the compressible bubble in harmony with f.

The bubble oscillation generates an attraction force between the bubble and the neighboring fish egg, resulting in capturing of the fish egg on the oscillating bubble surface (Fig. 35a-1). Even while the rod mounted on a 3-D traversing system is being traversed up and left, the captured fish egg remains held on the bubble (Fig. 35a-2). The capturing force is large

enough to hold and carry the fish egg during transportation. When the rod tip reaches its destination, the captured fish egg is released from the bubble by turning off the piezo-actuator, and finally lands on the silicon bottom plate (Fig. 35a-3). Since the fish egg surface is hydrophilic, it can be easily detached from the bubble via gravity. This means that the interfacial force (surface tension) between the bubble and fish egg is negligibly small compared to the gravity force on the fish egg, i.e., not a responsible force for holding and carrying of the fish egg.

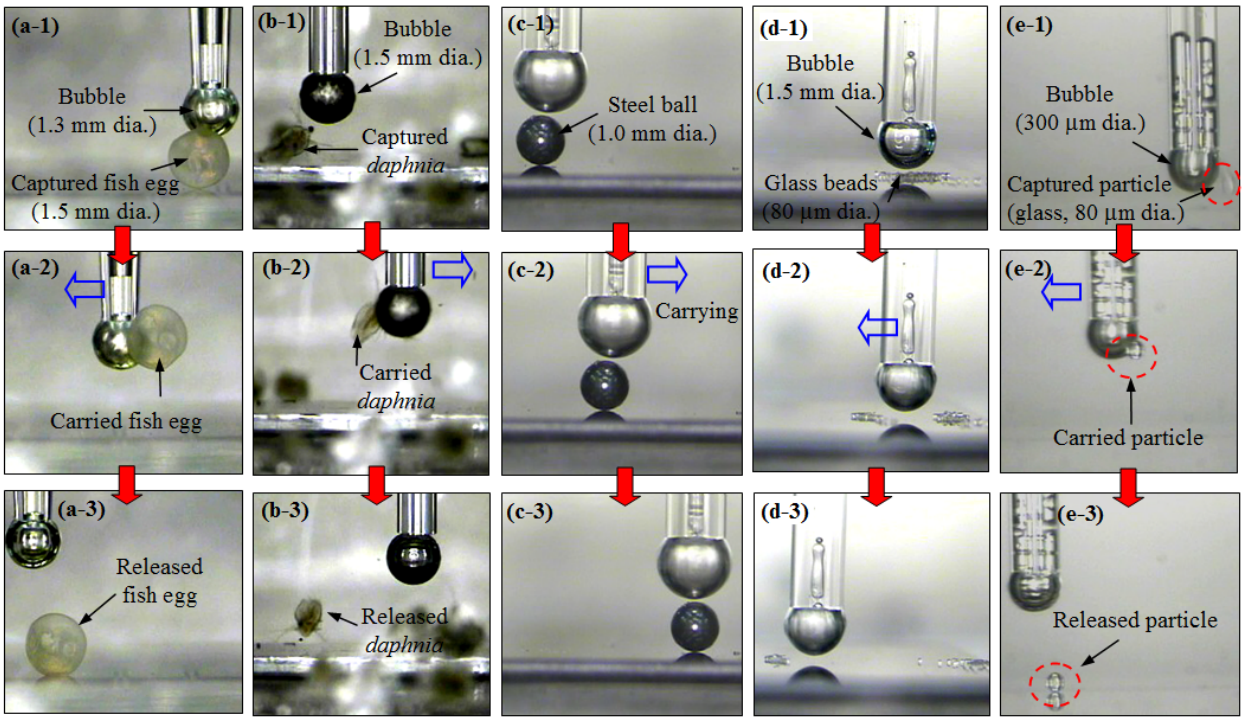

Figure 35 Sequential images of manipulation of millimeter- and micron-sized objects. Note that the rod tip is made hydrophobic to hold a bubble, and all bubbles are excited near their resonant frequency: The bubbles in (a-d) are in a millimeter size and acoustically excited at 4.5 kHz. (a) The fish egg and (b) the live water flea are captured by the oscillating bubbles, carried while the tip traverses, and released when the acoustic excitation is turned off. (c) The steel ball (1-mm dia.) is captured and carried by the oscillating bubble, although it cannot be completely lifted off the bottom surface due to high density. Note that the bubble is not in contact with the steel ball (non-contact manipulation). (d) When the bubble is excited before the bubble approaches the small objects (80-µm dia. glass

bead), the oscillating bubble generates a repelling force, dividing and moving particle clusters on the surface. This is due to the microstreaming vortical flow induced around the bubble. (e) The bubble is 300 μm in diameter and excited at 19 kHz. Similarly, the oscillating bubble captures, carries, and releases an 80-μm dia. glass particle.

This operation is also effective (Fig. 35b) with a live water flea (*Daphnia*, ~ 1.5 mm in size). The water flea makes several strokes to swim away from the oscillating bubble but is attracted back to the bubble (Fig. 35b-1 and -2). Only when the actuator is turned off is the water flea able to swim away from the bubble (Fig. 35b-3). After the capturing process, the water flea is still alive. Assuming that the capturing force exceeds the maximum propelling force the water flea can generate in quiescent water, Stokes drag estimates the capturing force to be approximately 90 nN. A similar-size but high-density object (1.0-mm dia. steel ball) is examined (Fig. 35c). Due to high density, the steel ball cannot be completely lifted off the surface. The capturing force is not larger than the gravity force on the steel ball (= density difference between the ball and water × volume × g ≈ 30 μN). Yet it is strong enough to laterally pull and move the steel ball while staying on the surface. In some conditions (Fig. 35d), interestingly, the oscillating bubble can push the small particles, thus dividing and moving particle clusters. The main difference from the capturing conditions above is that the bubble is initially placed at a distance (about 100 μm or larger) from the particles before the acoustic excitation is applied. So the particles are exposed to the outward microstreaming flow [46, 47] generated by the oscillating bubble. However, this repelling is not observed with millimeter-sized objects, which are comparable to or lager than the induced vortices.

Similar operations (Fig. 35e) are examined using a smaller bubble (300 μm dia.). Tested objects are glass (80 μm dia.) and polystyrene (100 μm dia.) beads. Such a small bubble is generated and grown by electrolysis using Pt electrodes on the bottom of the surface as shown in

Fig. 36 [31]. This electrolytic bubble creation is extensively studied in Chapter 2. As soon as the hydrophobic rod tip (230 μm dia.) touches the grown bubble, the bubble is easily transferred and deposited on the tip due to tip hydrophobicity as shown in Fig. 36b. Meanwhile, when the rod tip is hydrophilic, the created bubble is not transferred from the surface to the rod tip (Fig. 36a). Successful operations of capturing, carrying, and releasing are shown in Fig. 35e. The bubble is excited at f = 19 kHz (near the resonant frequency). The manipulation operations are confirmed to be effective as well with 100 μm polystyrene beads (less dense and less hydrophilic than the glass beads, not shown). In addition, a highly hydrophobic object such as a small piece of Teflon (contact angle of ~ 120^{o} with water) is also easily captured by an oscillating bubble, but it is difficult to release (detach) them from the bubble due to strong surface tension between the piece and bubble. It is confirmed that the operations of capturing, carrying, and releasing are also effective when the piezo-actuator is mounted on the base of the rod tip, rather than on the bottom of the water chamber.

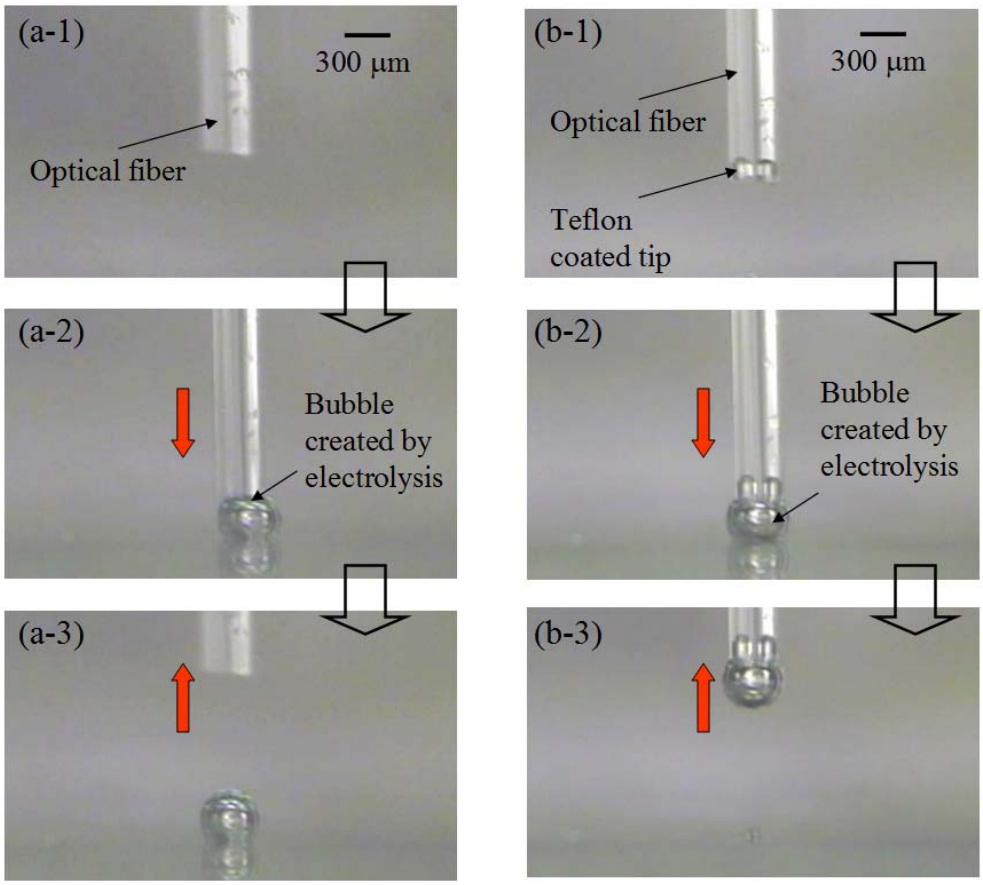

Figure 36 Sequential images of bubble creation and transportation. (a) Without Teflon coating layer on a rod tip: (a-1) Initial state - optical fiber (300 μm diameter) in water chamber; (a-2) After a bubble (300 μm diameter) is created by electrolysis on the bottom platinum patterned electrodes, the rod tip moves down and touches the created bubble by 3-D traverse systems; (a-3) when the rod moves up, the bubble stays on the bottom plate due to the bottom surface being more hydrophobic. (b) With Teflon coating layer on a rod tip; (b-1) Initial state; (b-2) After a bubble (300 μm diameter) is created, the rod tip moves down and touches the created bubble by 3-D traverse systems; (b-3) when the rod moves up, the bubble is transported to the rod tip and stays because the rod tip is more hydrophobic than the bottom electrodes. Note that bubbles prefer to stay in a hydrophobic site.

5.2.2 Quantification of capturing performance

Carrying performance is characterized by varying the excitation condition (voltage and frequency of the applied signal to the piezo-actuator). Figure 37 shows whether the captured particle (80 μm glass) is held on or departs from the oscillating bubble while the bubble rod tip is traversed by a motorized traversing system at three different carrying speeds. To quantify the excitation condition, the peak-to-peak oscillation amplitude Δ at the bubble apex is measured using high-speed images (insets) and is normalized by the bubble diameter D ($\varepsilon = \Delta/D$). Due to the lack of access to a small pressure probe, the transient pressure field was not measured. However, the oscillation amplitude is considered to be a better parameter to describe the excitation condition. In all tested cases, the bubbles have surface undulations (surface mode) [47, 86] when they are excited near the resonant frequency.

Generally, as shown in Fig. 37, the higher ε the stronger the capturing force. Near the resonant frequency f_o (≈ 19 kHz), the captured particles are still held on the oscillating bubble while being carried at all the tested carrying speeds (1, 2, and 3 mm/s). As the frequency becomes far from f_o, the captured particle easily departs from the bubble. As the applied voltage V increases, the capturing force becomes stronger. From the Stokes drag relation, the capturing forces are estimated to be approximately over 4 nN for the 80-μm glass particle.

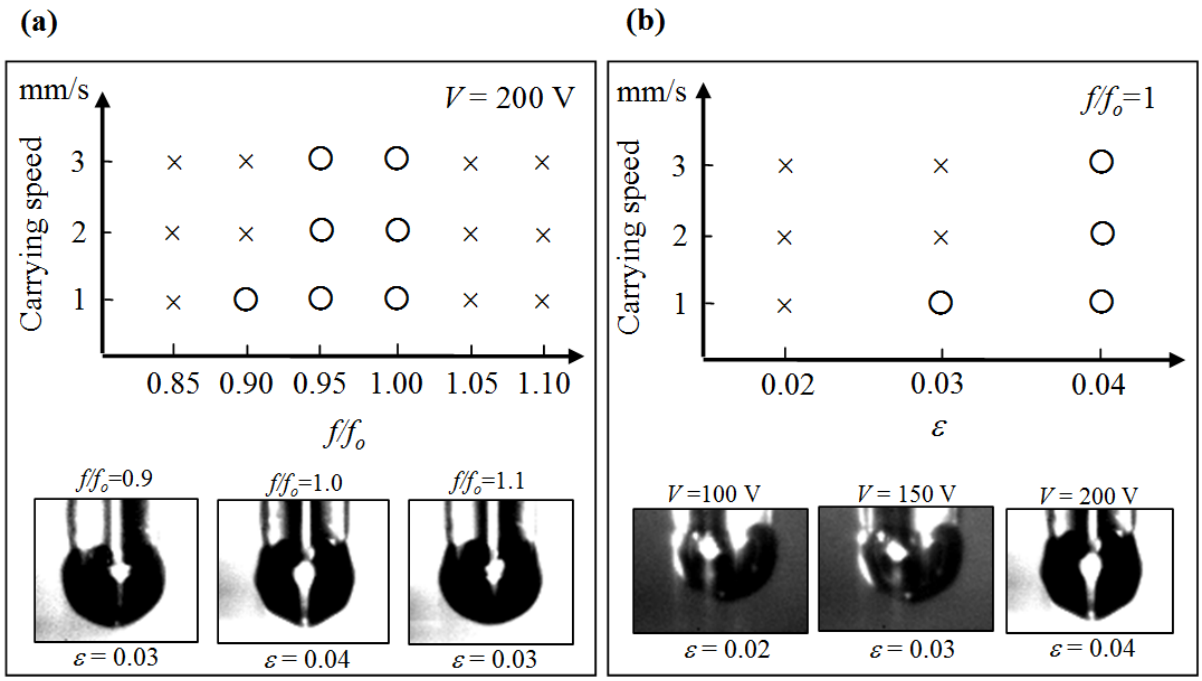

Figure 37 Quantification of carrying efficiency. "O" denotes that the oscillating bubble still holds the particle while carrying whereas "×" denotes that the carried particle departs from the oscillating bubble. The insets are images from a high-speed camera showing bubble oscillations. In all cases, the bubbles oscillate with surface undulations ($\varepsilon = \Delta/D$). Using the high-speed images, the oscillation amplitude (Δ) is measured at the bubble apex and normalized by the bubble diameter (D). (a) The carrying speed vs the excitation frequency. The excitation voltage is fixed at 200 V. At all the tested carrying speeds, the bubble oscillating near its resonant frequency f_o (i.e., ε is highest) holds the particles. (b) As the excitation voltage increases, ε increases, and thus the particle is held and carried at higher carrying speeds. The excitation frequency is fixed at 19 kHz (near its resonant frequency f_o).

5.3 SUMMARY

3-D manipulations of objects are presented using an acoustically excited oscillating bubble. Unlike manipulations in Chapters 3 and 4, the oscillating bubble is deposited on a hydrophobic rod tip and traversed in a 3-D space. The oscillating bubble captures various millimeter- and

micron-sized neighboring objects including glass and polystyrene beads (~100 μm), fish egg, and live water flea (~1 mm). The captured objects are carried in a 3-D space by traversing the bubble tip and released at desired positions by simply turning off the oscillation.

Carrying performance is characterized along with high speed imaging of oscillating bubbles by varying the frequency and amplitude of the acoustic excitation and the carrying speed. The higher the oscillation amplitude the higher the carrying efficiency. The maximum carrying speed is measured at over 3 mm/s. This method is effective with a low-level acoustic excitation (bubble oscillation amplitude relative to the diameter ≤ 5%), possibly providing a cost-effective, soft-contact 3-D manipulating tool for handling biological objects.

6.0 PROPULSION USING AN OSCILLATING BUBBLE

6.1 INTRODUCTION

As an exploratory work, in this chapter, the cavitational streaming flow is further applied to manipulate objects larger than the oscillating bubble. An ultimate goal is to propel and maneuver the mini/micro objects. Development of underwater micro-robots is of increasingly growing interest for drug delivery, bio-sensing, and bio-surgery inside human body. So far, several mechanisms for propulsion in small-scale underwater robots have been investigated and developed. Most of the underwater robots propelled by small actuators or motors are typically larger than millimeter size. Inspired by fish swimming, Kim *et al* [87] developed a millimeter-sized biomimetic underwater robot, which swims in water by moving its tail-fin using ionic polymeter-metal composite actuators.

To reduce the size of underwater robots the groups of Whiteside [88] and M. Sitti [89] have used microorganisms for the propelling power source. The locomotion of the microorganisms that are attached to a microscale object through chemical surface treatment is used to propel the object. Although they have demonstrated carrying and releasing of a few micron-sized polystyrene beads using the microorganisms, it is still challenging to directly control the microorganisms to steer and navigate the object. Using electrochemical reaction, Paxton et al [90] demonstrated propulsion of a nanoscale rod in H_2O_2 aqueous medium. The

outer surface of a half of the rod (370 nm diameter with 2 μm length) was covered with gold and the other half was covered with platinum. The platinum surface, a good catalyst, dissociates H_2O_2 into H_2O and O_2. As a result, the rod was propelled by the gradient of the O_2 along the rod axis. However, the above propelling expamples require complicated structures and driving mechanisms. Furthermore, they potentially have an adverse effect that microorganisms or toxic chemicals may be harmful to the environment, particularly inside human body.

The present propulsion principle that uses acoustically oscillated bubbles does not require any mechanical moving parts and electric wiring. Both strength and direction of the propulsion are highly controllable by changing the frequency and amplitude of the applied acoustic wave. The propulsion mechanism is illustrated in Fig. 38. The unique feature is to utilize the cavitational microstreaming flow that is generated when an acoustic wave is applied to a gaseous bubble (Fig. 38a). The general streaming flow is a toroidal vortical structure with a straight outgoing flow above the oscillating bubble. This overall flow pattern generates a net momentum flux away from and toward the substrate.

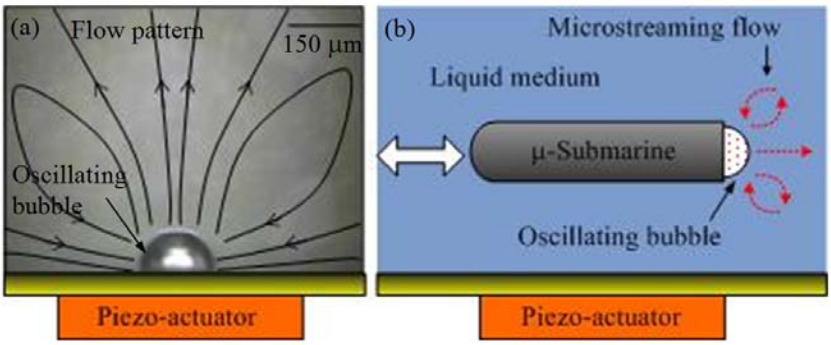

Figure 38 (a) Cavitational microstreaming flow around an oscillating bubble: When the bubble (150 mm dia.) is excited by the piezo-actuator at 25 kHz, large circulation flow patterns are formed around the bubble, generating a net momentum flux away from or towards the substrate. 10 μm polymer particles are seeded and suspended for flow

visualization; (b) Propulsion principle: when a bubble attached to the tip of μ-submarine is acoustically excited, the submarine is propelled forward or backward by the microstreaming flows.

An important innovation in this mechnism is to utilize reaction forces pushing or pulling the substrate, which occur in response to the induced momentum flux. Figure 38(b) shows the concept of the underwater propulsion. When a bubble sitting on the tip of a microscale rod is acoustically excited, the bubble generates cavitational flow around it, resulting in creating a net momentum flux away from and toward the rod depending on the applied frequency. The momentum flux propels the underwater robot in horizontal directions.

6.2 THEORETICAL BACKGROUND

To analytically prove the proposed propulsion concept, the net momentum flux generated by the oscillating bubble is obtained for an axisymmetrically oscillating bubble. The velocity components (u_r and u_θ) of the microstreaming flow in the polar coordinates (r, θ, ϕ) (Fig. 39) are derived from the streaming function ψ [equation (1) in chapter 3], as follows:

$$u_r = \frac{1}{r^2 \sin\theta}\frac{\partial \psi}{\partial \theta} = \frac{-6\varepsilon^2 a^4 \omega \sin(\Delta\phi)}{r^3}\left(\cos^3\theta - \cos\theta \sin^2\theta\right), \tag{1}$$

$$u_\theta = \frac{-1}{r \sin\theta}\frac{\partial \psi}{\partial r} = \frac{3\varepsilon^2 a^4 \omega \sin(\Delta\phi)}{r^3}\left(\cos^2\theta \sin\theta\right). \tag{2}$$

The bubble shape is assumed to be a half sphere on a solid flat surface. The net momentum flux can be calculated by integrating over the spherical surface area for arbitrary r. The infinitesimal area in the integration is described as $dA=(r\sin\theta d\phi)(rd\theta)$.

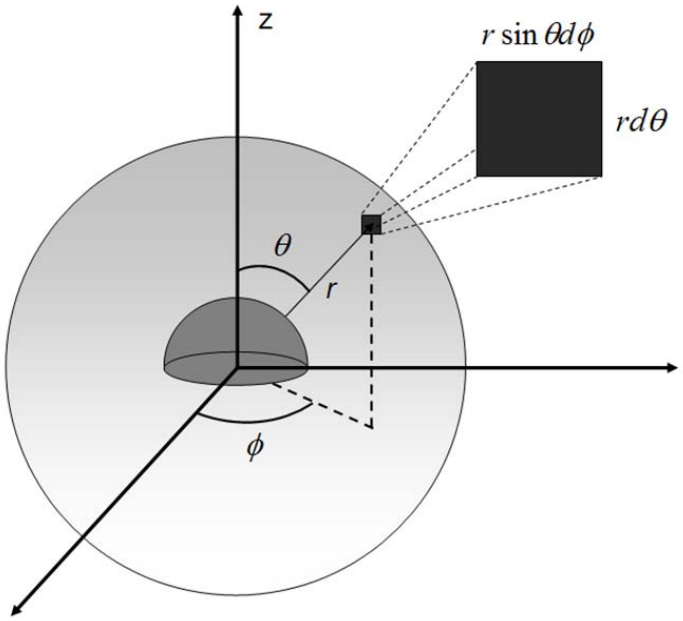

Figure 39 Schematic figure of a spherical bubble.

The net momentum flux in z direction is as:

$$P=\int_0^{\pi/2}\int_0^{2\pi}\left(\rho\underline{u}\cdot\underline{n}\right)\left(\underline{ue_z}\right)dA=\frac{36\pi\rho\varepsilon^4a^8\omega^2\sin^2\left(\Delta\phi\right)}{r^4}\times 0.167\,. \tag{3}$$

where, $\underline{n}$ is a surface normal vector and ρ is the medium density. Equation (3) reveals that the net momentum flux is not zero, which means that the oscillating bubble pushes the substrate as a reaction force. More specifically, the momentum flux is strongly dependent on oscillation

amplitude (fourth power of ε), bubble size (eighth power of a), and distance (negative fourth power of r) from the bubble. This analytical result is based on the assumption that the bubble oscillation is axisymmetric, which may not be realistic for the present surface wave mode oscillation. However, this result provides qualitative understanding of the proposed principle and guidelines for optimizing in the propulsion performance.

6.3 RESULTS AND DISCUSSION

6.3.1 Propulsion tests with glass rods

To experimentally prove the propulsion concept, multiple experiments are conducted using millimeter and micrometer sized glass rods in a small water chamber ($5 \times 5 \times 2.5$ cm^3 with 1.5 cm water level). A rod is immerged into the water chamber, and then a bubble (1 mm diameter) is injected on the tip of the submerged glass rod (Fig. 40a), which is held by a long gold wire (25 μm diameter and 5 mm length). A U-type polymer strut connects the wire and rod. The rod is free to move horizontally within a certain distance when tension of the wire is loose. The rod tip is coated with a hydrophobic Teflon layer to hold the bubble in place with strong adhesion (Fig. 40a1). The acoustic excitation is made by a ring-type piezo-actuator (outer and inner diameters, and thickness are 25 mm, 9.5 mm, and 3.2 mm, respectively, Omega Piezo Co.) glued on the bottom wall of the chamber. When the bubble is excited at 6-kHz (near the bubble resonance frequency) (Fig. 40a2), the rod (1 mm diameter with 3 mm length) is propelled left, meaning that the oscillating bubble pushes the rod. When the oscillating frequency is switched to 24 kHz, the rod is moving right (Fig. 40a3), in the opposite direction to the case in Fig. 40a2, indicating that

the oscillating bubble pulls the rod. It is speculated that the direction of the cavitational streaming flow is reversed. This result suggests that the frequency is an efficient parameter for controlling the propelling direction.

Similar experiments (Fig. 40b) are conducted with a microscale rod (220 μm diameter with 3 mm length) and bubble (470 μm diameter). Excitations at 13 kHz (near the bubble resonance frequency) and 18 kHz generates forward (Fig. 40b2) and backward (Fig. 40b3) propelling motions, respectively. By oscillating two separated bubbles (same size of 1 mm diameter) placed on a plate (one on the front face/the other on the back), rotational motions (torque) are generated (Fig. 40c). The bubbles are held on hydrophobic circle bases patterned by the standard photolithographic process. Excitations at 6 kHz and 24 kHz generate counterclockwise (Fig. 40c2) and clockwise (Fig. 40c3) rotations, respectively. This rotation direction is consistent with the dependency of the propulsion direction on the applied frequency.

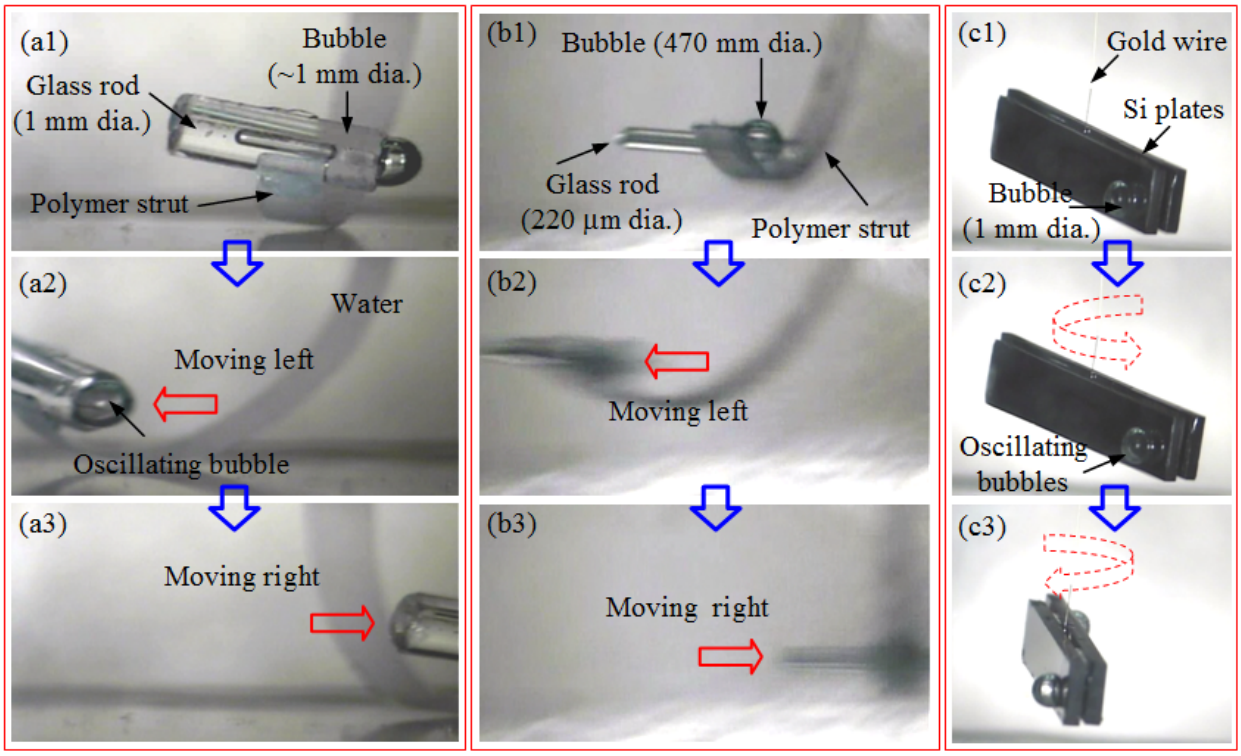

Figure 40 Snapshots of successive linear and rotational motions propelled by an oscillating bubble. (a) Linear propulsion of a glass rod (1 mm dia.). (a1) Initial state: A hydrophobic Teflon layer is deposited on the right tip of the rod to hold the bubble. (a2) When a bubble is acoustically excited at 6 kHz, the rod moves left (forward motion). (a3) When the applied frequency is changed to 24 kHz, the rod moves back to the right (backward motion). Note that the direction of the rod propulsion is easily controlled by the applied frequency. (b) Linear propulsion of a micron-sized glass rod. (b1) Initial state. (b2) When a bubble (470 mm dia.) is excited at 13 kHz, the submarine (220 mm dia.) moves to the left. (b3) When the same bubble is excited at 18 kHz, the submarine moves to the right. (c) Snapshots of rotational motions of rectangular Si plates (2× 10 mm2) by two oscillating bubbles of the same size (1 mm dia.). One bubble is attached to the front face and the other to the back face. They are separated by a certain distance to generate torque. The bubbles are sitting on hydrophobic circle bases patterned by the photolithographic micro process. (c1) Initial state. (c2) When the bubbles are excited at 6 kHz, the silicon plates rotate in a counterclockwise direction. (c3) At 24 kHz, the plates rotate in a clockwise direction.

6.3.2 Quantification of propulsion performance

To estimate the propelling force, the rod position in the pendulum configuration is measured when the propelled rod reaches a static equilibrium. Here, the propelling force is balanced with gravitational/buoyancy forces. By measuring the rod displacement, the propelling force vs. the voltage applied to the piezo-actuator is inferred, showing that the propelling force is proportional to the voltage (Fig. 41a, more exactly, bubble oscillation amplitude, see high-speed bubble images). The measured forces (hundreds nano-Newtons) are confirmed to be in the similar range of Stokes' drag calculated by the rod moving speed. Figure 41b shows the propelling force vs. the bubble oscillating frequency. The oscillating bubble generates a pushing force only near the bubble resonance frequency (6-kHz), whereas at the rest of the frequencies the bubble pulls the rod.

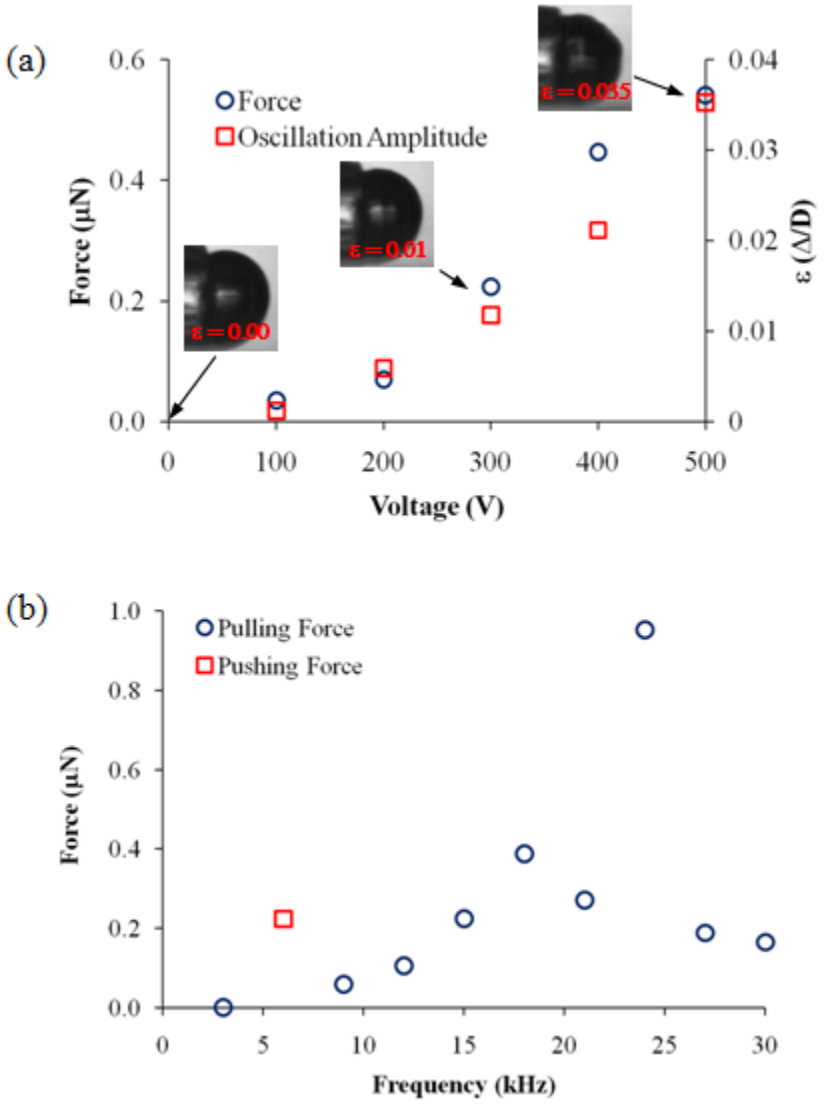

Figure 41 Measurement of quantitative propulsion forces. (a) Propelling force and bubble oscillation amplitude vs. voltage applied to the piezo-actuator at 6 kHz. Both bubble oscillation amplitude and propelling force are proportional to the applied voltage. The bubble oscillation amplitude Δ is measured at the bubble apex using high speed images (see insets) and normalized by the bubble diameter D (~ 1 mm) (ε = Δ/D). The propelling force is measured using the propelling displacement of the rod when hanging in the pendulum configuration. (b) Force vs. applied oscillation frequency. The bubble is oscillated in a wide range of frequency but the applied voltage is fixed at 300 V. Only near the bubble resonance frequency (~6 kHz), the pushing force is generated. At other frequencies, the rod is pulled by the oscillating bubble (D ~ 1 mm).

6.4 SUMMARY

In this chapter, a novel principle of underwater propulsion with proof-of-experiments utilizing the cavitational microstreaming flow. Uniqueness is that propelling is generated by oscillating bubbles remotely excited by an acoustic source, with no need for any moving parts(or paddling) or electric wiring to the bubbles. When an acoustic wave is applied to a gaseous bubble sitting on the tip of submerged mini/micro glass rod, the bubble oscillates and generates strong "streaming flows" around the bubble, called "cavitational microstreaming", resulting in generating a net momentum flux away from/toward the rod. As a consequence of the net momentum flux, the rod is pushed or pulled. Both strength and direction of propulsion are highly controllable by simply changing the frequency and amplitude of the applied acoustic wave. To estimate the propelling force, the rod position in the pendulum configuration is measured when the propelled rod reaches a static equilibrium. The measured forces are hundreds nano-Newtons, which is similar to Stokes' drag calculated by the rod moving speed. By oscillating two separated bubbles (same size of 1-mm-dia) on a plate (one on the front face/the other on the back), rotational motions (torque) are generated. Excitations at 6-kHz and 24-kHz generate counterclockwise and clockwise rotations, respectively.

7.0 CONCLUDING REMARKS

This thesis deals with development of novel manipulation techniques of micro/mini objects using oscillating bubbles. The operational concept, device fabrication, experimental proofs, characterizations, and underlying physics for several proposed object manipulation techniques are presented throughout the chapters. Most of the presented techniques are non-invasive, cost-effective, and simple, possibly being used for biological cells in microscope glass slide configurations. Two major physical principles studied and applied are cavitational microstreaming flows and electrowetting on dielectric (EWOD) actuation in gaseous bubbles. Micro/mini bubbles oscillated and handled in 2-D and 3-D spaces using these two principles are key components serving as carriers of objects to be manipulated.

The first type manipulation system allows us to manipulate mini/micro objects on a 2-D space-i.e., two-plate channel configuration consisting of the top and bottom plates with a piezo-actuator attached beneath the bottom plate. A series of bubble operations (creation, elimination, and transportation) and object manipulations (capturing, carrying, and releasing) is extensively investigated in this configuration along with modeling and analysis. Bubbles which are used as carriers for object manipulations are electrochemically created in an on-chip and on-demand manner and transported in any direction by EWOD actuations. The created bubble size is precisely time-controlled and modeled using a simple charge conservation principle. When the bubbles are excited by the piezo-actuator near their resonant frequencies, the oscillating bubbles

capture micron- and millimeter-sized particles. A variety of objects including micro-beads, a fish egg, and a live water flea are successfully captured. The capturing forces is identified and first completely confirmed as the acoustic radiation force through several experiments. Effects of the frequency and amplitude of acoustic excitation on capturing are quantified with high-speed imaging. The capturing operation is integrated with EWOD bubble transportation in order to demonstrate a series of object manipulation (capturing, carrying, releasing). Their operational performance is experimentally characterized: the carrying efficiency by oscillating bubbles for glass and polystyrene particles is over 95% with minimal particle loss. When the particles arrive at a desired location, they are released from the bubbles by turning off the acoustic excitation. Furthermore, the bubbles can be eliminated on-chip by the reverse electrochemical reaction if they are not used anymore. The bubble elimination is accelerated an order of magnitude faster using a Pt catalyst electrode. The elimination process is modeled by two sequential steps: catalytic reaction and dissolving process. In addition, the similar operations of capturing, carrying, releasing of objects are accomplished only using AC-EWOD, not using the acoustic excitation. In this case, the AC voltage (optimal frequency of 100 Hz) not only oscillates the bubble but also transports the oscillating bubble on the surface. However, the carrying efficiency is lower than the simultaneous actuations of acoustic excitation and EWOD.

The second type object manipulation system utilizes the capturing phenomenon by oscillating bubble. The main feature is that oscillating bubble is deposited on a 3-D traversing rod tip, rather than a two-dimensional surface. So it allows for object manipulation in a 3-D space. When the bubble is near objects, a piezo-actuator glued to the bottom of a water chamber is turned on at the bubble's resonant frequency. The bubble oscillates and captures the objects. The captured objects are carried by traversing the rod tip. Upon turning off the acoustic

excitation, the objects are easily released from the bubble. To quantify the carrying efficiency, the carrying speed is changed by moving the water chamber while the bubble tip is fixed. It is concluded that the maximum carrying speed is highest near the bubble resonant frequency, meaning that the trapping force is proportional to the bubble oscillation amplitude.

Finally, the cavitational streaming flow is extended to underwater propulsion (manipulation of objects much larger than the oscillating bubble). The key concept is to utilize the net momentum flux around the oscillating bubble. As a reaction force, the net momentum flux pushes or pulls the solid substrate on which the oscillating bubble sits. Both strength and direction of propulsion are highly controllable by simply changing the frequency and amplitude of the applied acoustic wave. Using mini/micro glass rods, the propulsion mechanism is experimentally proved. The propulsion force is measured to be hundreds nano-Newtons in a pendulum configuration. This propulsion method implicates such an application as propelling and maneuvering swimming robots inside human body that can be potentially used for drug delivery, surgery, and diagnostics.

7.1 FUTURE RESEARCH RECOMMENDATIONS

7.1.1 Enhancement of bubble elimination

The first future research topic involves enhancement of bubble elimination in 2-D micro-object manipulation systems. One of the critical drawbacks in the current 2-D micro-bubbles manipulation systems is slow bubble elimination by electro-chemical reaction. For a 200 μm diameter sized bubble elimination, it still takes more than 10 minutes. The previous experiment

show that thinning the Teflon layer improves the bubble elimination speed; however, the current thinnest Teflon thickness (400 Å) almost reaches the minimum thickness we can attain using the spin-coating method.

Application of acoustic excitation may significantly improve the bubble elimination speed. When a bubble is oscillated by acoustic excitation, the streaming flow around the oscillating bubble may promote chemical reactions on the surface and the rate of bubble dissolution into medium may be augmented more than twenty times [91]. Optimization of the control parameters such as the applied acoustic amplitude and frequency will increase the elimination speed further. Increasing the contact area between the bubble and the platinum catalyst will be another option. To increase the contact area, the elimination substrate can be structured with post arrays patterned by the MEMS technology, as shown in Fig 42. The increased contact area would increase the chemical reaction region, thus enhancing the bubble elimination speed.

Possibly, the combined approach of electrochemical reaction, acoustic excitation, and post-structured surface may provide the most efficient bubble elimination method. In addition, the current simple modeling for the bubble elimination process should be improved. The simple modeling consists of two sequential steps: electrochemical reaction and dissolution. The current electrochemical reaction modeling did not take into account the detailed effect of the catalytic reaction. A better understanding of the catalytic reaction and its implementation into the modeling should describe the electrochemical reaction process better.

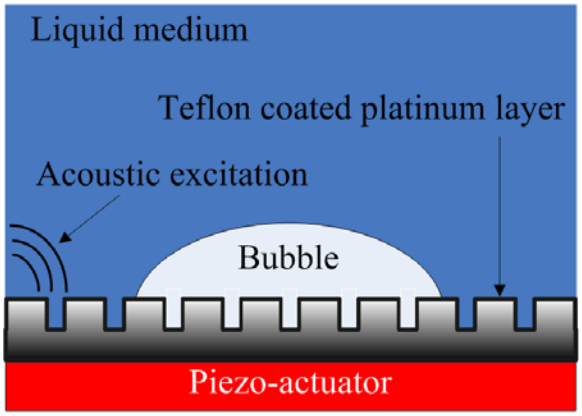

Figure 42 Enhanced micro bubble elimination method consisting of electrochemical reaction, acoustic excitation, and application of post-structured surface

7.1.2 3-D biological cell manipulation systems

In the 3-D manipulation, the bubble is oscillated by the acoustic excitation. Another method to oscillate the bubble is to use EWOD actuation (Fig. 43). This method minimizes cross-interference when multiple bubbles are used for multiple, parallel manipulations. In addition, it allows low frequency oscillations. The tip can be covered with a conductive metal layer and a hydrophobic dielectric layer for EWOD actuation. When the bubble is placed close to cells, an alternating voltage (about 200 Hz) is applied to the EWOD electrode. The bubble oscillates and generates a radiation attraction force similar to that generated by acoustic excitation, resulting in capturing of the neighboring cells. The captured cells can be carried in any direction in three-dimensional space by the traverse systems. It should be noted that the bubble is continuously actuated by EWOD during the carrying process. When the carried cells reach a desired place, the cells can be released from the bubble by turning off the EWOD actuation. Sometimes the micro gaseous bubble can not last more than a minute due to the dissolving process. If longer life time

is required, contrast agent bubbles which are coated with molecules to minimize the dissolving process can be used.

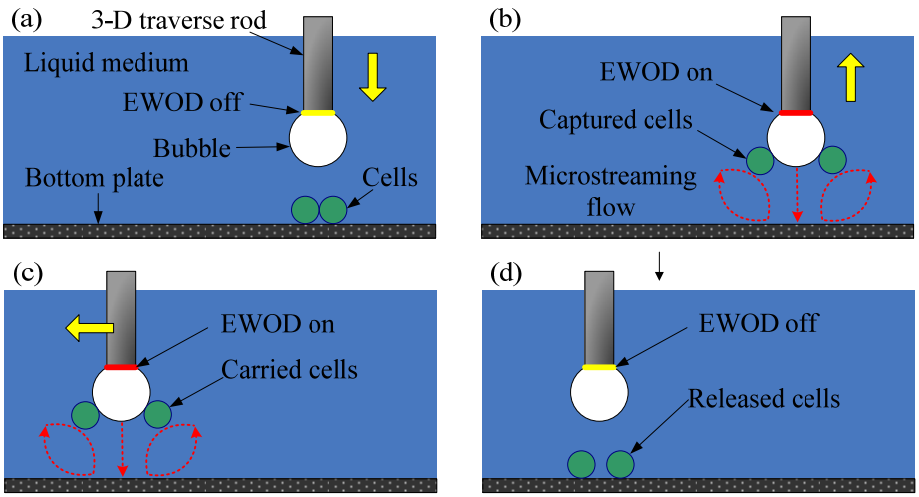

Figure 43 Biological cells captured, transported, and released by an oscillating bubble attached to a three-dimensional traverse rod tip: (a) Initial state (the rod tip is coated with a hydrophobic layer to ensure it holds a bubble), (b) The bubble captures cells when EWOD actuation excites the bubble on the rod tip, (c) The captured cells are carried by moving the tip via a three-dimensional traversing system, (d) When the bubble reaches its destination, EWOD actuation is turned off and the carried cells are released from the bubble.

7.1.3 Swimming robots actuated by multiple oscillating bubbles

In Chapter 6, the propulsion mechanism is experimentally proved by using a mini/micro glass rod. However, only 1-D propulsions are achieved and demonstrated. A real life swimming robot needs to be propelled in any direction in a 3-D space with increased propulsion speed. For this purpose, multiple oscillating bubbles can be placed in the swimming robot.

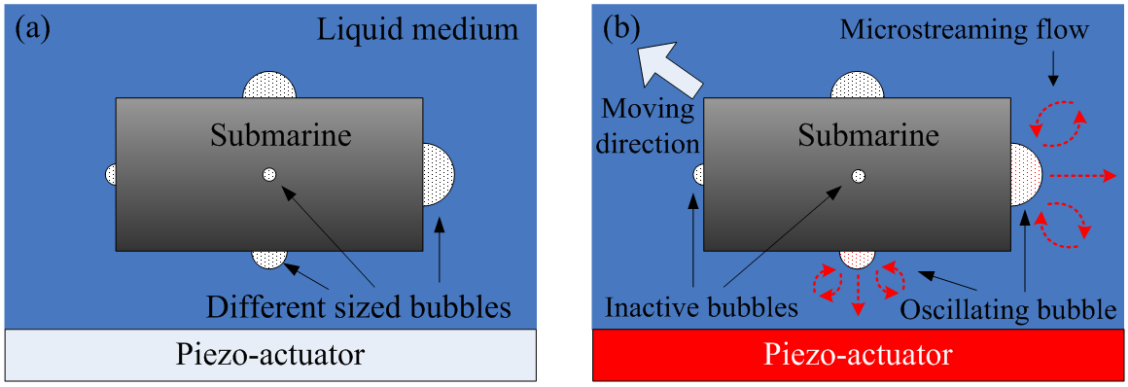

Figure 44 Submarine propulsion scheme in 3-D space by a cavitational microstreaming flow: (a) Initial state, (b) A submarine moves to the up and left direction when the bubbles on the rear and bottom sides of the submarine are excited by a piezo-actuator attached to the bottom of a water chamber.

When an acoustic wave is propagated to multiple bubbles of different size, only the bubble of a certain size (having the resonant frequency close to the applied frequency) actively becomes excited and generates the cavitational streaming flow, while other bubbles remain inactive. For simultaneous actuations of multiple bubbles of the same size, a single actuator can activate all of them if the actuator emits the single frequency acoustic wave at the bubble resonance frequency. For multiple bubbles of different size, a single actuator can also excite them simultaneously if the actuator can generate superposed acoustic waves of multiple frequencies. By adjusting the applied frequency to the resonant frequencies of desired bubbles, only the desired bubbles can be activated while others are still deactivated.

Based on this principle, a single, uniquely sized bubble is attached to the center of each surface of the swimming robot (Fig. 44a). Patterned hydrophobic layers can be applied to the swimming robot surfaces to improve bubble adhesion and minimize any lateral bubble movement during the bubble excitation. The swimming robot can move in an up and left direction by only exciting the bubbles on the rear and bottom sides, while other bubbles remain

inactive during the acoustic excitation (Fig. 44b). In this manner, the swimming robot can move in any direction in a three-dimensional space. To increase the speed of the submarine, multiple bubbles of the same size could be attached to the same surface.

BIBLIOGRAPHY

1. Nakayama, T., H. Fujiwara, K. Tastumi, K. Fujita, T. Higuchi, and T. Mori, *A new assisted hatching technique using a piezo-micromanipulator.* Fertility and Sterility, 1998. **69**: p. 784-788.

2. Park, J., et al., *Design and fabrication of an integrated cell processor for single embryo cell manipulation.* Lab on a Chip, 2005. **5**: p. 91-95.

3. Tan, K.K. and S.C. Ng, *Computer-controlled piezo micromanipulation system for biomedical applications.* Engineering Science and Education Journal, 2001. **10**: p. 249-256.

4. Yanagiada, K., et al., *The usefulness of a piezo-micromanipulator in intracytoplasmic sperm injection in humans.* Human Reproduction, 1998. **14**(2): p. 448-453.

5. Böhringer, K., R. Fearing, and K. Goldberg, *Microassembly*, in *Handbook of Industrial Robotics*, S. Nof, Editor. 1999, John Wiley & Sons: New York.

6. Weck, M. and C. Peschke, *Equipment technology for flexible and automated micro-assembly.* Microsystem Technologies, 2004. **10**: p. 241-246.

7. Ashkin, A., J.M. Dziedzic, and T. Yamane, *Optical trapping and manipulation of single cells using infrared laser beams.* Nature, 1987. **330**: p. 769-771.

8. Ashkin, A. and J.M. Dziedzic, *Optical trapping and manipulation of viruses and bacteria.* Science, 1987. **235**: p. 1517-1520.

9. Curtis, J.E., B.A. Koss, and D.G. Grier, *Dynamic holographic optical tweezers.* Optics Communications, 2002. **207**: p. 169-175.

10. MacDonalds, M.P., et al., *Creation and manipulation of three-dimensional optically trapped structures.* Science, 2002. **296**: p. 1101-1103.

11. Sheetz, M.P., *Laser Tweezers in Cell Biology*. 1997: New York: Academic Press.

12. Glasgow, I.K., et al., *Handling individual mammalian embryos using microfluidics.* IEEE Transactions on Biomedical Engineering, 2001. **48**(5): p. 570-577.

13. Hong, J.W., et al., *A nanoliter-scale nucleic acid processors with parallel architecture.* Nature Biotechnology, 2004. **22**(4): p. 435-439.

14. Hsu, C.-H., C. Chen, and A. Folch, *Microcanals for micropipette access to single cells in microfluidic environments.* Lab on a Chip, 2004. **4**: p. 420-424.

15. Kessler, J.O., *Hydrodynamic focusing of motile algal cells.* Nature, 1985. **313**: p. 218-220.

16. Maxwell, R.B., et al., *A microbubble-powered bioparticle actuator.* Journal of Microelectromechanical Systems, 2003. **12**(5): p. 630-640.

17. Cabrera, C.R. and P. Yager, *Continuous concentration of bacteria in a microfluidic flow cell using electrokinetic techniques.* Electrophoresis, 2001. **22**: p. 355-362.

18. Kremser, L., D. Blaas, and E. Kenndler, *Capillary electrophoresis of biological particles: Viruses, bacteria, and eukaryotic cells.* Electrophoresis, 2004. **25**: p. 2282-2291.

19. Westermeier, R., N. Barnes, and S. Gronau-Czybulka, *Electrophoresis in Practice: A Guide to Methods and Applications of DNA and Protein Separations.* 4th ed. 2005: John Wiley & Sons.

20. Burke, P.J., *Nanodielectrophoresis: Electronic nanotweezers.* Encyclopedia of Nanoscience and Nanotechnology, 2003. **X**: p. 1-19.

21. Chiou, P.Y., A.T. Ohta, and M.C. Wu, *Massively parallel manipulation of single cells and microparticles using optical images.* Nature, 2005. **436**: p. 370-372.

22. Jones, T.B., *Electromechanics of Particles*. 1995: Cambridge University Press.

23. Morgan, H. and N.G. Green, *AC Electrokinetics: colloids and nanoparticles*. 2003: Baldock, Hertfordshire, England: Research Studies Press.

24. Zimmerman, U. and G.A. Neil, *Electromanipulation of Cells*. 1996: CRC Press, Boca Raton.

25. Hultgren, A., et al., *Cell manipulation using magnetic nanowire.* Journal of Applied Physics, 2003. **93**(10): p. 7554-7556.

26. Lee, H., A.M. Purdon, and R.M. Westervelt, *Manipulation of biological cells using a microelectromagnet matrix.* Applied Physics Letter, 2004. **85**(6): p. 1063-1065.

27. Yan, J., D.Skoko, and J.F. Marko, *Near-field-magnetic-tweezer manipulation of single DNA molecules.* Physical Review E, 2004. **70**: p. 011905 (1-3).

28. Jager, E.W.H., O. Ingannäs, and I. Lundström, *Microrobots for micrometer-size objects in aqueous media: Potential tools for single-cell manipulation.* Science, 2000. **288**: p. 2335-2338.

29. Kim, C.-J., A. Pisano, and R.S. Muller, *Silicon processed overhanging microgripper.* Journal of Microelectromechanical Systems, 1992. **1**(1): p. 31-36.

30. Maruo, S., K. Ikuta, and H. Korogi, *Submicron manipulation tools driven by light in a liquid.* Applied Physics Letters, 2003. **82**(1): p. 133-135.

31. Chung, S.K., Y. Zhao, and S.K. Cho, *On-chip creation and elimination of microbubbles for micro-object manipulator.* Journal of Micromechanics and Microengineering, 2008: p. 18 (doi: 10.1088/0960-1317/18/9/095009).

32. Chung, S.K., et al., *Micro bubble fluidics by EWOD and ultrasonic excitation for micro bubble tweezers*, in *20th International Conference on Micro Electro Mechanical Systems (MEMS)*. 2007: Kobe, Japan. p. 31-34.

33. Chung, S.K. and S.K. Cho, *3-D manipulation of millimeter- and micro-sized objects using an acoustically-excited oscillating bubble.* Microfluidics and Nanofluidics, 2008. **6**: p. 261-265.

34. Hua, S.Z., et al., *Microfluidic actuation using electrochemically generated bubbles.* Analytical Chemistry, 2002. **74**(24): p. 6392-6396.

35. Nielsen, N.J., *History of Thinkjet Printhead Development.* Hewlett-Packard Journal, 1985. **36**(5): p. 4-10.

36. Tseng, F.-G., C.-J. Kim, and C.-M. Ho, *A high-resolution high-frequency monolithic top-shooting microinjector free of satellite drops - Part I: concept, design, and model.* Journal of Microelectromechanical Systems, 2002. **11**(5): p. 427-436.

37. Lin, L.W., *Microscale thermal bubble formation: Thermophysical phenomena and applications.* Microscale Thermophysical Engineering, 1998. **2**(2): p. 71-85.

38. Neagu, C., et al., *An electrochemical microactuator: principle and first results.* Journal of Microelectromechanical Systems, 1996. **5**(1): p. 2-9.

39. Pang, C., et al., *Electrolysis-based diaphragm actuators.* Nanotechnology, 2006. **17**(4): p. S64-S68.

40. Stanczyk, T., et al., *A microfabricated electrochemical actuator for large displacements.* Journal of Microelectromechanical Systems, 2000. **9**(3): p. 314-320.

41. Suzuki, H. and R. Yoneyama, *A reversible electrochemical nanosyringe pump and some considerations to realize low-power consumption.* Sensors and Actuators B-Chemical, 2002. **86**(2-3): p. 242-250.

42. Jackel, J.L., J.J. Johnson, and W.J. Tomlinson, *Bistable optical switching using electrochemically generated bubbles.* Optics Letters, 1990. **15**(24): p. 1470-1472.

43. Taylor, R.S. and C. Hnatovsky, *Trapping and mixing of particles in water using a microbubble attached to an NSOM fiber probe.* Optics Express, 2004. **12**(5): p. 916-928.

44. Diop, M. and R. Taylor, *Soft trapping and manipulation of cells using a disposable nanoliter biochamber.* Biophysical Journal, 2006. **90**(10): p. 3813-3822.

45. Elder, S.A., *Cavitation microstreaming.* J Acoust Soc Am, 1958. **31**: p. 54-64.

46. Marmottant, P. and S. Hilgenfeldt, *Controlled vesicle deformation and lysis by single oscillating bubbles.* Nature, 2003. **423**(6936): p. 153-156.

47. Tho, P., R. Manasseh, and A. Ooi, *Cavitation microstreaming patterns in single and multiple bubble systems.* Journal of Fluid Mechanics, 2007. **576**: p. 191-233.

48. Fair, R.B., *Digital microfluidics: is a true lab-on-a-chip possible?* Microfluidics and Nanofluidics, 2007. **3**(3): p. 245-281.

49. Mugele, F. and J.C. Baret, *Electrowetting: From basics to applications.* Journal of Physics-Condensed Matter, 2005. **17**(28): p. R705-R774.

50. Zhao, Y. and S.K. Cho, *Micro Bubble Manipulation by Electrowetting on Dielectric: transporting, splitting, merging and eliminating of bubbles.* Journal of Lab a Chip, 2007. **7**(2): p. 273-280.

51. Dickerson, R.E., H.B. Gray, and G.P. Haight, *Chemical Principles*. Second ed. 1974: W. A. Benjamin, Inc.

52. Papavasiliou, A.P., *Bubble-actuated planar microvalves*, in *Mechanical Engineering*. 2001, University of California, Berkeley. p. 1-118.

53. Suzuki, H. and R. Yoneyama, *Integrated microfluidic system with electrochemically actuated on-chip pumps and valves.* Sensors and Actuators B-Chemical, 2003. **96**(1-2): p. 38-45.

54. Xie, J., et al. *Electrolysis-based on-chip dispensing system for ESI-MS*. in *16th International Conference on Micro Electro Mechanical Systems (MEMS 2003)*. 2003.

55. Ho, C.T., et al., *Micromachined electrochemical T-switches for cell sorting applications.* Lab on a Chip, 2005. **5**(11): p. 1248-1258.

56. Lee, S., E. Loth, and C. Liu, *Micro-bubbles generated on electrolytic arrays and matrices and released in a water channel.* Experiments in Fluids, 2005. **38**(5): p. 672-682.

57. Lippmann, M.G., *Relations entre les phénomènes electriques et capillaires.* Ann. Chim. Phys., 1875. **5**(11): p. 494-549.

58. Pollack, M.G., R.B. Fair, and A.D. Shenderov, *Electrowetting-based actuation of liquid droplets for microfluidic applications.* Applied Physics Letters, 2000. **77**(11): p. 1725-1726.

59. Verheijen, H.J.J. and M.W.J. Prins, *Reversible electrowetting and trapping of charge: Model and experiments.* Langmuir, 1999. **15**(20): p. 6616-6620.

60. Cho, S.K., H.J. Moon, and C.J. Kim, *Creating, transporting, cutting, and merging liquid droplets by electrowetting-based actuation for digital microfluidic circuits.* Journal of Microelectromechanical Systems, 2003. **12**(1): p. 70-80.

61. Kang, K.H., *How electrostatic fields change contact angle in electrowetting.* Langmuir, 2002. **18**: p. 10318-10322.

62. Jones, T.B., *On the relationship of dielectrophoresis and electrowetting.* Langmuir, 2002. **18**: p. 4437-4443.

63. Collet, P., et al., *Dynamics of the contact line: Contact angle hysteresis.* Physical Review Letter, 1997. **79**: p. 3704-3707.

64. Daniel, S. and M.K. Chaudhury, *Rectified motion of liquid drops on gradient surfaces induced by vibration.* Langmuir, 2002. **18**: p. 3404-3407.

65. Extrand, C.W., *A thermodynamic model for contact angle hysteresis.* Journal of Colloid and Interface Science, 1998. **207**: p. 11-19.

66. Furmidge, C.G.L., *Studies at phase interfaces I. The sliding of liquid drops on solid surfaces and a theory for spray retention.* Journal of Colloid Science, 1962. **17**: p. 309-324.

67. Latorre, L., et al., *Electrostatic actuation of microscale liquid-metal droplets.* Journal of Microelectromechanical Systems, 2002. **11**: p. 302-308.

68. Smithwick III, R.W., *Contact-angle studies of microscopic mercury droplets on glass.* Journal of Colloid and Interface Science, 1988. **123**: p. 482-485.

69. Chung, S.K., Y. Zhao, and S.K. Cho, *Electrowetting-On-Dielectric (EWOD) Microfluidic Devices*. Lab on a Chip (LOC) Technologies and Applications, ed. K.E.H.a.A. Rasooly. 2009: Caister Academic Press.

70. Usui, H., et al. *Insulation and passivation properties of vapor-depositedfluorinated polymer thin films*. in *Proceedings of the Symposium on Electrical and Electronic Insulating Materials and Applications in Systems*. 2001.

71. Kinoshita, K., *Electrochemcial Oxygen Technology*. 1992: Wiley-Interscience.

72. Marmottant, P. and S. Hilgenfeldt, *A bubble-driven microfluidic transport element for bioengineering.* Proceedings of the National Academy of Sciences of the United States of America, 2004. **101**(26): p. 9523-9527.

73. Marmottant, P., et al., *Microfluidics with ultrasound-driven bubbles.* Journal of Fluid Mechanics, 2006. **568**: p. 109-118.

74. Coakley, W.T. and W. Nyborg, *Cavitation; dynamics of gas bubbles; applications*. Ultrasound: Its application in medicine and biology, ed. E. F.J. Fry. 1978: Elsevier: New York. 77-159.

75. Wilson W. L., W.F.J., Nyborg W. L., Schnitzler R. N., Sichel F. J. , *Deformation and motion produced in isolated living cells by localized ultrasonic vibration.* J. Acoust. Soc. Am., 1966. **40**: p. 1363-1370.

76. Lutz, B.R., J. Chen, and D.T. Schwartz, *Hydrodynamic tweezers: 1. Noncontact trapping of single cells using steady streaming microeddies.* Analytical Chemistry, 2006. **78**(15): p. 5429-5435.

77. Hu, J. and A. Santoso, *A π-Shaped Ultrasonic Tweezers Concept for Manipulation of Small Particles.* IEEE Transactions on Ultrasonics, Ferroelectrics, and Frequency Control, 2004. **51**(11): p. 1499-1507.

78. Hu, J., et al., *Trapping, transportation and separation of small particles by an acoustic needle.* Sensors and Actuators A, 2007. **138**: p. 187-193.

79. Hu, J., J. Yang, and J. Xu, *Ultrasonic trapping of small particles by sharp edges vibrating in a flexural mode.* Applied Physics Letter, 2004. **85**(24): p. 6042-6044.

80. Miller, D.L., *Particle gathering and microstreaming near ultrasonically activated gas-filled micropores.* Journal of Acoustical Society of America, 1988. **84**(4): p. 1378-1387.

81. Leighton, T.G., *The Acoustic Bubble*. 1997: Academic Press.

82. Minnaert, M., *On musical air bubbles and sound of running water.* Phil. Mag., 1933. **16**: p. 235-248.

83. Lohse, D., *Bubble puzzles.* Physics Today, 2003. **56**: p. 36.

84. Lechelt, M., W. Blohm, B. Kirschneit, M. Pfeiffer, E. Gresens, J. Liley, R. Holz, C. Luring, and C. Moldaenke, *Monitoring of surface water by ultrasensitive Daphnia toximeter.* Environmental Toxicology, 2000. **15**(5): p. 390-400.

85. Spyridopoulos, M.T. and S.J.R. Simons, *Direct measurement of bubble-particle adhesion forces on the effects of particle hydrophobicity and surfactant.* Chemical Engineering Research and Design, 2004. **82**(4): p. 490-498.

86. Chung, S.K. and S.K. Cho, *On-chip manipulation of objects using mobile oscillating bubbles.* Journal of Micromechanics and Microengineering, 2008. **18**: p. 125024 (12pp).

87. Kim, B., et al., *A biomimetic undulatory tadpole robot using ionic polymer–metal composite actuators.* Smart Materials and Structures, 2005. **14**: p. 1579-1585.

88. Weibel, D.B., et al., *Microoxen: Microorganisms to move microscale loads.* Proc. Natl. Acad. Sci, 2005. **102**: p. 11963.

89. Behkam, B. and M. Sitti, *Bacterial flagella-based propulsion and on/off motion control of microscale objects.* Appl. Phys. Lett., 2007. **90**: p. 023902.

90. PAXTON W. F., A.S., MALLOUK T. E., *Motility of catalytic nanoparticles through self-generated forces.* Chemistry - A European Journal, 2005. **11**(22): p. 6462 - 6470.

91. Gould, R.K., *Rectified diffusion in the presence of, and absence of, acoustic streaming.* J. Acoust. Soc. Am., 1973. **56**: p. 1740-1746.